Searches for dark matter self-annihilation signals from dwarf spheroidal galaxies and the Fornax galaxy cluster with imaging air Cherenkov telescopes

Dissertation
zur Erlangung des Doktorgrades
des Fachbereichs Physik
der Universität Hamburg

vorgelegt von

Björn Helmut Bastian Opitz
aus Warburg

Hamburg
2014

Gutachter der Dissertation:	Prof. Dr. Dieter Horns JProf. Dr. Christian Sander
Gutachter der Disputation:	Prof. Dr. Dieter Horns Prof. Dr. Jan Conrad
Datum der Disputation:	17. Juni 2014
Vorsitzender des Prüfungsausschusses:	Dr. Georg Steinbrück
Vorsitzende des Promotionsausschusses:	Prof. Dr. Daniela Pfannkuche
Leiter des Fachbereichs Physik:	Prof. Dr. Peter Hauschildt
Dekan der MIN-Fakultät:	Prof. Dr. Heinrich Graener

Abstract

Many astronomical observations indicate that dark matter pervades the universe and dominates the formation and dynamics of cosmic structures. Weakly interacting massive particles (WIMPs) with masses in the GeV to TeV range form a popular class of dark matter candidates. WIMP self-annihilation may lead to the production of γ-rays in the very high energy regime above 100 GeV, which is observable with imaging air Cherenkov telescopes (IACTs).

For this thesis, observations of dwarf spheroidal galaxies (dSph) and the Fornax galaxy cluster with the Cherenkov telescope systems H.E.S.S., MAGIC and VERITAS were used to search for γ-ray signals of dark matter annihilations. The work consists of two parts: First, a likelihood-based statistical technique was introduced to combine published results of dSph observations with the different IACTs. The technique also accounts for uncertainties on the "J factors", which quantify the dark matter content of the dwarf galaxies. Secondly, H.E.S.S. observations of the Fornax cluster were analyzed. In this case, a collection of dark matter halo models was used for the J factor computation. In addition, possible signal enhancements from halo substructures were considered.

None of the searches yielded a significant γ-ray signal. Therefore, the results were used to place upper limits on the thermally averaged dark matter self-annihilation cross-section $\langle \sigma v \rangle$. Different models for the final state of the annihilation process were considered. The cross-section limits range from $\langle \sigma v \rangle_{\mathrm{UL}} \sim 10^{-19}\ \mathrm{cm^3 s^{-1}}$ to $\langle \sigma v \rangle_{\mathrm{UL}} \sim 10^{-25}\ \mathrm{cm^3 s^{-1}}$ for dark matter particles masses between 100 GeV and 100 TeV. Some of the diverse model uncertainties causing this wide range of $\langle \sigma v \rangle_{\mathrm{UL}}$ values were analyzed.

Kurzfassung

Verschiedene astronomische Beobachtungen deuten darauf hin, dass dunkle Materie das Universum durchzieht und die Entstehung und Dynamik kosmischer Strukturen dominiert. Schwach wechselwirkende, massive Teilchen (WIMPs, von "weakly interacting massive particles"), deren Ruhemasse im GeV- bis TeV-Bereich liegt, sind vielversprechende Kandidaten für eine teilchenphysikalische Erklärung der dunklen Materie. Selbstvernichtungsprozesse von WIMPs können Gammastrahlung im Energiebereich oberhalb von 100 GeV erzeugen, die mit abbildenden Luftschauer-Tscherenkow-Teleskopen (IACTs, "imaging air Cherenkov telescopes") beobachtet werden kann.

Für diese Dissertation wurden Beobachtungen von sphäroidalen Zwerggalaxien (dSph) und des Fornax-Galaxienhaufens mit den Tscherenkow-Teleskopen H.E.S.S., MAGIC und VERITAS verwendet, um nach Gammastrahlungs-Signalen dunkler Materie zu suchen. Die Arbeit hat zwei Teile: Erstens wurde eine auf Likelihood-Funktionen basierende Methode eingeführt, die zur Kombination bereits publizierter dSph-Beobachtungen der verschiedenen IACTs dient. Diese statistische Methode kann zudem die systematischen Unsicherheiten der "J-Faktoren" miteinbeziehen, welche den DM-Inhalt der Zwerggalaxien quantifizieren. Zweitens wurden H.E.S.S.-Beobachtungen des Fornax-Galaxienhaufens analysiert. In diesem Falle wurden verschiedene Modelle des DM-Halos von Fornax verwendet, um die jeweiligen J-Faktoren zu berechnen. Außerdem wurden mögliche Verstärkungen des DM-Signals durch Halo-Substrukturen betrachtet.

Weder die Beobachtungen der Zwerggalaxien noch die des Galaxienhaufens lieferten ein signifikantes Gammastrahlungs-Signal. Deshalb wurden ihre Ergebnisse genutzt, um obere Grenzen (UL, "upper limits") auf den thermisch gemittelten Selbstvernichtungs-Wirkungsquerschnitt $\langle \sigma v \rangle$ der dunklen Materieteilchen zu bestimmen. Dabei wurden unterschiedliche Modelle für die Endzustände der Vernichtungsprozesse benutzt. Die Grenzen auf den Wirkungsquerschnitt liegen im Bereich von $\langle \sigma v \rangle_{\mathrm{UL}} \sim 10^{-19}\ \mathrm{cm^3 s^{-1}}$ bis $\langle \sigma v \rangle_{\mathrm{UL}} \sim 10^{-25}\ \mathrm{cm^3 s^{-1}}$, gültig für DM-Teilchenmassen von 100 GeV bis 100 TeV. Einige der unterschiedlichen Modellunsicherheiten und Abhängigkeiten, die zu diesem großen Bereich von $\langle \sigma v \rangle_{\mathrm{UL}}$-Werten führen, wurden ebenfalls erörtert.

Contents

List of Figures

List of Tables

Chapter 1

Introduction

Astronomy and particle physics are concerned with the very largest and the very smallest constituents of our universe, respectively. In both fields, technological progress and considerable observational, theoretical and financial efforts have allowed the establishment of "standard models" which describe the currently known phenomena with remarkable comprehensiveness[1]. The *standard model of particle physics*, in particular, successfully covers *all* experimental results found with the help of man-made particle accelerators, and it allows the computational prediction of particle interactions with astounding precision.

The *standard model of cosmology*, on the other hand, successfully describes the evolution of the universe since the "Big Bang" and the formation of large-scale structures within a compelling mathematical framework. However, it suffers from the fact that only a few percent of the energy content of the universe seem to consist of the known types of matter and radiation. About 70% are attributed to the mysterious "dark energy", whose origin is very poorly understood. In addition, more than 20% of the universe's energy density is in the form of "dark matter" (DM), which is also the driving component behind the formation and dynamics of galaxies, but cannot be explained by any the standard model particle. Hence, the astronomical observations which have decisively demonstrated the existence of dark matter also point to the need for particle physics "beyond the standard model" (BSM).

Correspondingly, both scientific communities of astronomy and particle physics (and their unifying offspring, "astroparticle physics") undertake strong efforts to better constrain and understand the properties of dark matter, and possibly find the yet unknown particle of which it consists. One path, which is also followed in the present work, is to aim for the *indirect detection* of dark matter by way of observing astronomical signals from *self-annihilations* of DM particles in the universe. These are expected if dark matter consists of *weakly interacting massive particles* (WIMPs) with masses in the order of $\sim 100\,\mathrm{GeV}$, which are a common by-product of BSM theories like supersymmetry.

[1] See Chapter 2 for an extended discussion and external references.

If such WIMP annihilations take place, they lead to the production of γ-rays with an energy spectrum reaching up (or close) to the rest mass energy of the dark matter particles. Unlike antiparticles, which can also act as messenger particles of DM annihilations, γ-rays point back to their source. Therefore, their observation can be used to look for a DM signal from particular objects in the sky, like the centre of our own galaxy, dwarf galaxies orbiting the Milky Way, or external clusters of galaxies.

Very high energy (VHE) γ-rays, commonly defined to have energies above 100 GeV, are detectable with ground-based imaging air Cherenkov telescopes (IACTs). These are used to detect the Cherenkov light emitted by superluminal particles in the electromagnetic showers produced when VHE γ-rays enter the Earth's atmosphere. One array of such telescopes is H.E.S.S., the *High Energy Stereoscopic System* located in Namibia, others include the MAGIC and VERITAS systems. All of these have been used to search for γ-ray signals from the self-annihilation of dark matter particles, and results from all three telescope systems were utilized for this thesis. It is organized as follows:

Chapter 2 provides the theoretical background for the remainder of the work. Section 2.1 summarizes the evidence for dark matter, its role in the ΛCDM framework, and the expected and observed properties of cold dark matter haloes. Section 2.2 explains why dark matter is not part of the particle physics standard model, describes thermal DM production in the early universe and introduces supersymmetry and other models of particle dark matter. Finally, Section 2.3 is concerned with techniques for the detection of DM particles, concentrating on the expected γ-ray signal from dark matter annihilations and its computation.

Chapter 3 covers the observation of VHE γ-rays with Cherenkov telescopes. The properties of air showers and the emitted Cherenkov light are briefly summarized in Section 3.1. The following sections focus on the H.E.S.S. detectors and analysis techniques used for Chapter 5, especially the suppression of the instrumental background from charged cosmic rays. MAGIC and VERITAS are covered in less detail.

In Chapter 4, a novel, likelihood-based stacking technique is introduced (Section 4.1), which allows the combination of published IACT searches for DM annihilation signals from dwarf spheroidal galaxies around the Milky Way (Section 4.2). In addition, this method takes into account the uncertainties on the DM haloes of the dwarf galaxies, which propagate into the predicted γ-ray yield from DM annihilations and constitute an important factor of systematic uncertainty in dark matter searches. While no significant dark matter signal has been found, limits on the parameter plane of dark matter particle mass and self-annihilation cross-section could be placed (Section 4.3). Building upon work by the *Fermi*-LAT collaboration (Ackermann *et al.* 2011), the above-mentioned halo uncertainties were included in a statistically meaningful manner. This is the first time that such a method has been employed in the analysis of IACT observations. It is also the first time that observations from *different* Cherenkov telescopes were combined in a stacking analysis. The results shown in this chapter have not been

previously published.

Chapter 5, on the other hand, mainly presents results which have been published by the H.E.S.S. collaboration (Abramowski *et al.* 2012, 2014). Observations of the Fornax cluster of galaxies were used to search for a dark matter annihilation signal, placing special emphasis on different determinations of the DM halo profile of the cluster (Section 5.1) and possible signal enhancements from dark matter substructure (Section 5.1.2). The analysis of H.E.S.S. data was performed for three different extensions of the signal region (Section 5.2), in order to account for the angular dependence of the potential subhalo boost. As no significant γ-ray signal was found, upper limits on the γ-ray flux were computed assuming both featureless power-law spectra and different γ-ray spectra from DM self-annihilations (Section 5.3.1). Finally, using the different observation regions, DM haloes and substructure boosts, upper limits on the self-annihilation cross-section were derived as a function of the DM particle mass. Here, several different final states of the annihilation process and flux enhancements from internal bremsstrahlung and the "Sommerfeld effect" were also taken into account (Sections 5.3.2, 5.3.3).

While Chapters 4 and 5 obviously build upon the previous ones, the attempt was made to keep them reasonably self-contained. Hence, some minor repetitions may occur. Chapter 6 summarizes the present work and provides an outlook of possible future continuations.

Throughout this work, the usual convention $\hbar = c = 1$ is followed, unless stated otherwise.

Chapter 2

Theoretical background

It is a common duty of graduate students in astrophysics to explain to their non-expert acquaintances the difference between "dark" matter and black holes. Despite the assumption of an expert readership of this thesis, the first section of this chapter shall serve to recapitulate the general lines of what we know about this intriguing type of *invisible* matter and its distribution in the universe. The second section contains a few ideas about the possible particle physics behind it. Finally, Section 2.3 shows how the combination of both allows to draw a sketch about how dark matter could be detectable, e.g. with observations in very-high-energy γ-rays.

2.1 Dark matter and the formation of galaxies

For most of its history, astronomy was a business of observing visible light. Correspondingly, the term "dark matter" was coined by Jan Hendrik Oort and Fritz Zwicky (see the next section) to denote something that did not *shine* like stars and galaxies. However, it became clear over the last century that dark matter (DM) isn't actually "dark" — rather, it does not interact electromagnetically at all, so that it doesn't absorb visible light either and is indeed invisible[1]. Nevertheless, it plays an import role in the formation and dynamics of galaxies and the whole observable universe.

2.1.1 Early observational evidence

Although the first use of the term "dark matter" is often attributed to Zwicky (1933), it was actually Oort (1932) who inferred the existence of non-luminous matter by an analysis of stellar velocities in the Milky Way. (Section 11 of his publication is titled "The amount of dark matter".)

[1] It should be mentioned that there may be higher-order interactions between dark matter and photons, see Section 2.3.1. They are, however, strongly suppressed.

Zwicky, on the other hand, mentioned "dunkle Materie" (since his article appeared in German) as a possible explanation why a simple dynamical estimate of the total mass of the Coma galaxy cluster was several hundred times larger than the sum of the masses of its galaxies (see also van den Bergh 1999). His argument was somewhat archetypical for constraints on the properties of dark matter haloes (as described in Section 2.1.4), therefore it is summarized swiftly here:

Many clusters of galaxies are relaxed structures, i.e. they are approximately in thermodynamic equilibrium and without obvious effects of external forces having acted upon them. Therefore, one can use the virial theorem

$$\overline{E_{\mathrm{kin}}} = -0.5\,\overline{E_{\mathrm{pot}}}\,, \tag{2.1}$$

relating the average kinetic and potential energies of the galaxies, to deduce the gravitational potential of the cluster from the observed velocity dispersion σ_v of the galaxies. Approximately, the total mass M of a cluster of radius[2] R is then given by

$$M = \frac{3\pi R \sigma_v^2}{2G}\,, \tag{2.2}$$

where G is the gravitational constant. Common values are $\sigma_v \sim 1000$ km s^{-1} and $R = 1$ Mpc, and correspondingly $M_{\mathrm{cluster}} \sim 10^{15}$ solar masses $\mathrm{M}_\odot$. Observations today show that about 80% of this mass are in the form of dark matter, while most of the baryonic mass is made up by the intracluster gas and only a few per cent of the total mass budget is contained in the optically visible galaxies (Voit 2005; Gonzalez *et al.* 2013).

Another classic piece of evidence for dark matter is provided by the velocity curves of spiral galaxies, observed e.g. by Rubin & Ford (1970) and Rubin *et al.* (1980). Here, the rotational velocities of stars and neutral hydrogen are measured as a function of the radial distance to the galaxy centre. Figure 2.1 shows how in a typical example, NGC 6503, the rotation curve is flat beyond the extent of the stellar disk (∼10 kpc in this case). The combined mass of stars and gas is not sufficient to cause this behaviour, so that an additional, "dark" component of the galaxy's gravitational potential is needed.

Additional evidence for dark matter is provided by observations of the large-scale structure of the universe and the cosmic microwave background. These are best understood in the framework of the current "standard model" of cosmology, which is described in the next section. More precise constraints on the properties of dark matter *haloes* are summarized in Section 2.1.4. These are important for the analyses presented in the later chapters of this thesis.

[2]Here, R denotes the *gravitational* radius, following Schneider (2006). Zwicky considered a sphere of evenly distributed mass. — Astronomical distances are commonly given in *parsecs*, where 1 pc = 3.09×10^{16} m = 3.26 ly.

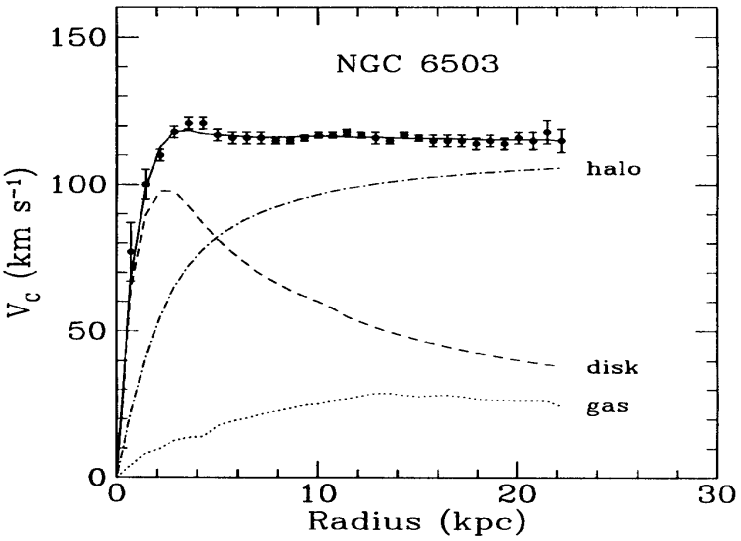

Figure 2.1: The rotation curve of the spiral galaxy NGC 6503 and the best-fitting constituents of its halo. The dash-dotted line indicates the contribution from the dark matter halo, while the other two lines show the velocity profiles expected from the stellar disk and baryonic gas only. This figure was adapted by Freese (2009) from Begeman et al. *(1991).*

2.1.2 ΛCDM and hierarchical structure formation

Many different types of astronomical observations over the past few decades have led to a "concordance" or "standard" model of cosmology, which describes the formation of the universe over the time since the Big Bang in remarkable precision[3]. According to this model, the present energy density of the universe is dominated by *dark energy*, parametrized by a cosmological constant Λ, and "cold" dark matter (CDM, see below). The total energy density $\Omega_{\text{tot}} = 1$ corresponds to a flat universe. The relative contributions of dark energy and dark matter are estimated as $\Omega_\Lambda \approx 69\%$ and $\Omega_{\text{CDM}} \approx 26\%$, while "normal" baryonic matter makes up only about 5 per cent (Planck Collaboration *et al.* 2013b).

Beyond these numbers, the ΛCDM model contains two important (though somewhat imprecise) conjectures about the nature of dark matter: First, the DM particles are produced thermally in the heat bath of the Big Bang, before they "freeze out" of thermal equilibrium due to the expanding universe. Hence, the mass, interaction cross-section and relic density of the dark matter are coupled, see Section 2.2.2. Second, it is mainly the dark matter that allows gravitational structure formation within the very uniform early universe: Baryonic matter overdensities are too small to evade being washed away by the cosmic expansion.

[3] Apart from the ever-growing number of textbooks on the subject, several review articles on the cosmological standard model and its parameters can be found in the "Review of Particle Physics" (Beringer *et al.* 2012). Two other reviews that were helpful for the present work were provided by Voit (2005) and Bennett (2006). Longair (2013) gathered a historical account.

Only the deep gravitational potential wells of dark matter structures allow the formation of galaxies.

In order to understand this scenario, it is helpful to compare the evolutionary timesteps of the ΛCDM universe with the supporting observational evidence:

Perhaps the most important ingredient of the cosmological standard model is the Big Bang scenario. Evidently, the universe has evolved from a rather definite beginning about 13.8 billion years ago (Planck Collaboration *et al.* 2013b), when it was a very hot and dense plasma in almost perfect thermal equilibrium. Ever since then, space itself has expanded, which resulted in adiabatic cooling of the universe and eventually allowed the formation of galaxies, stars and planets like our own.

First evidence for the *Big Bang* was found by Lemaître (1927) and Hubble (1929). They observed that not-too-distant galaxies recede from the Milky Way with velocities v that are, on average, proportional to their distance d. For historical reasons, this relation has become known as Hubble's Law:

$$v = H_0 \times d\,. \tag{2.3}$$

Here, H_0 is the present value of the Hubble parameter $H(t) = \frac{\dot{a}(t)}{a(t)}$, where the scale factor $a(t)$ describing the expansion is determined by general relativity and the different forms of energy density in the universe (radiation, matter, dark energy).

Another very important piece of evidence for the Big Bang was the discovery of the *cosmic microwave background* (CMB) by Penzias & Wilson (1965). This isotropic microwave radiation features an almost perfect black-body spectrum with a temperature of about 2.7 K (Mather *et al.* 1990; Fixsen 2009) and relative fluctuations of the order of 10^{-5}. It is convincingly interpreted as the relic radiation from the recombination of atomic nuclei and electrons about $t = 380,000$ years after the Big Bang (e.g. Dicke *et al.* 1965; Samtleben *et al.* 2007). The redshift

$$z = \frac{\lambda_{\text{observed}} - \lambda_{\text{emitted}}}{\lambda_{\text{emitted}}} \tag{2.4}$$

of recombination is $z \approx 1100$, i.e. the wavelength of CMB photons has been expanded by this value due to the expansion of the universe.

In fact, the almost perfect isotropy of the CMB poses a problem: Regions of the universe appear to have been isotropized when they were no longer causally connected. The *inflationary* scenario (see e.g. Bennett 2006) provides a possible explanation for this, as well as for the flatness of the universe:

At a very early phase of the Big Bang ($t \sim 10^{-35}$ sec), space may have undergone a phase of exponential expansion by many orders of magnitude. In the course of this inflation, quantum fluctuations of the scalar field driving the expansion were imprinted on the energy density of the universe, where they prevailed even after inflation had ended. These primordial fluctuations are assumed to have seeded the formation of structures in the universe. Eventually, they have proven visible

in the fluctuations of the CMB, first measured by the COBE satellite (Smoot *et al.* 1992). Although such CMB measurements can be seen as support for the inflation hypothesis, observational tests of inflationary models are notoriously difficult, see e.g. Planck Collaboration *et al.* (2013c). Nonetheless, the *BICEP2* collaboration has reported the detection of B-mode CMB polarization, which has been interpreted as evidence for primordial gravitional waves from cosmic inflation (Ade *et al.* 2014).

At the end of inflation, the universe must have been reheated (see Allahverdi *et al.* 2010) to a very dense and hot plasma, which subsequently cooled adiabatically. During this cooling plasma phase, the different constituents of the universe underwent phase transitions as the temperature fell below the respective reaction energies of the different interactions (see Section 2.2.1). Prominent examples are the electroweak phase transition, when the W and Z bosons acquired their masses through the mechanism named after Peter Higgs and a few others (see the Nobel prize 2013), the QCD phase transition when quarks were confined into protons and neutrons, or indeed the above-mentioned recombination of nuclei and electrons to bound atom states. Presumably at some point between the former two, however, another important transition took place: The decoupling of the dark matter particles from thermal equilibrium, and hence the freeze-out of dark matter yielding today's relic density. This is covered in more detail in Section 2.2.2.

An additional, very important ingredient of the cosmological standard model is *Big Bang nucleosynthesis* (BBN), the production of light elements in the first few (∼three, Weinberg 1977) minutes of the universe. Atomic nuclei such as those of helium, deuterium or lithium are formed thermally via nuclear reactions, while heavier elements can only be produced in supernova explosions. Since the corresponding reaction rates are known, the primordial abundances of these light elements can be calculated (e.g. Alpher *et al.* 1948) and compared to their occurence in the present universe, allowing for the reprocessing during stellar evolution. Apart from lithium, good agreement is generally found, depending on the baryon-to-photon ratio in the early universe and thus allowing an estimation of its baryonic matter content Ω_b (see the review in Beringer *et al.* 2012). The latter can also be determined from CMB observations and good agreement is found with abundance observations and BBN theory, visible in the right panel of Figure 2.2.

During all these stages, sound waves induced by the primordial fluctuations travelled through the plasma. The speed of these density waves was determined by the photonic radiation pressure on the baryons, and their propagation essentially stopped when the photon density was diminished by recombination. Therefore, the travel distance of a sound wave between inflation and the last scattering of photons at $z \sim 1100$ provides a cosmic distance scale, due to these *baryon acoustic oscillations* (BAO). This is indeed measurable in both the CMB and the (baryonic) large-scale structure (LSS) of the universe. Until today, the sound horizon has expanded to a scale of ~ 150 Mpc, visible as a peak in the correlation function

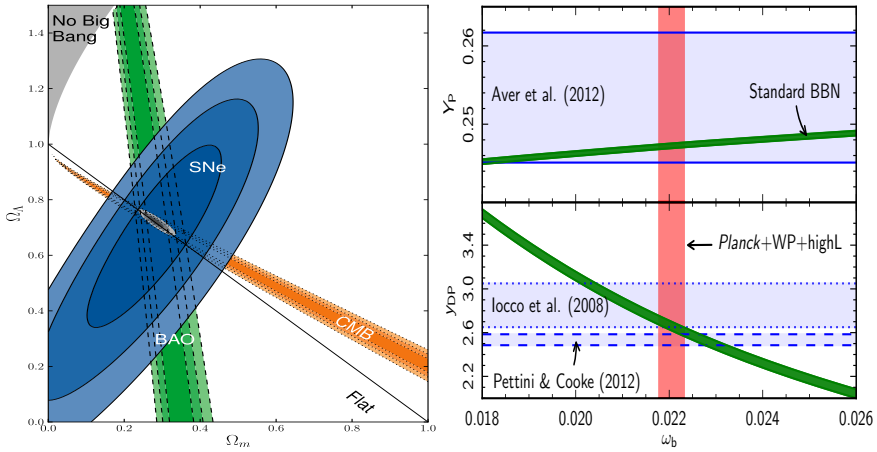

Figure 2.2: Evidence for non-baryonic dark matter in cosmological densities: Left, determination of the parameters Ω_Λ and Ω_m from observations of the cosmic microwave background (CMB), baryon acoustic oscillations (BAO, see main text) and supernovae (SNe, Suzuki et al. 2012). The concordance result of a flat universe with $\Omega_\Lambda \approx 0.7$ and $\Omega_m \approx 0.3$ is clearly visible. Right, Big Bang nucleosynthesis and the primordial abundances of helium (top) and deuterium nuclei (bottom). The blue shaded areas show astronomical observations, the green lines the expectation from standard BBN theory and the red line shows the Planck *measurement (Planck Collaboration et al. 2013b). The overall result of $\omega_b = \Omega_b h^2 \approx 0.022$, where $h \approx 0.7$ is the normalized Hubble constant, shows that baryons make up only ∼15% of the total matter density Ω_m.*

of galaxies over sufficiently large volumes of the universe (Eisenstein *et al.* 2005; Cole *et al.* 2005). The Fourier transform of this singular distance scale in real space is the harmonic series of peaks in the angular power spectrum of the cosmic microwave background, shown in Figure 2.3. This feature of the CMB was first observed with ground- and balloon-based telescopes (e.g. de Bernardis *et al.* 2000), and pinned down by the measurements of the *WMAP* satellite (Bennett *et al.* 2003 published the first-year results).

The positions and relative heights of these peaks depend on several cosmological parameters in distinguishable ways, see e.g. Figure 4 of Hu & Dodelson (2002). Thus, their precise measurement allowed the conclusion that the universe is flat and dominated by dark energy and dark matter, as described above. (See Hinshaw *et al.* (2013) and Planck Collaboration *et al.* (2013b) for the latest cosmological parameter determinations from WMAP and Planck, respectively.)

The combination of CMB observations with those of baryon acoustic oscillations in the large-scale structure and supernova lightcurves allows a particularly constraining determination of Ω_m and Ω_Λ: As visible in the left panel of Figure 2.2, these measurements have orthogonal parameter degeneracies. This makes the concordance result of $\Omega_\Lambda \approx 0.7$ and $\Omega_m \approx 0.3$ rather conclusive, despite the lack of a compelling theoretical explanation for the cosmological constant Λ.

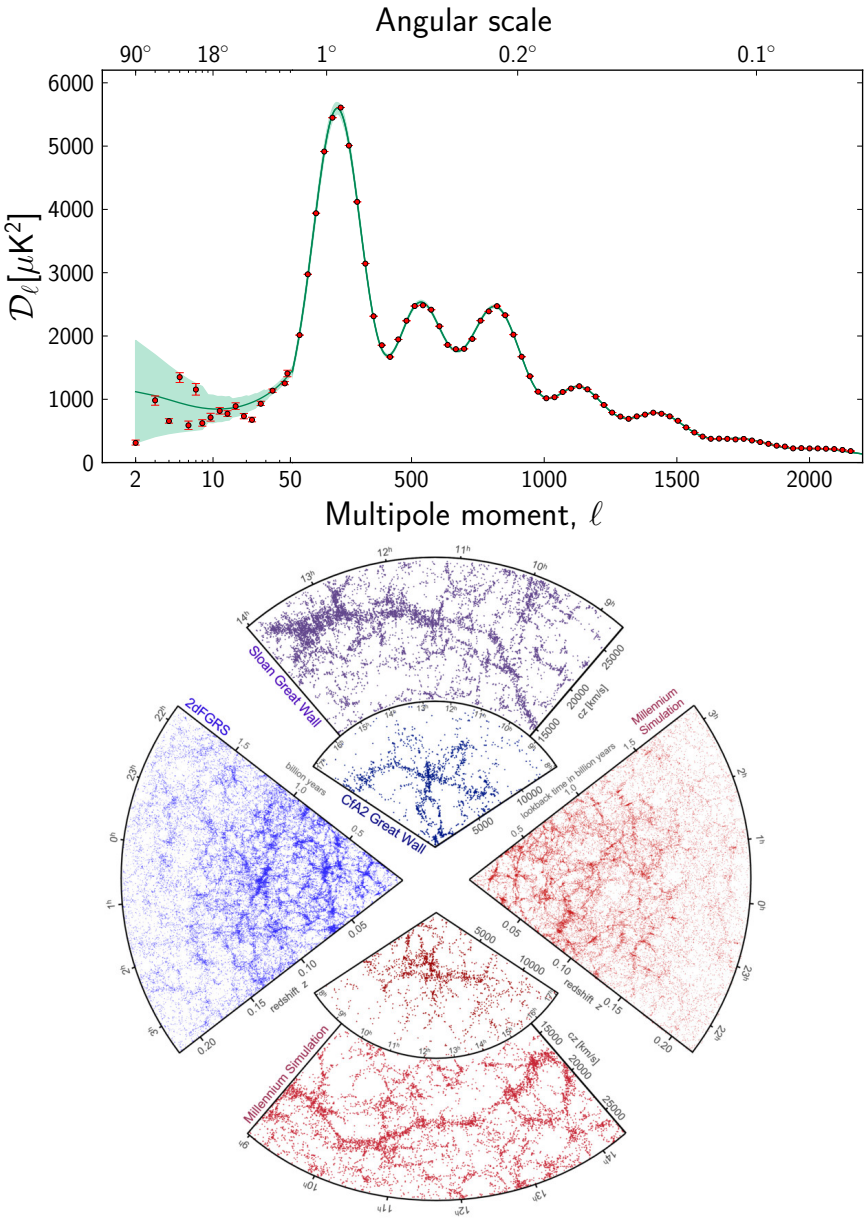

Figure 2.3: Concordance cosmology. Top panel: The Planck *measurement of the CMB temperature power spectrum (data points) and the best-fit ΛCDM model (green line; the shaded band shows the uncertainty due to cosmic variance. Planck Collaboration* et al. *2013a). Bottom panel: The large-scale structure of the universe, up to $z \sim 0.2$, in observations (blue) and numerical simulation (red; Springel* et al. *2006 and* `www.mpa-garching.mpg.de/millennium`*).*

The decoupling of photons and atomic matter at recombination set the stage for the further evolution of the universe. No longer diluted by radiation pressure, the baryons started falling into the gravitational wells provided by the dark matter. Indeed, the minuteness of the plasma fluctuations apparent in the CMB indicates that the growth of structure in the universe was driven by matter which had already decoupled from the photon bath before recombination.

The ΛCDM model thus includes *hierarchical structure formation*: Small dark matter structures formed first, due to gravitational collapse against the expansion of space, and larger structures like galaxies, clusters or superclusters of galaxies are built up by mergers of smaller objects and accretion of diffuse matter. This picture has been vindicated by numerical simulations of structure formation, which are able to reproduce the large-scale content of the universe to high precision. (Springel *et al.* 2006 provide an overview).

The current large-scale structure is deduced from the observation of baryons, e.g. in sky surveys like 2dFGRS (Folkes *et al.* 1999) or SDSS (Abazajian *et al.* 2003), as well as observations of the "Lyman-α forest" (see e.g. Weinberg *et al.* (2003) and references therein), which map the distribution of neutral hydrogen. In addition, the dark matter structures themselves can be indirectly observed through their gravitational lensing of background light sources like quasars, as reviewed by Massey *et al.* (2010). The bottom panel of Figure 2.3 shows a graphical comparison of the LSS, out to the relatively modest redshift of about 0.2, as "seen" in the 2dFGRS and SDSS, and the *Millenium* simulation (Springel *et al.* 2005).

If dark matter consists of weakly interacting massive particles (WIMPs, Section 2.2.2), the first dark matter objects that were gravitationally bound and no longer dissipated away by the thermal motion of the dark matter particles possibly assembled around a redshift of 50. These "minihaloes" had a mass roughly similar to that of the Earth (Green *et al.* 2004; Diemand *et al.* 2005). For dark matter particle models other than WIMPs, this *free-streaming mass* (M_{lim}) can take quite different values, and even for the neutralino (Section 2.2.3), there is a considerable range of possible values (Bringmann 2009). Unfortunately, it is not possible to include these *microhaloes* in full simulations of cosmological structure formation: $M_{\mathrm{lim}} \sim 10^{-6}\ \mathrm{M}_{\odot}$ is a typical value for the free-streaming mass, while clusters of galaxies have masses around $10^{15}\ \mathrm{M}_{\odot}$, and these vastly different scales cannot yet be treated simultaneously. However, semi-analytical "toy models" of structure formation can reproduce the available information from simulations rather well (e.g. Bullock *et al.* 2001; Macciò *et al.* 2008). They also fit the high-resolution, small-scale simulations of microhalo formation that have been performed for redshifts up to ~ 30 (Diemand *et al.* 2005; Anderhalden & Diemand 2013, showing recent results).

The buildup of dark matter structures was followed and traced by the baryonic matter. Until a redshift of about ten, i.e. in the first few hundred million years of the universe, the first stars and galaxies had formed (see e.g. Bromm *et al.* 2009). Their radiation provided the energy for the *reionization* of the universe, turning most of the neutral atoms from the recombination era into a plasma of charged

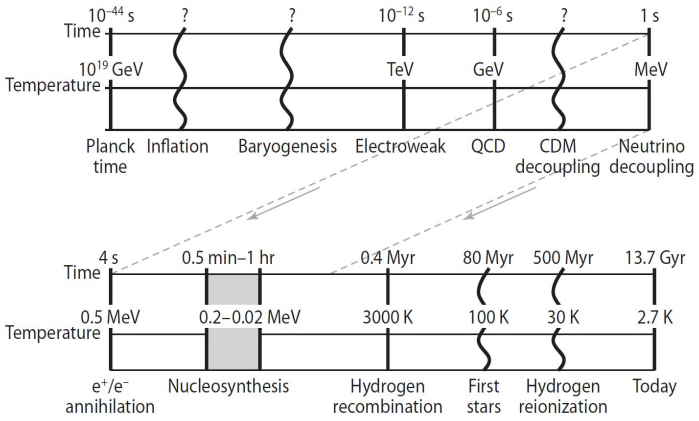

Figure 2.4: Thermodynamic history of the universe. From Loeb & Furlanetto (2013)

ions and electrons again (e.g. Robertson *et al.* 2010). Larger structures, like galaxy clusters and superclusters, have formed much later: Most clusters with masses above 10^{15} $M_\odot$ form at redshifts $z < 1$ (Voit 2005). This is also roughly the time ($z = 1$ corresponding to an age of about six billion years) when Dark Energy, if interpreted as a time-independent cosmological constant, started to dominate the energy density of the universe and to reaccelerate its expansion.

Figure 2.4 shows a summarising sketch of the history of the ΛCDM universe.

2.1.3 Properties of simulated dark matter haloes

As mentioned in the previous section, numerical simulations of the evolution of dark matter-dominated structures in the universe have provided significant support for the ΛCDM cosmology. Apart from these simulations of larger scales, important findings concern the *density profiles* and inner structure of dark matter haloes. These are difficult to measure observationally (see the next section), but the numerical results inform the interpretation of observations, therefore they are summarized here first. (Frenk & White (2012) review the history of the subject, whereas Kuhlen *et al.* (2012a) provide a snapshot of the state of the art in late 2012.)

While Press & Schechter (1974) already performed N-body simulations to test their influential model of structure formation, classic studies of dark matter *haloes* and their properties were those of Navarro, Frenk and White ("NFW"; Navarro *et al.* 1996; Navarro *et al.* 1997). They found that a "universal", two-parameter radial density profile $\rho(r)$ could be fit to all simulated haloes:

$$\rho_{\mathrm{NFW}}(r) = \frac{\rho_s}{\left(\frac{r}{r_s}\right)\left(1+\frac{r}{r_s}\right)^2}, \tag{2.5}$$

where r_s is the "scale radius" of the halo and $\rho_s = 4\rho(r_s)$ its characteristic density.

This density profile diverges as r^{-1} at the centre (although the mass contained in a sphere of radius r is finite), while it drops off as r^{-3} in the outer regions. Such inner slopes

$$\lim_{r\to 0}\left(\frac{\mathrm{d}\log\rho}{\mathrm{d}\log r}\right)=\gamma\approx -1 \tag{2.6}$$

characterize "cuspy" haloes, which are a general feature of cold dark matter simulations. Opposed to these are "cored" mass profiles such as the one defined by Burkert (1995):

$$\rho_B(r)=\frac{\rho_c r_c^3}{\left(r+r_c\right)\left(r^2+r_c^2\right)}\,, \tag{2.7}$$

which have a core of constant dark matter density ($\gamma=0$).

Both NFW and Burkert profiles for the Fornax galaxy cluster are depicted in Figure 5.3. While DM-only simulations always possess varying degrees of "cuspiness", some astronomical observations seem to show evidence for cored haloes. This "cusp vs. core" antinomy is covered in more detail in Section 2.1.5. It is quite relevant for efforts to detect dark matter in γ-rays because the self-annihilation luminosity scales with the *squared* DM density (see Section 2.3.1), so that overdense peaks of dark matter at the centres of haloes may boost the annihilation signal.

Finally, it should be mentioned that later numerical simulations (Navarro *et al.* 2004; Springel *et al.* 2008b) have indicated that DM halo profiles may actually be better approximated by the Einasto (1965) profile

$$\rho_{\mathrm{Ein}}(r)=\rho_{-2}\exp\left\{-\frac{2}{\alpha_E}\left[\left(\frac{r}{r_{-2}}\right)^{\alpha_E}-1\right]\right\} \tag{2.8}$$

whose inner slope is not constant, but gradually approaches zero. Here, r_{-2} is the radius at which $\gamma=-2$, $\rho_{-2}=\rho\left(r_{-2}\right)$ and α_E is a shape parameter. However, the difference between NFW and Einasto profiles is typically not very large on the relevant length scales, therefore only the former are used in the remainder of this work.

Another general property of simulated dark matter haloes is that their *concentration* depends on their mass. The concentration is defined as the ratio of the *virial radius* of a halo to its scale radius,

$$c=r_{\mathrm{vir}}/r_s\,. \tag{2.9}$$

Unfortunately, there is no universally used definition for the virial radius itself. Usually, it is defined as the radius enclosing a sphere that contains a particular mass density; the value used by Navarro, Frenk and White is 200 times ρ_{crit}, the critical density of the universe[4], hence this radius is denoted r_{200} in the work

[4]for which the universe is flat, $\rho_{\mathrm{crit}}=3H_0^2/8\pi G\approx 1.88\times 10^{-29}h^2\ \mathrm{g\,cm^{-3}}$

presented here (e.g. Chapter 5). Other authors, e.g. Bullock *et al.* (2001), defined the virial radius by an overdensity with respect to the average mass density of the universe, thus depending on the formation redshift of the halo.

Bullock *et al.* (2001) also analyzed the relation between halo concentration and mass, finding a relatively weak power law:

$$c\left(M_{\rm vir}\right) \propto M_{\rm vir}^{-0.1}\,, \tag{2.10}$$

depending on the environment of the halo, e.g. whether it is a genuine halo of its own or a subhalo of a larger one, and with a rather large scatter of $\Delta(\log c) \sim 0.2$. Further simulational studies have corroborated this relation (e.g. Macciò *et al.* 2008), and observations seem to validate it as well (e.g. Buote *et al.* 2007; Comerford & Natarajan 2007). For NFW profiles, the concentration of a halo is related to its structural parameters by the following identity:

$$M_{200} = \frac{4\pi}{3}\rho_{200}\,r_{200}^3 = 4\pi\rho_0\,r_s^3\left[\ln(1+c) - \frac{c}{1+c}\right]\,. \tag{2.11}$$

Therefore, one can approximately relate the *measured* virial mass M_{200} of a galactic system with its concentration c, and hence deduce its DM profile parameters ρ_s and r_s.

Yet another property of dark matter haloes which is important for the observational prospects of detecting a DM annihilation signal is the amount of *substructure* they contain. As mentioned in the previous chapter, the ΛCDM model includes the hierarchical buildup of larger structures from smaller ones. However, it isn't *a priori* known to which degree smaller haloes "survive" the merger process and subsequent tidal interactions, and thus continue to orbit their host haloes as gravitationally self-bound objects.

Numerical computations which were used to analyze the substructure of Milky-Way-like dark matter haloes include the *Aquarius* (Springel *et al.* 2008b) and *Via Lactea II* (Diemand *et al.* 2008) simulations. Springel *et al.* (2008b) and Springel *et al.* (2008a) conclude from their simulation that the *diffuse* main halo will be most easily detected from within the Milky way. However, the dark matter contained in *substructures* would shine about 200 times more brightly in annihilation γ-rays when viewed from outside the Galaxy. This "substructure boost" may even amount to a factor of 1000 for clusters of galaxies.

Pinzke *et al.* (2009) have used the Aquarius results to compute the boost as a function of the free-streaming mass, and their results were used for the calculations involving the Fornax galaxy cluster presented in Chapter 5. However, it should be noted that these calculations depend strongly on the interpolation of the subhalo properties between the resolution limit of the simulations (about 10^8 $M_\odot$) and the free-streaming mass (between 10^{-12} and 10^{-3} $M_\odot$, depending on the model). Some analytical models of structure formation find markedly different results for the boost factor. See e.g. Section 5.1.2 of this work or Section 2.2.2 of Kuhlen *et al.* (2012a) for a discussion.

2.1.4 Observational constraints on dark matter haloes

Contemporary numerical simulations of structure formation tracing only dark matter typically produce more or less concordant results (Kuhlen *et al.* 2012a). On the other hand, the backreaction of baryonic matter on the dark matter distributions is more difficult to model at the same level of precision. These complicated baryonic effects like star and galaxy formation, supernovae, AGN etc. have only recently been included in numerical simulations of halo formation (e.g. Stinson *et al.* 2013; Di Cintio *et al.* 2014). Nevertheless, they may lead to feedback effects that can either steepen the DM density profiles (e.g. via "adiabatic contraction", Blumenthal *et al.* 1986) or dilute the DM density by supernova feedback (Navarro *et al.* 1996; Pontzen & Governato 2012) or dynamical friction (e.g. El-Zant *et al.* 2001), thus flattening the inner profile to a core. Therefore, and simply in order to test the CDM simulations, it is necessary to compare observational results on dark matter haloes with these predictions.

Unfortunately, one cannot see a dark matter halo. Instead, the dark matter mass density has to be inferred from its effects on either background light sources or visible tracers of its gravitational potential. Three types of method have proven particularly successful:

1. As mentioned above, gravitational lensing of background light sources can be used to observe dark matter distributions (cf. Massey *et al.* 2010). Not only the masses of galaxies and galaxy clusters have been measured this way, but also their density profiles and halo substructure could be traced, even beyond the extent of visible matter. In general, the results were in good agreement with NFW-like expectations.

2. For most dark matter haloes, however, such analyses are not possible, due to the lack of a lensed light source. Therefore, optical observations of dynamical tracers are used to derive insights about the more central regions of the DM haloes, where such tracers are actually available. The choice of the tracer population and its interpretation depends on the object under consideration: Spiral galaxies allow the measurement of the above-mentioned stellar rotation curves (Figure 2.1), especially when they are observable edge-on. For elliptical galaxies, which have little or no net rotation, such a measurement cannot be performed; instead, the velocity dispersion is analyzed. It can be linked to the halo mass profile by use of the Jeans equations, see e.g. Binney & Tremaine (2008) or Walker (2013).

   At larger galactocentric radii, globular clusters can be used as tracer objects, and for the analysis of galaxy clusters, the galaxies themselves are obvious candidates for such studies. The corresponding results of Schuberth *et al.* (2010) and Drinkwater *et al.* (2001), respectively, have been used for the analysis of the elliptical galaxy NGC 1399 and the Fornax cluster in Chapter 5.

3. Finally, clusters of galaxies contain most of their baryonic matter (about 80%) in the form of hot, diffuse plasma, which emits thermal X-rays of a characteristic temperature. This temperature depends on the depth of the dark matter potential well, hence the mass of the cluster. Assuming that the gas is in hydrostatic equilibrium, the mass *profile* can also be extracted from measurements of the emitted X-ray spectrum. Buote *et al.* (2007), for example, have used such measurements to reconstruct the $c(M)$ relation (Equation 2.10) for early-type galaxies, galaxy groups and clusters in the mass range $0.06 - 20 \times 10^{14}$ $M_\odot$. This $c(M)$ function, in combination with the X-ray catalogue of Reiprich & Böhringer (2002), was also used to derive a mass profile of the Fornax cluster (Chapter 5).

All these methods have produced results which are, typically, in reasonable agreement with the expectations from cold dark matter simulations. There are, however, notable exceptions, see Section 2.1.5. At present, it is not known whether these are due to an intrinsic failure of the CDM model or to insufficient simulations, e.g. neglecting or wrongly modelling baryonic effects.

There are also shortcomings of the observational capabilities which limit the power to discriminate between cold dark matter and other models (Section 2.1.6). For example, observations of the dwarf spheroidal galaxies (dSph) of the Milky Way (see Chapter 4) allow a rather precise determination of the mass contained within their half-light radii, despite their small number of member stars (Walker *et al.* 2009, 2010; Wolf *et al.* 2010). The measurement of their mass *profiles*, on the other hand, is more difficult and ambiguous: The observable velocity dispersion profiles do not depend strongly on the inner DM density profiles, effects from anisotropies in the stellar system are difficult to disentangle from those of the mass profile itself, and especially in the very centre of the dSphs, there are simply not enough stars to allow a discrimination between cored and cuspy dark matter profiles. Nevertheless, there are indications that NFW profiles may be ruled out for certain dwarf galaxies (Walker & Peñarrubia 2011); however, these claims have also been disputed on methodological grounds (Kowalczyk *et al.* 2013), and the debate continues (Laporte *et al.* 2013).

2.1.5 Small-scale problems of cold dark matter

In fact, the above-mentioned "core-cusp problem" (de Blok 2010) about the inner density profiles of dark matter haloes is part of a set of issues where the CDM[5] predictions seem to be contradicted by observations. They concern the abundance and inner structure of dark matter subhaloes and the (presumably) corresponding dwarf galaxies, therefore they are often summarized as "small-scale problems of CDM". Weinberg *et al.* (2013) provide a recent and brief account of these issues

[5]These structures have formed before the onset of cosmic reacceleration, and so the issue of a time-dependent dark energy Λ does not play a dominating role. See, however, Penzo *et al.* (2014)

and their possible solutions, which shall be summarized here because they affect the observational prospects for the detection of dark matter:

It was mentioned in the previous section that there is an ongoing debate whether observations of dwarf spheroidal galaxies support their location within NFW-type dark matter haloes. This is particularly unfortunate because these dwarf galaxies, with their low baryonic content, are strongly dominated by dark matter and could thus serve as ideal testing grounds for DM halo models. A different type of galaxy which shares this property is the class of low surface brightness (LSB) galaxies. These can have higher halo masses than the dwarfs, but their low stellar densities ensure that their dynamics are also dominated by dark matter, and if they are late-type galaxies, their rotation curves can be measured. As reviewed by de Blok (2010), such observations point to cored or, at most, mildy cuspy dark matter haloes in LSBs (see also Kuzio de Naray & Spekkens 2011).

Such cored dark matter haloes contradict the "cuspy" CDM expectations. It was suspected for some time that the low baryonic content and lack of star-formation activity in dwarf galaxies prohibit the solution of this puzzle by baryonic physics. In the last few years, however, hydrodynamical simulations (Mashchenko *et al.* 2006; Governato *et al.* 2010) and analytical arguments (Pontzen & Governato 2012) have shown that repeated cycles of starburst activity, associated supernova feedback and gas outflows may sufficiently heat the dark matter haloes to erase the central cusps. On the other hand, Di Cintio *et al.* (2014) claim that the efficiency of this effect depends on the ratio of stellar and dark matter masses in a halo: Their simulations show that dwarf-scale haloes should be cuspy nevertheless, so the issue seems not to be settled yet.

Another possible explanation for the lack of cusps in dark matter haloes may lie in the physics of dark matter itself, rather than baryonic activity: *Warm* dark matter (WDM, see Section 2.1.6), having particle masses in the keV range, would produce cored haloes if the random motion of DM particles were sufficiently energetic. However, this line of argument runs into troubles when compared with the second type of small-scale CDM controversies, namely those associated with the abundance of dwarf-type galaxies corresponding to dark matter subhaloes:

First, it was realized that the relatively small number of dwarf galaxies ("satellites") orbiting the Milky Way could not compete with the much higher number of predicted dark matter subhaloes, when comparing the corresponding mass functions (or rotational velocities). This has become known as the "missing satellites" problem (Klypin *et al.* 1999; Bullock 2010) and is particularly pressing for small-mass subhaloes. It may, however, be alleviated by observational issues, as most of the smallest, "ultra-faint" dwarf spheroidals were discovered in data from the SDSS (e.g. Belokurov *et al.* 2007), which covers only about 20% of the entire sky. In addition, baryonic physics may come to the rescue of CDM again: The star formation in dark matter haloes may be sufficiently suppressed so that many more "dark" subhaloes could surround the Milky Way than can be observed (see again Weinberg *et al.* (2013) for references).

On the other hand, it was realized that the heaviest subhaloes in CDM simula-

tions lack a sufficient number of Milky Way counterparts as well. These haloes should be even more massive than the brightest satellites of our Galaxy, and therefore should not be able to "avoid" the formation of a visible stellar halo. This has been dubbed the "too big to fail" problem (Boylan-Kolchin *et al.* 2011). However, the numbers of such massive subhaloes are small, and star formation may be sufficiently stochastic, so that the Milky Way could still be a statistical anomaly rather than a falsification of CDM theory (Kuhlen *et al.* 2012b, 2013). (The same applies for Andromeda, which is the only other galaxy where such studies of the dwarf satellite population have been feasible, e.g. Collins *et al.* 2014.)

Meanwhile, *warm* dark matter would by itself cause the formation of a much smaller number of subgalactic dark matter structures, because the higher free-streaming mass of keV DM particles would suppress the formation of low-mass subhaloes in the first place. However, if such WDM particles were so light that they would lead to the formation of galaxy cores on the scales that are observed, the corresponding subhalo suppression would be so strong that there should be even *less* galactic substructure than is observed around the Milky Way. Hence, it seems that warm dark matter cannot solve both the cusp-core and subhalo abundance problems on the small scales of dark matter structure simultaneously (see also Schneider *et al.* 2014).

Summarizing the state of affairs, it still seems unclear whether these small-scale discrepancies in fact invalidate cold dark matter theory, or whether they can be solved by baryonic, astrophysical mechanisms. The observational knowledge of the amount and structure of dark matter satellites isn't decisive, either. Therefore, the CDM predictions and models that are used for the analyses of dwarf spheroidal galaxies (Chapter 4) and the Fornax cluster (Chapter 5) in the remainder of this thesis may cautiously be treated as reasonable, while certainly not proven.

2.1.6 Alternative theories and models

For the sake of fairness, a few alternatives to the standard (Λ)CDM picture ought to be mentioned. Although there is certainly sufficient motivation to search for heavy, "cold" dark matter particles, the theoretical ideas behind the WIMP picture may still prove altogether wrong. For example, Kroupa (2012) reviews what he considers a "falsification" of the standard model of cosmology on the ground of (dwarf) galaxy properties. Ostriker & Steinhardt (2003) discuss alternatives to CDM and their possible observational signatures. Different *particle* models of dark matter are discussed in Section 2.2.

Some of the noteworthy and well-studied alternatives to the standard CDM picture are the following:

Warm dark matter (WDM), roughly referring to DM particle masses in the keV range, has received renewed attention lately (Biermann *et al.* 2013), possibly because of the persisting small-scale problems sketched in Section 2.1.5. It can be made up by sterile, right-handed neutrinos produced in the early uni-

verse and provide the correct dark matter relic density (e.g. Abazajian *et al.* 2012). Nevertheless, such models face stringent observational constraints from structure formation, as warm dark matter haloes form later and with less substructure than those of cold DM. Therefore, the observation of matter structures at high redshift in the Lyman-α forest can be used to set limits on possible sterile neutrino parameters (e.g. Viel *et al.* 2006; Viel *et al.* 2013). Alternative, e.g. non-thermal, production mechanisms can alter these bounds, but the WDM deficiencies noted in Section 2.1.5 remain.

Self-interacting dark matter (SIDM, Carlson *et al.* 1992; Spergel & Steinhardt 2000) refers to dark matter particles which are, as usual, weakly coupled to the standard model (see Section 2.2), but have strong self-couplings leading to enhanced elastic scattering or self-annihilation cross-sections. Such self-interactions could produce the observed halo cores by thermalization of the DM particle population, if elastic scattering events occur frequently enough, or by particle loss due to annihilation. Models of SIDM are testable via the properties of DM halo cores (e.g. Kuzio de Naray *et al.* 2010), or with observations of merging galaxy clusters: DM self-interactions could lead to a displacement between the dark matter haloes and the (collisionless) galaxies of the colliding clusters. Recent studies of such merger events were conducted by e.g. Dawson *et al.* (2012), Rocha *et al.* (2013) and Kahlhoefer *et al.* (2014).

Modified Newtonian Dynamics (MOND) were introduced by Milgrom (1983) to provide an explanation for the apparent lack of mass seen in galactic rotation curves *without* the need for an unknown type of dark matter. Instead, Newton's law of gravity itself is modified in the regime of weak gravitational fields. This phenomenological modification is able to *describe* the properties of galactic haloes over an impressive range of mass scales (Famaey & McGaugh (2012) provide a recent review), but its physical interpretation remains unclear. In addition, MOND faces observational challenges, for example from cluster merger analyses (like the famous "bullet cluster", Clowe *et al.* 2006) or the power spectrum of the very largest scales of the universe (Dodelson 2011). Famaey & McGaugh (2013) compare the "Challenges for ΛCDM and MOND".

Baryonic forms of dark matter: Astronomical surveys like EROS and OGLE were able to rule out non-luminous "massive compact halo objects" (MACHOs) as the dominant DM component by the lack of observed microlensing events (e.g. Tisserand *et al.* 2007; Wyrzykowski *et al.* 2011). These exclusions, however, depend on the mass of the MACHO object, and primordial black holes (PBH) in the right mass range may also behave similarly to non-baryonic cold dark matter. For example, Griest *et al.* (2013) claim that "there are still about 4 orders of magnitude in mass (from 3×10^{-13} $M_\odot$ to 2×10^{-9} $M_\odot$), where PBH DM (or MACHO DM) can make

up the entirety of the DM."

Such baryonic forms of dark matter face, of course, the restrictions of Big Bang nucleosynthesis, but there are claims that e.g. somewhat exotic forms of QCD dibaryon matter may be able to elude the bounds on the baryon (i.e.: nucleon) content of the universe (Farrar 2003).

Altogether, it is probably fair to state that while these astrophysically motivated alternatives to the "standard" variant of non-baryonic, cold dark matter certainly have their respective merits, they also face difficulties that are comparably severe as those of CDM. New observational input as well as theoretical development appears necessary to approach a resolution of the dispute. For example, solutions to the small-scale DM problems have been proposed (e.g. by van den Aarssen *et al.* 2012) which are grounded in the realm of particle physics, which is the subject of the next section. Inflationary models corresponding to the *BICEP2* results (Ade *et al.* 2014) may also alleviate the ΛCDM small-scale problems by changing the primordial power spectrum (Garrison-Kimmel *et al.* 2014).

2.2 Dark matter particle candidates

Having established the astronomical evidence for *some* type of dark matter, it is an obvious question to ask precisely *what* type of particle this dark matter could be made of. As it turns out, there is no valid DM candidate within the standard model of particle physics, so that the astronomical observation of dark matter may be interpreted as the first unambiguous and perhaps most poignant detection of physics "beyond the standard model" (BSM).

2.2.1 The standard model of particle physics

During the last century, experimental and theoretical advances in subatomic physics have led to a theory that is able to describe all known particles, their interactions and associated phenomena. This theory is called the standard model (SM) of particle physics, and it is certainly an impressive manifestation of mankind's curiosity. (See, e.g., the concise historical reviews by 't Hooft (2007) and Wyatt (2007); comprehensive reviews on *very* many aspects of the SM can be found in Beringer *et al.* 2012.)

The standard model's particle content is depicted in Figure 2.5. It consists of three generations of fermionic quarks and leptons and five sorts of bosons corresponding to the different interactions. These forces are described by Yang-Mills theories based on the principle of local gauge invariance (Yang & Mills 1954), and the corresponding symmetry groups are formed as

$$SU(3)_C \otimes SU(2)_T \otimes U(1)_Y \ . \tag{2.12}$$

Here, the subscript C denotes the *colour* charge of the strong interaction, or quantum chromodynamics (QCD, Gross & Wilczek 1973; Politzer 1973). T and

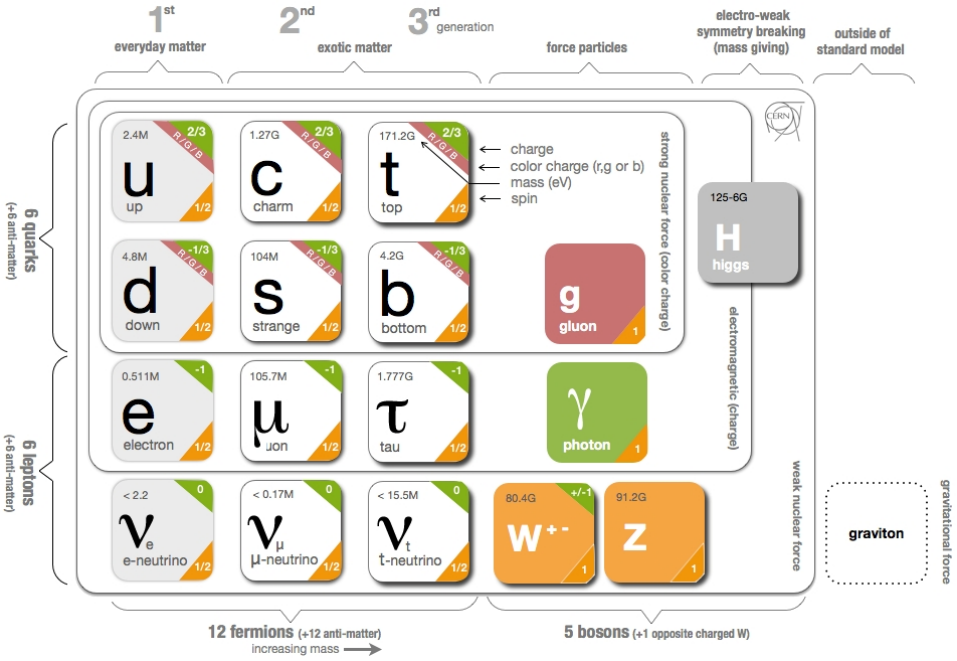

Figure 2.5: The particle content of the Standard Model. Only quarks and gluons carry colours and are subject to the strong interaction, which is mediated by eight different gluons. All electrically charged particles interact via photon exchange; neutrinos only take part in weak interactions, mediated by the W (electrically charged) and Z (electrically neutral) vector bosons. Electroweak symmetry breaking is achieved by the Higgs mechanism, shown here is the associated boson. Only gravity (symbolised by its hypothetical mediator, the graviton) could not yet be included of the standard model of particle physics. Source: http://www.isgtw.org/spotlight/go-particle-quest-first-cern-hackfest

Y stand for weak isospin and hypercharge of the unified electroweak interaction (Glashow 1961; Weinberg 1967; Salam 1968). It was shown rather soon that such gauge theories are renormalizable ('t Hooft & Veltman 1972). However, the symmetry breaking mechanism proposed by Anderson (1963), Englert & Brout (1964), Higgs (1964) and Guralnik *et al.* (1964), which was included in the electroweak theory to allow its massive vector bosons W and Z, was only recently confirmed by the discovery of the "Higgs boson" at the LHC (Chatrchyan *et al.* 2012; Aad *et al.* 2012), see also Cho (2012) and `nobelprize.org/nobel_prizes/physics/laureates/2013/`.

The only well-known force *not* included in the standard model is gravity; this is due to the persistent difficulties in unifying Einstein's theory of general relativity with small-scale quantum mechanics (e.g. Calcagni *et al.* 2013), and to the difficulty to detect a graviton (Rothman & Boughn 2006).

Apart from gravitation, the standard model is at present *sufficient* to describe all known particle physics phenomena. Nevertheless, it is often considered *incomplete* (e.g. Morrissey *et al.* 2012), for several theoretical and experimental reasons:

- There are 26 different free parameters in the SM, which may be considered too large a number. For example, the masses of most particles (which depend on their Yukawa couplings to the Higgs) are not predicted. This problem is related to the fact that there seem to be precisely three generations of quarks and leptons, which is also not predicted by the theory itself.

- The discovery of neutrino oscillations (see Bilenky 2005) has proven that neutrinos are massive, which was originally not anticipated. However, it is unknown whether these masses are of the "Dirac" type (as for the other fermions) or "Majorana" masses, which would mean that neutrinos are their own antiparticles.

- In addition, the standard model does not provide a complete recipe for *baryogenesis*, i.e. the creation of a matter-dominated universe in the Big Bang. This asymmetry between matter and antimatter necessitates CP violation, which was found present in both the quark and lepton sectors, but the exact mechanism for the generation of the asymmetry remains under debate.

- A theoretical problem concerning the Higgs boson is the instability of its mass against quantum corrections, known as the *hierarchy problem* because of the hierarchy of energy scales involved. This is covered in a little more detail in Section 2.2.3.

- Finally, there is no SM candidate for dark matter (see below), and although there are many theoretical ideas to understand primordial inflation and dark energy e.g. in terms of scalar fields (and the associated particles), their incorporation in the standard model of particle physics remains cloudy.

Concerning dark matter, the astronomical evidence mentioned in the previous section shows that any candidate particle most probably needs to have the following set of features: It should be

- neutral, i.e. not interacting electromagnetically;
- cold, i.e. sufficiently massive and slow-moving as to not erase gravitational structures;
- non-baryonic, in order to comply with the nucleosynthesis bounds;
- and perhaps weakly interacting, which would allow thermal DM production in the early universe, see the next section.

None of the particles shown in Figure 2.5 fulfills all these criteria. The neutrinos used to be considered potential dark matter candidates, as they are electrically neutral and formed in the primordial universe, so that there is still a cosmic neutrino background. However, they would form *hot* dark matter, due to their low masses, and their relic density is too low.

2.2.2 The "WIMP miracle"

In contrast to the standard model particles, a *weakly interacting massive particle* (WIMP) could meet the astronomical requirements to be the single constituent of dark matter. Such particles are natural ingredients of various theories beyond the standard model, e.g. supersymmetry, which are described in the following sections. However, all these models share a compellingly simple mechanism for the production of dark matter in the early universe: A particle of mass $\sim 100\,\mathrm{GeV}$, which interacts weakly with SM particles and freezes out from thermal equilibrium after the Big Bang, could produce "just" the right dark matter relic density without any fine-tuning.

As mentioned in Section 2.1.2, today's relic abundance of dark matter has been measured precisely. Planck Collaboration *et al.* (2013a) published several different values, depending on the set of measurements used for fitting the ΛCDM parameters; the value derived from the most inclusive combination is

$$\Omega_{\mathrm{DM}} h^2 = 0.1187 \pm 0.0017, \tag{2.13}$$

where $h = 0.6780 \pm 0.0077$ is the Hubble parameter in units of 100 km s^{-1} Mpc^{-1}. This value of $\Omega_{\mathrm{DM}} h^2$ can be compared with computations of the relic density of WIMPs (see e.g. Feng 2010, and references therein). These computations are performed as follows: In the early universe, the dark matter is assumed to be in thermal and chemical equilibrium with the rest of the primordial plasma. Dark matter particles are continually destroyed by self-annihilation, but also created from standard model particles by the opposite processes. For weakly interacting particles, these processes are mediated by W or Z exchange; often, the choice of

a particular BSM physics model allows to calculate these reaction rates precisely (e.g. Gondolo *et al.* 2004).

Then, dark matter drops out of chemical equilibrium due to the falling temperature of the universe. SM particles no longer have enough energy to produce dark matter particles in collisions, and the number density of DM particles declines, roughly when $T \sim m_{\mathrm{DM}}/20$. However, this effect is counteracted by the expanding universe, which dilutes the DM density so strongly that the rate of self-annihilation events falls close to zero. Henceforth, the comoving number density of dark matter particles stays almost constant.

Figure 2.6 shows this dark matter "freeze-out" for different self-annihilation cross-sections. Calculations show that the relic density does not depend strongly on the *mass* of the dark matter particle. Therefore, the necessary annihilation cross-section, which is usually given in its velocity-averaged form $\langle \sigma v \rangle$, can be approximated by the formula

$$\Omega_{\mathrm{DM}} h^2 \approx \frac{3 \times 10^{-27}\ \mathrm{cm^3 s^{-1}}}{\langle \sigma v \rangle}\,, \tag{2.14}$$

so that the measured density $\Omega_{\mathrm{DM}} h^2 \approx 0.1$ is achieved by the "thermal" value of $\langle \sigma v \rangle = 3 \times 10^{-26}\ \mathrm{cm^3 s^{-1}}$. This number is not strictly fixed: Apart from the remaining mass dependence, velocity-dependent annihilation processes or co-annihilation with other BSM particles may change the thermal history of the dark matter density. In addition, *non*-thermal DM production can provide the correct relic density if the annihilation rate were otherwise too high. Nonetheless, this thermal self-annihilation cross-section provides a standard scale against which BSM physics models, but also the sensitivities of dark matter searches are often weighed.

Finally, it should be noted that the *chemical* decoupling of dark matter, i.e. the point when the production and annihilation rates start to differ, may be different from its *kinetic* decoupling, as elastic collisions can keep the dark matter thermalized even though it is out of chemical equilibrium (e.g. Bringmann 2009). However, this mainly affects the small-scale cutoff of dark matter structures (see Section 2.1.2), rather than its relic abundance.

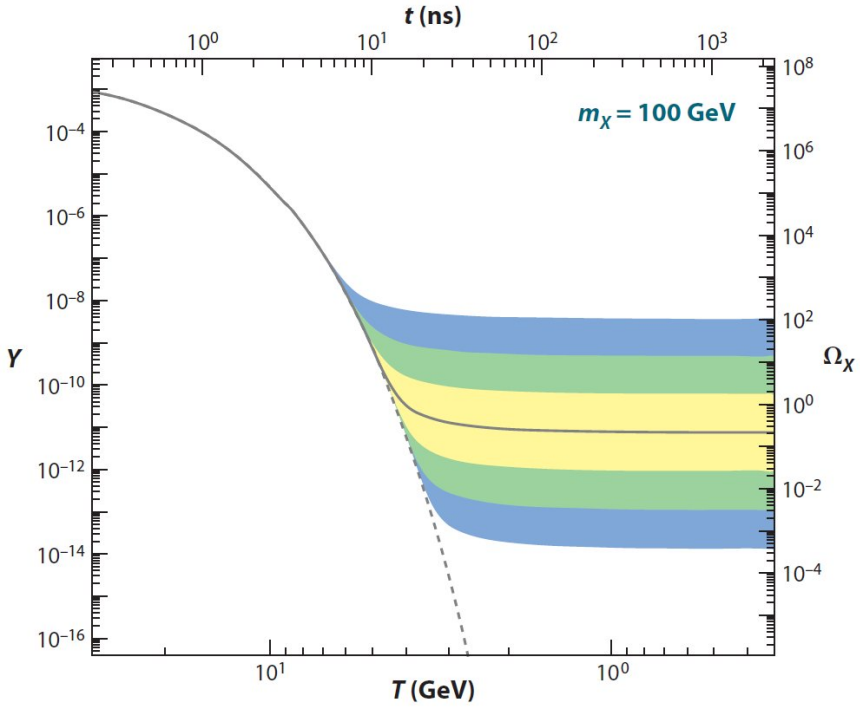

Figure 2.6: Thermal freeze-out of a dark matter particle with mass $m_\chi = 100\,\mathrm{GeV}$, leading to the relic density Ω_χ. The horizontal axes show the temperature T and age t of the universe, respectively. The left axis shows the comoving number density Y of DM particles. The solid line denotes the Y evolution for an annihilation cross-section leading to the correct dark matter relic density, while the shaded areas indicate cross-sections which are factors 10, 100 and 1000 smaller or larger than this "thermal" value. From Feng (2010)

2.2.3 Supersymmetry

The most extensively studied framework for physics beyond the standard model is probably supersymmetry (SUSY, Wess & Zumino 1974). It provides a connection between the fermionic (matter) part of the particle spectrum and the bosonic gauge force mediators. At the same time, it relates the Lorentz space-time symmetry of special relativity to the internal symmetries and quantum numbers of particles. In addition, it provides a very reasonable dark matter candidate and helps to solve the hierarchy problem (see below), which may explain the ongoing interest in this theory despite the complete lack of experimental evidence for SUSY[6]. There is an impressive amount of literature on supersymmetry. References to many early publications can be found in a recent review on BSM searches at the LHC by Parker (2013); a popular theoretical "primer" was provided by Martin (1998).

One particular prediction of SUSY is that every standard model particle should have a supersymmetric partner of the same mass, but different spin. The SM fermions, leptons and quarks, have bosonic partners branded "sleptons" and "squarks", while the SM (gauge) bosons acquire fermionic partners labelled with the ending "-ino", e.g. the "wino". The Higgs particle is a special case, as SUSY requires *two* Higgs doublets for technical reasons, which results in a total of five different Higgs particles. The lightest of these, however, behaves similarly to the standard model Higgs.

Obviously, this symmetry is broken: No superparticles have been found experimentally, so they must have higher masses than the SM particles, if they exist at all. Several different mechanisms have been proposed for this breaking of supersymmetry, and many of them also attack the large number of additional free parameters (like particle masses and couplings) that broken SUSY otherwise contains. However, all of these models need to allow sparticle masses in the TeV mass range, if SUSY is supposed to solve the *hierarchy problem* (e.g. Susskind 1979) of the standard model.

The hierarchy problem

A scalar particle like the Higgs receives quantum corrections to its mass (Δm) which are quadratic in the renormalization cut-off scale[7] Λ_{cut}, due to loop processes as shown in the left panel of Figure 2.7:

$$\Delta m_H^2 \sim \frac{\lambda^2}{16\pi^2} \int^{\Lambda_{\mathrm{cut}}} \frac{d^4 p}{p^2} \sim \frac{\lambda^2}{16\pi^2} \Lambda_{\mathrm{cut}}^2 \,. \tag{2.15}$$

Here, λ is a dimensionless coupling, p denotes the four-momentum of the quark, and the integration should be performed over all possible loop momenta[8]. Therefore, the scale Λ_{cut} is introduced to mark the cut-off at which the standard model

[6] Hopes for SUSY detection, however, have been growing for quite some time: Ellis (1985)
[7] not to be confused with the cosmological constant Λ
[8] The description here follows Feng (2010).

description is no longer adequate; for example, this may be the "Planck scale" $\Lambda_{\text{Pl}} = G_N^{-1/2} \sim 10^{19}$ GeV at which gravity becomes comparable in strength to the other forces.

This technique yields mathematically sensible results; however, if the Planck scale is chosen as a cut-off, the bare mass of the Higgs must be fine-tuned over 38 orders of magnitude in order to balance these quadratic corrections and keep the measured mass at its value of 125 GeV. Therefore, this has become known as the *fine-tuning* or *hierarchy* problem, due to the stark hierarchy of energy scales involved.

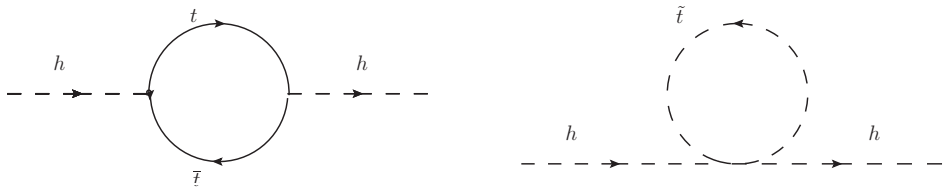

Figure 2.7: Quantum corrections to the mass of the Higgs boson. Left: fermion loop involving a top quark t. Right: scalar loop involving a stop squark $\tilde{t}$. (SUSY particles are usually marked with a tilde.)

Supersymmetry, on the other hand, alleviates this instability of the Higgs mass: The scalar superpartners of SM particles, e.g. the stop squark $\tilde{t}$, generate quantum corrections (Figure 2.7, right panel) which are opposite in sign to the standard model ones. If the sparticles had the same mass as their SM particles, this cancellation would be exact; since they don't, a residual correction remains which is logarithmic in the scale ratio:

$$\begin{aligned}\Delta m_H^2 &\sim \frac{\lambda^2}{16\pi^2}\int^{\Lambda}\frac{d^4p}{p^2}\bigg|_{\text{SM}} - \frac{\lambda^2}{16\pi^2}\int^{\Lambda}\frac{d^4p}{p^2}\bigg|_{\text{SUSY}} \\ &\sim \frac{\lambda^2}{16\pi^2}\left(m_{\text{SUSY}}^2 - m_{\text{SM}}^2\right)\ln\left(\frac{\Lambda_{\text{cut}}}{m_{\text{SUSY}}}\right).\end{aligned} \tag{2.16}$$

This logarithmic factor is less than one hundred, making the fine-tuning problem much less severe. However, this mechanism only works if the superpartner masses are not too different from those of their standard model counterparts. Since the Higgs couplings are proportional to the particle masses and the top is the most massive quark, a *stop* squark at the TeV scale could provide such cancellations.

SUSY dark matter

While the above-mentioned *raisons d'être* for supersymmetry are based on the grounds of particle physics, SUSY also provides a compelling candidate for dark matter. In order to prevent the violation of baryon and lepton number (and hence, proton decay) in SUSY processes, the theory contains a new symmetry which

differentiates between supersymmetric and standard model particles. It is called R-parity[9] and defined as

$$P_R = (-1)^{2s+3B+L}\,, \tag{2.17}$$

with spin s and baryon/lepton numbers B and L, so that SUSY particles carry R-parity $P_R = -1$ and non-SUSY particles have $P_R = +1$. Since R-parity is a conserved quantity, supersymmetric particles can only be produced or annihilated in even numbers. Therefore, the lightest supersymmetric particle (LSP) cannot decay to SM particles, and if it is produced at the high temperatures in the early universe, it can serve as an "ideal" dark matter particle candidate. (See, e.g., Goldberg (1983) and Ellis *et al.* (1984), or the reviews by Jungman *et al.* (1996) and Bertone *et al.* 2005.)

One particularly good DM candidate is the lightest *neutralino*, often labelled $\tilde{\chi}_0$ or simply χ. In the "minimal supersymmetric standard model" (MSSM), defined by the minimal additional particle content with respect to the SM, there are four mixing neutral fermion fields: The superpartners of the standard model B and W_3 fields and those of the two scalar neutral Higgs particles. From these fields emerge four Majorana mass eigenstates, the neutralinos. The lightest of these can be expressed as

$$\chi = N_{11}\tilde{B} + N_{12}\tilde{W}_3 + N_{13}\tilde{H}_1^0 + N_{14}\tilde{H}_2^0\,, \tag{2.18}$$

where the mixing angles depend on electroweak parameters, see e.g. Appendix A of Bertone *et al.* (2005). They are not given *a priori*, but they determine neutralino properties like the self-annihilation cross-section and the production rates of different final state particles. Therefore, it is customary to talk about the "bino", "wino" or "higgsino" content of the neutralino.

The neutralino is not the only possible DM candidate in supersymmetry. The gravitino, the SUSY partner of the graviton, would be very hard to detect experimentally, as it only interacts gravitationally. Nevertheless, it is a popular candidate for long-lived, decaying dark matter models based on P_R violation (e.g. Takayama & Yamaguchi 2000; Lola 2011). The sneutrino, on the other hand, seems excluded by direct searches (see Section 2.3) due to its rather strong nucleon-scattering cross-section.

2.2.4 Other models of particle CDM

It must be noted that there are many other particle models for cold dark matter, see e.g. Feng (2010) or Bertone (2010). Compactified extra dimensions, for example, could solve the hierarchy problem by lowering the cut-off scale $\Lambda_{\rm cut}$ to a few TeV. These *Kaluza-Klein* (KK) models (Kaluza 1921; Klein 1926) predict "towers" of excited states for each standard model particle, each state having a mass that depends on the compactification radius of the additional dimension(s). The *lowest*

[9] Originally, R-parity was defined in the framework of non-supersymmetric "grand unified theories", which also would have allowed proton decay processes.

of such states could also be stable, and hence dark matter candidate particles (Kolb & Slansky 1984). Servant & Tait (2003) have shown that the lightest excitation of the standard model B field is a valid CDM candidate if it has a mass in the TeV range. Abramowski *et al.* (2012), for example, have searched for γ-ray signals from the self-annihilation of such a "lightest Kaluza-Klein particle" (LKP). See also Hooper & Profumo (2007) for a review of the dark matter phenomenology of universal extra dimensions.

Another interesting cold dark matter candidate is the *axion*, originally proposed to solve the "CP problem" of QCD (see, e.g., the review by Ringwald 2012). It is a very light (sub-eV) pseudoscalar with very weak couplings to SM particles, but if produced non-thermally in the early universe, it can indeed provide the correct relic density and dark matter distributions which behave similar to WIMPs (reviews by Bradley *et al.* 2003; Duffy & van Bibber 2009). Experimentally, however, it is only indirectly accessible to γ-ray astronomy (see e.g. Horns *et al.* 2012; Meyer *et al.* 2013), therefore it is not covered any further in this work.

2.3 Methods of WIMP detection

While the astrophysical evidence for cold dark matter is compelling (Section 2.1), the detection of dark matter *particles* is still an important open issue in fundamental physics. It is generally believed that a *complementary* approach is necessary to unambiguously identify any (or, *the*) dark matter particle (e.g. Bechtle *et al.* 2012; Arina *et al.* 2013). Figure 2.8 sketches the three different pathways used for this endeavour, concentrating on WIMP dark matter:

- First, dark matter could be produced in the collision of standard model particles at facilities like the LHC (see e.g. Mitsou 2013). Typically, the experimental signature of DM production is missing transverse momentum, as both WIMPs escape the detector without interacting. The missing p_T must be balanced by the initial-state or final-state radiation of quarks or bosons in order to be detectable (see Birkedal *et al.* 2004). Of course, higher-level searches for theoretical models like supersymmetry may also provide information on the dark matter particle, if the model parameters can be sufficiently constrained, e.g. if there is a clear experimental signature of neutralino production.

- Secondly, *direct detection* experiments aim to measure the recoil energy from elastic collisions of WIMPs with the detector material, e.g. liquid noble gases (e.g. Aprile *et al.* 2012; Akerib *et al.* 2014). These experiments directly probe the local, astrophysical dark matter density. Therefore, the interpretation of their results depends on the knowledge of this value (commonly assumed to be about 0.2–0.4 GeV cm^{-3}, Nesti & Salucci 2013; Read 2014), but also on the phase-space distribution of dark matter particles at the Earth's location in the Milky Way, which has to be inferred from theoretical models (see

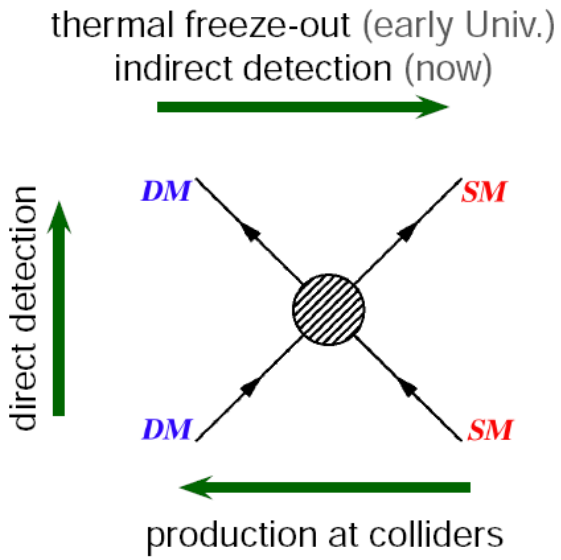

Figure 2.8: A sketch of possible interactions between dark matter and standard model particles, corresponding to different methods of DM detection. See text for more details. Source: `mpi-hd.mpg.de/lin/research_DM.en.html`

e.g. Lee *et al.* 2014). The sensitivity of current experiments has reached the "expected" parameter space of SUSY dark matter models, and indeed there have been claims of detected signals consistent with dark matter; however, none of these were confirmed by other experiments yet. For example, the detection of an annular signal modulation at the DAMA/LIBRA experiment (Bernabei *et al.* 2008) has been interpreted as evidence for dark matter with a mass of a few GeV, but this claim is in apparent conflict with the results of other experiments, e.g. Aprile *et al.* 2012; Agnese *et al.* 2013; Akerib *et al.* 2014.

- Finally, there is the possibility to detect dark matter *indirectly* by observing the products of its self-annihilation or decay in space. Observations in γ-rays are treated in the next subsection; apart from these, neutrinos (e.g. Aartsen *et al.* 2013) or charged antiparticles (e.g. Aguilar *et al.* 2013; Bergström *et al.* 2013) could serve as *messenger* particles signalling WIMP annihilations. In contrast to charged particles, which are deflected by cosmic magnetic fields, γ-rays and neutrinos might also be used to trace the *distribution* of dark matter in and around the Milky Way or other galaxies. However, this would only be possible if dark matter annihilation signals were actually detected — so far, no undisputed signal has been found. Porter *et al.* (2011) review dark matter searches using astroparticle observations.

There are other types of dark matter searches which do not easily fit into these categories: For example, constraints on the self-annihilation cross-section can

be derived from CMB data, due to the injection of energy into the primordial plasma around the time of recombination (e.g. Padmanabhan & Finkbeiner 2005; Madhavacheril *et al.* 2013). WIMP annihilation to highly energetic electrons could be observable in the radio signal produced by synchrotron radiation in (inter-) galactic magnetic fields (e.g. Egorov & Pierpaoli 2013; Storm *et al.* 2013). The decay of sterile neutrinos, acting as warm dark matter, could produce a sharp keV photon line observable in X-rays (e.g. Borriello *et al.* 2012). A number of other, non-SUSY and non-KK WIMPs and their possible modes of detection are reviewed by Feng (2010); Strigari (2013) considers direct and indirect dark matter detection in more depth. The remainder of the present work, however, is dedicated to neutralino detection in very high energy γ-rays, which is the topic of the next subsection.

2.3.1 γ-rays from dark matter annihilations

The idea that the self-annihilation of dark matter particles may produce observable γ-rays can be traced back a long time, see e.g. Gunn *et al.* (1978). Searches for such a signal have gained momentum with the latest generation of ground-based TeV γ-ray observatories (see the next chapter), and satellite observatories like *Fermi*-LAT (Atwood *et al.* 2009). The *decay* of WIMP dark matter may also yield γ-ray signals, but is neglected in the present work. For reviews of indirect DM searches in γ-rays, see e.g. Bringmann & Weniger (2012) or Funk (2013); an overview of published results from Cherenkov telescopes was gathered by Doro (2014).

Typically, these searches are performed using observations of particular astronomical objects which are considered promising sources of a WIMP annihilation signal. For example, the centre of the Milky Way has been the subject of considerable attention (e.g. Aharonian *et al.* 2006a; Abramowski *et al.* 2011b; Belikov *et al.* 2012), as it is relatively close and has a high dark matter density. However, the exact amount and the density profile of dark matter in the Galaxy is still disputed (e.g. Nesti & Salucci 2013; Burch & Cowsik 2013). Another drawback of Galactic centre observations is the strong background of astrophysically produced γ-rays. Therefore, the dwarf spheroidal galaxies surrounding the Milky Way are also considered promising targets: They are less massive and further away than the Galactic centre, but almost background-free (Chapter 4). Finally, clusters of galaxies have been chosen as targets for dark matter searches, as they are the richest dark matter structures in the universe and therefore may provide an observable signal despite their distance. DM substructures within clusters may additionally boost their signal, see Chapter 5.

Apart from these target types, the dark matter contribution to the diffuse extragalactic γ-ray background has also been analyzed (e.g. Bringmann *et al.* 2014). In order to detect or constrain a DM signal in the diffuse flux, however, all other contributing sources have to be modelled precisely. Such sources could be the populations of blazars and millisecond pulsars below the flux threshold for individual detections.

None of these searches have yielded unambiguous detections of a dark matter signal. Therefore, the observations are commonly used to derive limits on the parameters of theoretical dark matter particle models. Two ingredients are necessary to perform such limit calculations: First, it is mandatory to estimate the amount and distribution of dark matter in the target object. As dark matter is assumed to annihilate in pairs, the corresponding γ-ray flux scales with the *squared* dark matter density ρ^2_{DM}. Therefore, the uncertainties on this quantity (see Section 2.1.4) strongly influence dark matter limit computations.

Secondly, the γ-ray energy spectrum $\mathrm{d}N_\gamma/\mathrm{d}E_\gamma$ resulting from dark matter annihilations must be predictable from the DM particle model. Here, different SUSY models have been particularly predictive: See, e.g., Bergström *et al.* (1998), Gondolo *et al.* (2004) or Cembranos *et al.* (2011).

Together, these two quite different pieces of information make it possible to predict the energy-differential γ-ray flux from dark matter annihilations:

$$\frac{\mathrm{d}\Phi(\Delta\Omega, E_\gamma)}{\mathrm{d}E_\gamma} = \frac{1}{4\pi} \underbrace{\frac{\langle\sigma v\rangle}{2m^2_{\mathrm{DM}}} \frac{\mathrm{d}N_\gamma}{\mathrm{d}E_\gamma}}_{\text{particle physics}} \times \underbrace{\bar{J}(\Delta\Omega)\Delta\Omega}_{\text{astrophysics}} . \tag{2.19}$$

Here, the astrophysical information about the dark matter density is incorporated in the $\bar{J}$ factor, or "halo factor", which is the line-of-sight integral over ρ^2 averaged within the solid angle $\Delta\Omega = 2\pi\left(1 - \cos\vartheta_{\mathrm{max}}\right)$ of the observation:

$$\bar{J}(\Delta\Omega) = \frac{1}{\Delta\Omega} \int_{\Delta\Omega} \mathrm{d}\Omega \int_{\mathrm{l.o.s.}} \mathrm{d}\ell\ \rho^2_{\mathrm{DM}}(r(\ell)) . \tag{2.20}$$

In Equation 2.20, the variable ℓ parametrizes the line of sight (l.o.s.), while r is the radial distance from the centre of the target object. Hence, $r^2 = \ell^2 + D^2 - 2D\ell\cos\vartheta$, where D is the distance of the object and ϑ the angle between D and ℓ. Frequently, the l.o.s. integration is artificially bounded, e.g. at the tidal radius of the dark matter halo. Please note that in Chapter 4 and Appendix B, the quantity

$$J(\Delta\Omega) = \bar{J}(\Delta\Omega) \times \Delta\Omega \tag{2.21}$$

is used, following the nomenclature of other publications.

The halo factor is commonly given in units of $\mathrm{GeV^2cm^{-5}}$. Its numerical value can differ by orders of magnitude, depending on the observation target and on the assumed dark matter halo profile. For example, a reasonable value for observations of the Galactic center is $\bar{J} \sim 10^{25}\ \mathrm{GeV^2cm^{-5}}$ (Bergström *et al.* 1998; Doro *et al.* 2013), dwarf spheroidal galaxies may have halo factors up to $\bar{J} \sim 10^{24}\ \mathrm{GeV^2cm^{-5}}$ (Chapter 4), and the Fornax galaxy cluster yields $\bar{J} \sim 10^{22}\ \mathrm{GeV^2cm^{-5}}$ (Chapter 5). However, the $\bar{J}$ factor is often not well constrained, and the assumption of a fixed $\bar{J}$ value should be avoided. Chapter 4 presents a more appropriate procedure which takes into account the sizeable uncertainties of the $\bar{J}$ factors.

The γ-ray spectrum from DM annihilations

The other ingredient which determines the γ-ray flux is given by the particle physics model of dark matter. Typically, mass m_{DM} and self-annihilation cross-section $\langle \sigma v \rangle$ are left as free parameters in dark matter searches. The photon spectrum, on the other hand, depends on the final state particles of the annihilation process and can be calculated if the different couplings are given by the model. For example, *wino* dark matter, i.e. a neutralino with a dominant $\tilde{W}$ component, annihilates predominantly to $W^{\pm}$ bosons. Figures 4.3 and 5.11 show γ-ray spectra from DM annihilations to different final states[10].

Generally, the γ-ray spectrum consists of the three different components shown in Figure 2.9:

- The bulk of the photons, particularly at lower energies, is produced by decay products of the final-state particles. For example, DM annihilation to W, τ or quark pairs results in hadronic jets containing π^0 mesons, which decay almost exclusively to photons. The γ-ray spectra from such processes are often calculated with the use of QCD Monte Carlo generators like PYTHIA, see e.g. Cembranos *et al.* (2013). Several authors have provided analytical approximations to the resulting spectra, e.g. Bergström *et al.* (1998) for the case of annihilation to W and Z bosons.

- *Virtual internal bremsstrahlung* (VIB, e.g. Bringmann *et al.* 2008) and initial/final state radiation (ISR/FSR) are processes where a photon is radiated off a charged particle in the internal or the external legs of the annihilation process. Such radiation is generally suppressed by one power of the electromagnetic coupling constant α, but may nevertheless yield a significant photon flux close to the DM particle mass, due to the lifting of helicity suppression.

- Finally, direct annihilations of dark matter to two photons or a photon and a Z boson is possible via loop processes. These are suppressed by a factor $\propto \alpha^2$, but if detected, they would provide a "smoking gun" signal for DM annihilations. In the case of annihilation to two photons, the γ-ray energy is precisely $E_\gamma = m_{\mathrm{DM}}$, since the relative motion of the DM particles is negligible. Such a "line" signal would be very untypical for any astrophysical background process, and it would indicate the dark matter particle mass. Therefore, many searches have been performed, e.g. by Weniger (2012), Ackermann *et al.* (2013) and Abramowski *et al.* (2013).

Another aspect of the "particle physics" part of Equation 2.19 is the suppression of the γ-ray flux for higher dark matter masses, scaling (approximately) with m_{DM}^{-2}. This suppression is due to the smaller number density of DM particles

[10] A brief description of how different SUSY models (in the mSUGRA framework) determine the neutralino contents and thus the dominant annihilation channels can be found in the study by Colafrancesco *et al.* (2006).

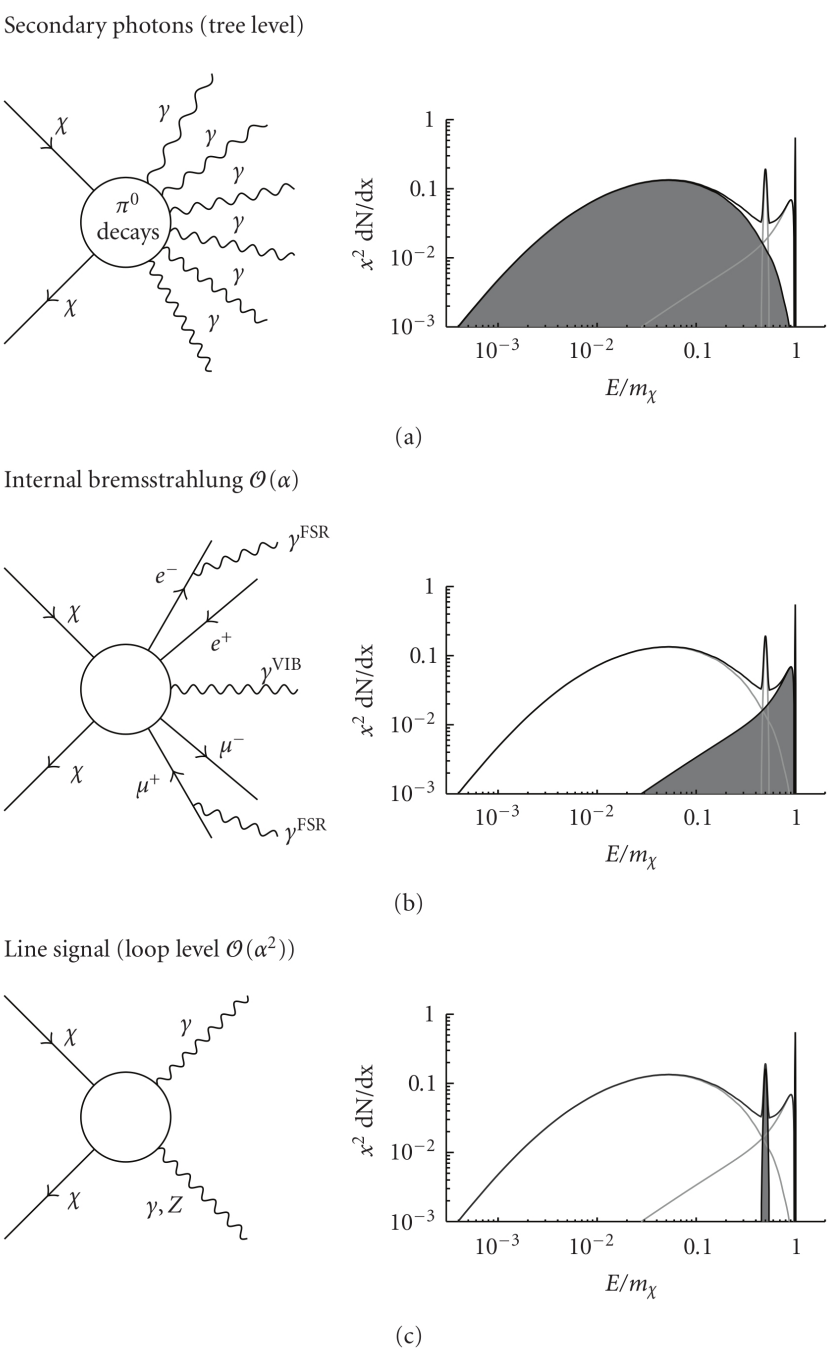

Figure 2.9: The three "ingredients" of the γ-ray spectrum from dark matter annihilations: a), secondary photons from the decay of final state particles. b), internal bremsstrahlung and final-state photon radiation. c), direct annihilation to two photons or a pair of γ and Z via loop processes. Plotted on the right is the γ-ray spectrum weighted with x^2, where $x = E_\gamma / m_{\mathrm{DM}}$. From Kuhlen (2010)

at fixed halo mass density, and it reduces the detectability of high-mass dark matter considerably. Figure 2.10 shows the differential γ-ray flux from annihilations of DM particles with masses of 0.1, 1 and 10 TeV, using the photon spectrum approximation by Bergström *et al.* (1998). Even though the number of photons per annihilation event is larger for higher DM particle masses, the γ-ray flux in the energy range below 100 GeV (accessible e.g. with *Fermi*-LAT) is reduced by orders of magnitude.

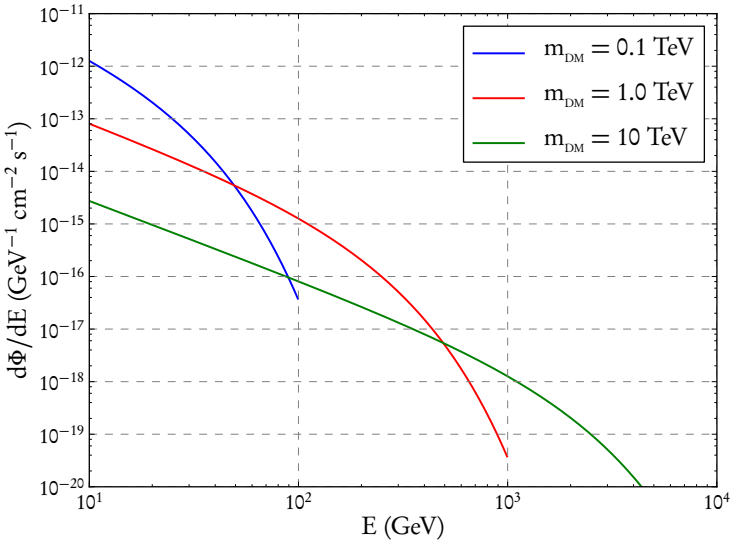

Figure 2.10: The differential γ-ray flux from dark matter annihilations: Suppression with m_{DM}^{-2}. Fluxes for different DM particle masses were calculated using the thermal annihilation cross-section $\langle\sigma v\rangle = 3 \times 10^{-26}$ cm^{3}s^{-1} and the halo factor $\bar{J} = 10^{25}$ GeV^{2}cm^{-5}. The γ-ray spectrum is approximated with the parametrization by Bergström et al. *(1998).*

The conventional way of calculating *upper limits* on the self-annihilation cross-section $\langle\sigma v\rangle$ from non-detections of dark matter in γ-ray observations is described in Section 5.3.2. A methodological alternative is shown in Section 4.3.2.

Chapter 3

Imaging Air Cherenkov Telescopes

The intriguing phenomenon of *cosmic rays* was discovered more than 100 years ago by Victor Hess[1]. Today, it remains a topic of considerable theoretical and observational effort, see e.g. Beringer *et al.* (2012), Chapter 26. The flux of *charged* cosmic rays spans many orders of magnitude in both the particle energy and the number of particles hitting the Earth's atmosphere. Over the energy range from a few GeV to more than 100 TeV, the energy-differential flux of charged nucleons, dominantly protons, follows a power law with index $\Gamma \approx 2.7$. At $E = 1$ TeV, it was measured by the PAMELA (Adriani *et al.* 2011) and AMS-02 (Consolandi 2014) experiments to be $\mathrm{d}N_p/\mathrm{d}E \approx 8 \times 10^{-9}$ cm^{-2} s^{-1} sr^{-1} GeV^{-1}.

These charged CRs are deflected by the magnetic fields within and beyond the Milky Way, so that they arrive on Earth almost isotropically[2]. In contrast, *γ-rays* and *neutrinos* trace back to their source. More specifically, they travel along geodesics: Cheung *et al.* (2014) have used the *Fermi* satellite to observe a γ-ray signal that was deflected by a gravitational lens.

Neutrinos are weakly interacting particles, so that large detector volumes are necessary for their observation and clear cosmogenic signals are hard to find (e.g. IceCube Collaboration 2013). Observations in γ-rays, on the other hand, have been very fruitful: For example, it was possible to spatially resolve CR acceleration sites in supernova remnants (e.g. Aharonian *et al.* 2004). While the cosmic γ-ray flux up to energies of a few hundred GeV can be measured with satellite observatories like *Fermi*-LAT (Atwood *et al.* 2009), the *very high energy* (VHE) range from roughly 100 GeV to above 100 TeV is only accessible with ground-based telescopes having much larger collection areas. The *Whipple* telescope in Arizona allowed the first unambiguous detection of a VHE γ-ray source, the Crab Nebula (Weekes *et al.* 1989). In the years after that, and particularly during the last decade, several large collaborations have constructed *arrays* of such imaging air Cherenkov

[1] See the commemorating volume edited by Walter *et al.* (2014).
[2] Anisotropies at the 10^{-3} level remain, see e.g. Amenomori *et al.* (2006).

telescopes (IACTs). Observations with H.E.S.S., MAGIC and VERITAS were used for the work presented in Chapters 4 and 5, therefore these instruments are described in the following sections. This chapter is intended to provide a broad overview of VHE γ-ray detection and analysis techniques, with special emphasis placed on the H.E.S.S. instrument; more detailed information on the analysis of the Fornax cluster observations can be found in Chapter 5.

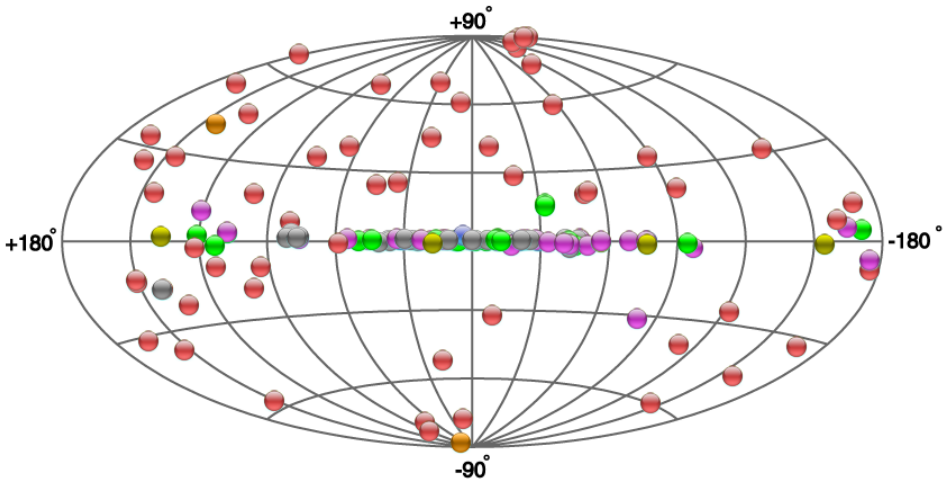

Figure 3.1: VHE γ-ray sources, status on 25/02/2014. Shown is an all-sky view in Mollweide projection. The colours indicate different source types. Red: Active galactic nuclei, purple: pulsar wind nebulae, green: supernova remnants, yellow: Galactic binary systems, brown: starburst galaxies, grey: dark/unidentified sources, blue: other sources. From `tevcat.uchicago.edu`

Figure 3.1 shows a collection of presently known VHE γ-ray sources, whose number has surpassed 100 just a few years ago. The different source classes and astrophysical relevances of these observations are described in many excellent review articles, recent ones are e.g. those by Holder (2012) or Rieger *et al.* (2013). Hillas (2013) covers the historical development of TeV γ-ray observations and analysis techniques, and Hinton (2009) includes a concise, but informative description of the properties of the Cherenkov light used for their detection.

Before concentrating on VHE γ-rays, their detection and analysis, it should be noted that IACTs have also been used to perform measurements of the cosmic ray proton (Aharonian *et al.* 1999) and electron flux, e.g. by Aharonian *et al.* (2008, 2009) and Borla Tridon *et al.* (2011).

3.1 VHE γ-rays and their detection

Very high energy γ-rays entering the Earth's atmosphere initiate particle showers, produced by the alternating processes of electron-positron pair production and bremsstrahlung. Charged particles traversing a medium faster than the speed

of light cause the emission of Cherenkov radiation (see Cherenkov 1937, 1986), a condition fulfilled in air by electrons with energies larger than 20–40 MeV, depending on the atmospheric height[3]. This Cherenkov light is emitted at an angle ϑ_c which depends on the relative particle velocity $\beta = v/c_0$, where c_0 is the speed of light in vacuum, and the material's refractive index n:

$$\cos\vartheta_c = \frac{1}{\beta n}\,. \tag{3.1}$$

In the atmosphere, this angle is about $\vartheta_c \sim 1°$, depending on the atmospheric height. As the maximal shower development occurs about 10 km above sea level (a.s.l.), the Cherenkov light from vertically incident γ-rays illuminates a ground area of about 130 m radius at typical observation heights of about 2000 m. Figure 3.2 shows a sketch of such a light cone and its detection with telescopes. Roughly speaking, the shower will be detected by a telescope anywhere within the light cone; thus, a small number of telescopes can cover an effective collection area of about 10^5 m^2, much larger than what is possible with satellite missions.

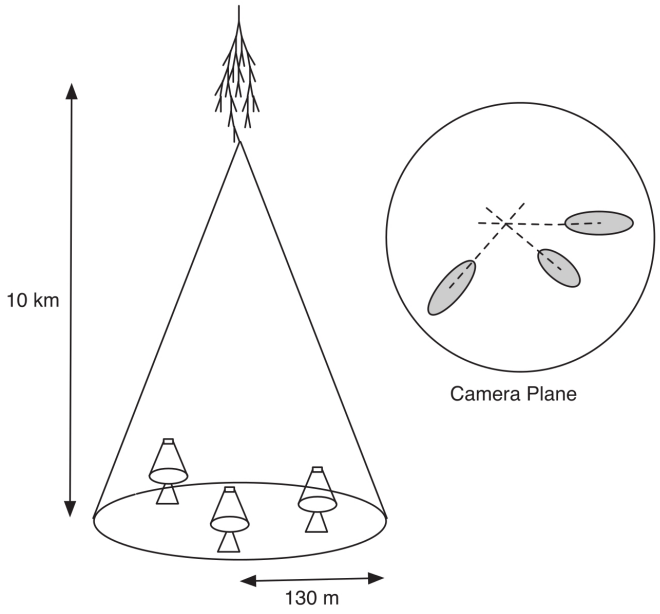

Figure 3.2: Schematic picture of a γ-ray-initiated air shower and the detection of its Cherenkov light. Shown in the "Camera Plane" is a superposition of the shower images recorded by three separate *cameras. From Holder (2012)*

Cherenkov light is predominantly blue and ultraviolet (UV). Its spectrum is proportional to λ^{-2}, with a UV cutoff depending on the dielectric properties of the medium. While UV light is strongly absorbed by the atmosphere, the blue part is transmitted, so that optical mirrors can be used for the collection

[3]The description here follows Hinton (2009).

of Cherenkov photons. The light yield at an elevation of ~ 2 km a.s.l. is about 100 optical photons per square meter and TeV of primary γ-ray energy, and about 100 photoelectrons must be recorded in the telescope to allow reconstruction of the shower image. Therefore, taking into account the typical instrumental efficiency of roughly 10%, a mirror size of about 100 m^2 per telescope is necessary to record 100 GeV γ-ray showers.

The Cherenkov light pulses from air showers last only a few nanoseconds, making fast cameras a necessity for their detection against the night sky background. In most current IACTs, photomultiplier tubes (PMTs) are used, with a pixelisation of about 0.1° opening angle allowing sufficient reconstruction of the shower image. (A more modern detection concept is followed by the FACT collaboration, see Anderhub *et al.* 2011.)

The energy deposited in Cherenkov photons is proportional to the total track length of all charged shower particles, which in turn is proportional to the energy of the primary γ-ray. Since the photon density is roughly constant within the light cone, the detection of air showers in Cherenkov light allows the determination of the primary γ-ray energy with a precision of 10–20% per event, the statistical uncertainty being related to fluctuations of the electromagnetic showers. A calibration of the energy scale can be performed using muon events, which produce rings of Cherenkov light in the telescope camera and whose light yield can be predicted. However, a systematic uncertainty of about 20% remains, because the absorption of Cherenkov light in the atmosphere has to be extracted from Monte Carlo (MC) simulations using generic models of the atmospheric conditions[4].

Nonetheless, *stereoscopic* observations in particular (see the next sections) allow a precise reconstruction of the primary γ-ray direction and the impact distance of the air shower, which affects the relation between the primary energy and the shower image. Thus, a relative uncertainty of about 15% on the energy reconstruction and a directional uncertainty of $\sim 0.1°$ *per event* have become the current observational standard.

The main challenge to VHE γ-ray observations is the background from hadronic cosmic ray events, which also produce air showers and Cherenkov light. Observational methods to estimate and reduce this background are discussed in the next section.

3.1.1 Background suppression and estimation

In Cherenkov telescope observations, air shower events from hadronic cosmic rays, i.e. mainly protons, outnumber the γ-ray events by large factors. For example, about 1000 times more CR events are recorded in the field of view when compared to a strong, Crab-like γ-ray source. Therefore, VHE γ-ray astronomy requires a strong reduction of this CR background, as well as a reliable estimation of the

[4]However, Meyer *et al.* (2010) have performed a cross-calibration of IACTs and the beam-calibrated *Fermi*-LAT telescope via observations of the Crab Nebula.

remaining contamination of the γ-ray signal sample. This is achieved by three steps of data analysis:

Event classification and γ-hadron separation. In the mid-1980s, Monte Carlo simulations of air showers and their Cherenkov light showed that γ-initiated and hadronic events produce quite different optical images, if recorded with a sufficiently fine-grained camera (Stepanian *et al.* 1983; Hillas 1985). Figure 3.3 shows two examples of simulated air shower images: It is visible that the purely electromagnetic shower from a γ-ray is more regular and narrower than the hadronic shower from a CR proton, in which pions with large transverse momentum are produced. Hence, the shape of the shower image can be used to differentiate between "γ-like" and "hadron-like" events. The "Hillas parametrization" of width, length and orientation of the shower image is still widely in use (see Figure 3.3 and Hillas 1996).

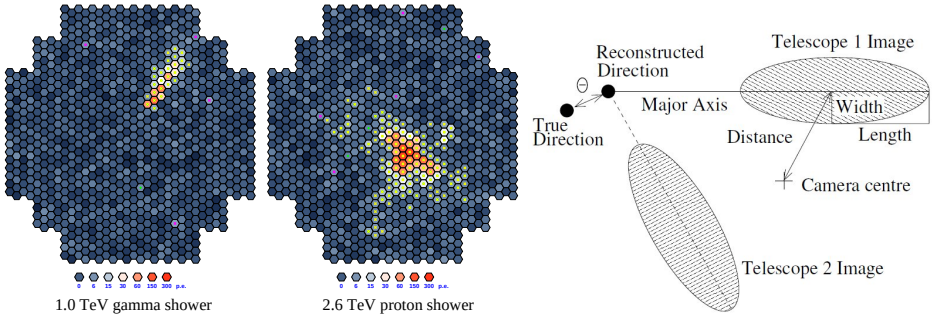

Figure 3.3: Simulated air shower camera images: Left, a γ-ray shower image with primary energy $E_\gamma = 1$ TeV; middle, the much wider and irregular image from a proton shower with $E_p = 2.6$ TeV (Völk & Bernlöhr 2009). Right, description of a γ-ray event with the "Hillas parameters" (from Aharonian et al. 2006). Note the projected angle Θ (in this work: ϑ) between the nominal target position and the reconstructed γ-ray direction.

Angular source cuts. Secondly, the angular direction of the incoming shower can be used as a discriminating parameter, in particular when stereoscopic images are recorded. For example, if the observational target is point-like, a signal region of $\vartheta = 0.1°$ opening angle (solid angle $\Delta\Omega = 10^{-5}$ sr) is often used, corresponding to the 68% signal containment radius of the telescope's γ-ray point-spread-function.

Background estimation from off-source regions. Thirdly, the large field of view of modern IACT cameras (up to 5° in the case of H.E.S.S.) allows to simultaneously record off-target regions, where no or little γ-ray signal is expected. From these "off-regions" (see Figure 3.5), the remaining number of hadronic background events in the on-region, deceivingly reconstructed as γ-like, can be estimated.

A more precise description of data analysis techniques used for H.E.S.S. observations is presented in Section 3.3. Concluding the present section, it has to be remarked that the event selection techniques described above require sufficiently

well recorded shower images. The night sky background (NSB) of optical photons limits the detection of low-energy γ-ray events, as it produces a constantly fluctuation background of photoelectrons in the camera PMTs, visible also in Figure 3.3. This background is cut out by "image cleaning" procedures before the shower image parameters are reconstructed[5], but low-energy γ-rays simply do not produce enough Cherenkov light to be reliably reconstructed. This effectively sets the energy threshold of IACTs to a few tens of GeV for large-mirror telescopes (MAGIC and H.E.S.S. II, see below), and about 100 GeV for the ∼12 m telescopes of H.E.S.S. and VERITAS.

In addition, the duty cycle of Cherenkov telescopes is limited to about 10% by the requirements of low NSB and good weather conditions. Observations during moonlight, e.g., are possible, but come at the cost of a raised energy threshold (see e.g. Albert *et al.* 2008).

3.2 The High Energy Stereoscopic System (H.E.S.S.)

As of 2014, the *High Energy Stereoscopic System*[6] is an array of five imaging air Cherenkov telescopes, four identical ones placed in a square of 120 m side length and a large fifth telescope placed in the middle (Figure 3.4). The fifth telescope was inaugurated in 2012 and completes the "H.E.S.S. II" setup[7], the large dish size of about 28 m serving to lower the energy threshold of the system to below 100 GeV. However, the data used in the present work were collected with the four-telescope setup, which was constructed in the years 2002–2003.

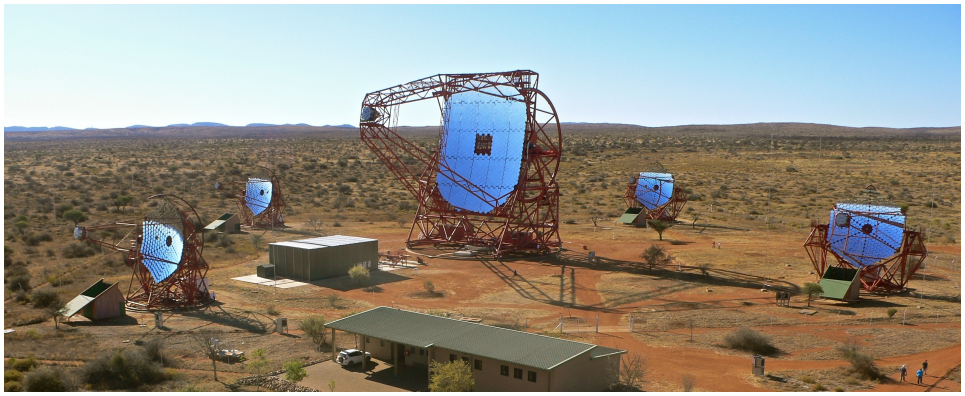

Figure 3.4: The H.E.S.S. array of Cherenkov telescopes.

H.E.S.S. is located at 23°16′18″ South, 16°30′00″ East in the Khomas Highland of Namibia, about 100 km southwest of Windhoek. The dry climate and elevation of 1800 m a.s.l. provide good observation conditions, and the location

[5] Except for the "model" analysis, see Section 3.3.3.

[6] www.mpi-hd.mpg.de/hfm/HESS/pages/about/

[7] www.mpi-hd.mpg.de/hfm/HESS/pages/press/2012/HESS_II_first_light/

on the southern hemisphere makes it possible to observe the central part of the Milky Way, resulting in the discovery of many Galactic VHE γ-ray sources (e.g. Aharonian *et al.* 2005).

The four smaller telescopes[8] have hexagonal reflector dishes of 13 m flat-to-flat diameter, the 382 mirror segments providing a total reflector size of 107 m^2 per telescope. 960 photomultiplier tubes per camera cover a field of view (FoV) that is 5° in diameter. Each PMT is equipped with a light-collecting Winston cone and thus corresponds to an angle of 0.16° on the sky.

More specifications of the four-telescope system and a detailed description of standard analysis procedures can be found in the publication by Aharonian *et al.* (2006). The observations of the Fornax galaxy cluster presented in Chapter 5 were analysed both using these procedures and the "model" analysis by de Naurois & Rolland (2009). Therefore, both analysis chains are summarized briefly in the next section[9].

3.3 H.E.S.S. data analysis

Generally speaking, IACT observations and data analysis are performed in the following steps:

- target tracking, camera and system event triggers and data acquisition;
- image processing and event reconstruction;
- background subtraction and estimation;
- analysis of γ-ray signal events, and possibly reconstruction of the differential energy spectrum and temporal or spatial structures in the signal.

Detailed description of all these steps and related issues like pointing and tracking accuracy, camera calibration, optical efficiency, estimation of systematic uncertainties etc. can be found elsewhere (Aharonian *et al.* 2006; de Naurois & Rolland 2009). Here, only a qualitative description is given.

Pointing, tracking and atmospheric monitoring. Observations with the H.E.S.S. telescopes are usually carried out in "wobble" mode (Fomin *et al.* 1994), i.e. with a pointing offset from the target position of typically 0.7°. This allows the simultaneous observation of background regions. During the observation runs of 28 min length, the atmospheric conditions are continually monitored. Variations in the atmosphere and the corresponding Cherenkov light yield from γ-ray events form the biggest source of systematic uncertainty in VHE observations. Therefore, runs with dubious atmospheric conditions, e.g. due to weather, dust or smoke from bushfires, are not used for analysis (see Hahn *et al.* 2014).

[8] Note the people in the lower right corner of Figure 3.4.

[9] Note that I performed the "standard" analysis based on Hillas parametrization of γ-ray images, while my collaborator Aion Viana made use of the "model" analysis.

Data acquisition. Such atmospheric variations are also visible in the system trigger rate, which is otherwise constant, due to the steady CR flux. The acquisition of air shower event data[10] is triggered by a set of conditions concerning single and multiple PMT pixel intensities, and in particular the simultaneous detection of an event in at least two telescopes. This ensures stereoscopic imaging, which is required for the event reconstruction, and suppresses the background from muon events triggering single telescopes. A typical system trigger rate is about 240 Hz.

Image cleaning and event reconstruction. In the standard H.E.S.S. analysis (Aharonian *et al.* 2006), recorded shower images are subjected to a cleaning procedure in order to suppress the NSB and to smooth out shower brightness fluctuations. Pixels with intensities less than a few photoelectrons and without neighbouring pixel signals are removed from the event image. After that, the remaining shower images are well suited for fitting the Hillas parameters width, length, distance to the camera centre and direction (Figure 3.3, right panel). The combination of Monte Carlo simulations and several separate camera images allows the calculation of *mean reduced scaled parameters*: The expected width and length of a shower ellipse are taken from MC-simulated lookup tables, depending on the impact parameter and image amplitude of the shower. These scaled parameters are then averaged over the telescopes which have recorded the event. The distributions of the mean reduced scaled width (MRSW) for simulated γ-ray and proton showers are shown in Figure 3.5, right panel.

γ-ray event selection. Using these parametric descriptions of the shower image, the reconstructed shower direction ϑ and the image intensity, selection cuts are applied to the event sample to reduce the hadronic background. The "standard" cuts as defined by Aharonian *et al.* (2006), for example, require an image amplitude of at least 80 photoelectrons, a maximal distance of $\vartheta^2 = 0.0125$ squared degrees from the nominal source position, and a maximal MRSW of 0.9 for a shower event to be γ-like. There are also other sets of selection cuts: "Hard" cuts ensure a particularly clean γ-ray sample, which maximizes the sensitivity for weak sources, and "loose" cuts allow a low energy threshold for stronger sources with steeply falling energy spectra. After application of these selection cuts, the γ-ray detection efficiency ranges from a few percent (hard cuts, large zenith angle) to about 70% (loose cuts, small zenith angle).

Background estimation. The remaining hadronic background in the γ-like event sample can be estimated by using geometrically defined off-source regions, as shown in the left panel of Figure 3.5. *Reflected* background regions, at the same radial distance to the camera centre as the signal region, are used to suppress camera acceptance differences between *on*- and *off*-regions. This method minimizes the systematic error on the background estimation and is therefore used for the calculation of signal spectra and fluxes. On the other hand, *ring*-like background regions around each point in the FoV make it possible to construct a "skymap" of

[10] The present state of the H.E.S.S. data acquisition system is covered by Balzer *et al.* (2014). The data handling makes use of the ROOT system (Brun & Rademakers 1997, see `root.cern.ch`).

γ-like event rates or significances (see Figure 5.6) around the target position.

Typically, the angular extent of the *off*-regions is larger than the *on*-region, which is taken into account by a factor α when estimating the number of γ-ray signal events N_γ:

$$N_\gamma = N_{\mathrm{on}} - \alpha \times N_{\mathrm{off}} \,. \tag{3.2}$$

For pointlike sources, for example, it is possible to record about ten off-regions, resulting in a background normalization factor $\alpha \approx 0.1$. However, the α factor is not determined by this purely geometrical consideration alone, because it is also used to parametrize possibly remaining differences in the camera acceptance and system live-time between the signal and background regions.

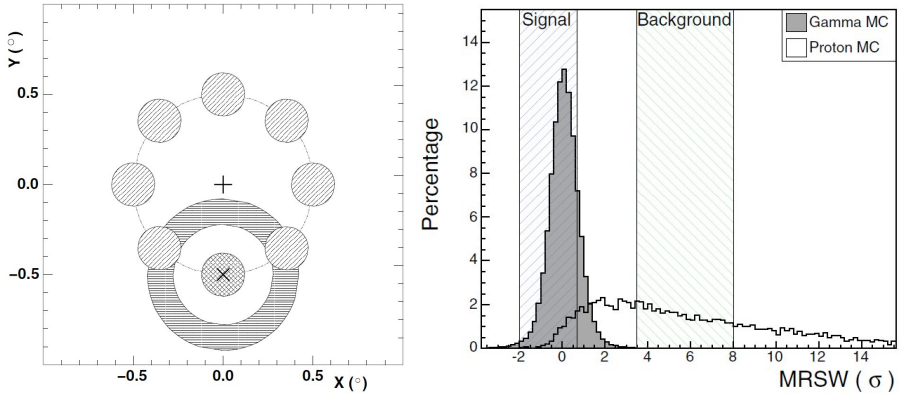

Figure 3.5: Background estimation techniques: Left, geometrical definitions of on- *vs* off-*regions (Aharonian* et al. *2006). The + sign marks the camera centre, the cross (×) marks the observational target, indicating a "wobble" distance of* 0.5°. *"Reflected" background regions, at the same radial distance to the camera centre, are filled with diagonal lines, while the "ring" background is filled with horizontal lines. Right panel: The* mean reduced scaled width *parameter (MRSW), in Monte Carlo-simulated distributions of photon and proton events. Such parameter regions are used in the "template" analysis (image from Berge* et al. *2007).*

3.3.1 Background estimation with the "template" method

Another method of background estimation, which is particularly useful for the generation of skymaps and the analysis of *extended* sources, was introduced by Rowell (2003). Here, the background contamination of the γ-like event sample is not estimated from designated off-regions in geometrical observation space, but in the space of the Hillas parameters. As shown in the right panel of Figure 3.5, the mean reduced scaled width parameter allows the selection of a relatively clean γ-ray sample. On the other hand, higher values of MRSW (and other parameters) define an event sample that is almost purely hadronic. This region in parameter space then defines the number of "off events" N_{off}, which nevertheless originate in the angular "signal" region of the sky.

The background normalization parameter α is computed as the ratio of γ-like to hadron-like events as found in the remaining part of the field of view, corrected for (radial) acceptance differences between the two event samples. Thus, the number of γ-ray signal events is derived by Equation 3.2, just like in the case of geometrically defined off-regions. The background normalization factor in the template method can have similar values ($\alpha \sim 0.1$), depending on the exact choice of parameters. See also Berge *et al.* (2007) for a description of the acceptance differences and their correction.

This method involving a background "template" was used for the Fornax cluster analysis presented in Chapter 5, because the extended source regions employed there (up to $\vartheta_{\mathrm{max}} = 1.0°$) made a geometrical background subtraction impossible. The template method was shown by Rowell (2003) to be reliable, except for the reconstruction of energy spectra, which suffers from systematic, but not well known differences between the signal and background regions in parameter space[11]. In the Fornax dark matter search, however, the reconstruction of γ-ray energies was not necessary, because only integrated event numbers were used for higher-level analysis.

3.3.2 The effective γ-ray detection area

An important ingredient for dark matter-related γ-ray analyses is the effective detection area of an instrument (see Sections 4.2.2 and 5.3). In the case of Cherenkov telescopes, it is obtained by making MC simulations of γ-ray-initiated air showers and analyzing their detection rate when passed through a simulation of the telescopes and their response. Figure 3.6 (from Aharonian *et al.* 2006) shows the effective area of the four-telescope H.E.S.S. configuration for different zenith angles of observation.

Two effects are visible: At lower energies (below ~ 1 TeV), the effective area is largest for observations at small zenith angles (ZA). Absorption of the Cherenkov light in the atmosphere over the longer path lengths induced by larger ZA renders low-energy events undetectable. In contrast, higher-energy events have a larger collection area at larger ZA, simply due to the geometrical projection of the showers on a larger area on the ground.

Also shown in Figure 3.6 are "safe energy thresholds" for different ZA, as defined by Aharonian *et al.* (2006). This refers to the energy reconstruction of γ-ray events, which becomes strongly biased at the low-energy end of the acceptance: Low-energy γ-rays may trigger the telescopes and be recorded due to an upward fluctuation of their Cherenkov light yield, so that the event energy is reconstructed at too high a value. Similar events with downward-fluctuating light yields, on the other hand, may not be detected at all. Therefore, energy cuts are induced on the γ-ray sample whenever spectral information is supposed to be obtained, in order to ensure unbiased reconstruction of the γ-ray events. These

[11] See, however, Fernandes *et al.* (2012).

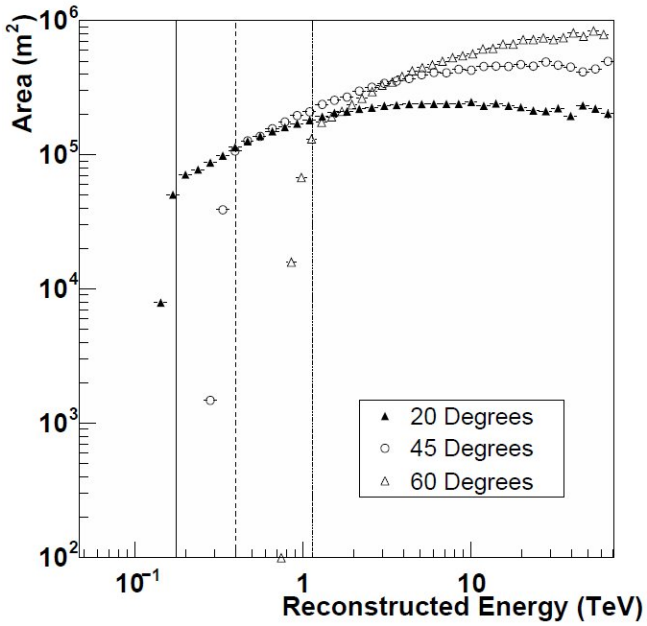

Figure 3.6: Effective detection areas of H.E.S.S. as a function of the reconstructed primary γ-ray energy for different zenith angles of observation (Aharonian et al. 2006). Vertical lines show the "safe energy threshold" (at higher energies for higher zenith angles), as defined in this publication.

thresholds can be defined as a function of the energy bias (Aharonian *et al.* 2006), by the event rate peak assuming a certain power-law spectrum (Konopelko *et al.* 1999), or by some percentage of the maximal effective area (Section 5.2).

Another consequence of this energy reconstruction bias is that the effective detection area differs when derived as a function of either the true γ-ray energy (in MC simulations) or the reconstructed energy. This has to be taken into account when obtaining energy spectra, but also for dark matter searches where the product of γ-ray spectrum and effective area is integrated (Section 4.2.2 and Equations 4.6, 4.13, 5.10 and 5.11).

3.3.3 The "model" analysis

The classic Cherenkov telescope analysis technique described above, relying on the Hillas parametrization of shower images, is robust, relatively simple and still widely in use today. However, a powerful alternative was introduced for the French telescope CAT (Bohec *et al.* 1998), which relies on a semi-analytic *model* of the Cherenkov light from γ-ray showers and a likelihood-based comparison of the raw camera images with the expectations from this model. The present implementation of this technique for the analysis of H.E.S.S. data was described by de Naurois & Rolland (2009).

In contrast to Hillas-based analyses, the "model" technique does not require

the cleaning of camera images and the corresponding loss of information about the shower. Instead, a statistical model for the night sky background is combined with a multi-dimensional model of the Cherenkov light emission, implementing e.g. also the primary γ-ray's point of first interaction in the atmosphere. The large parameter space of the shower model has to be sufficiently covered in Monte Carlo studies, and the multi-dimensional likelihood function used for fitting the model to the shower image is computationally expensive. On the other hand, this analysis technique provides a better sensitivity than the standard Hillas analysis. Therefore, it has been used extensively within the H.E.S.S. collaboration, particularly for observations of weak sources.

In the case of dark matter searches, however, no significant γ-ray excesses were found with the "model" technique, either. For example, both Hillas- and model-based analyses found a null result in the Fornax cluster data, see Section 5.2.

Finally, it should be noted that several refinements or combinations of the described analysis methods have been proposed, e.g. by Ohm *et al.* (2009), Fiasson *et al.* (2010) and Becherini *et al.* (2011).

3.4 MAGIC and VERITAS

Apart from H.E.S.S., there are two other major IACT systems currently operating: MAGIC (Major Atmospheric Gamma-Ray Imaging Cherenkov Telescopes, Albert *et al.* 2008b) and VERITAS (Very Energetic Radiation Imaging Telescope Array System, Holder *et al.* 2006). Both are situated in the northern hemisphere: MAGIC was built at 2200 m above sea level on the Roque de los Muchachos on the Canary island of La Palma (28°45′43″ N, 17°53′24″ W), while the VERITAS telescopes surround the base camp of the Whipple observatory on Mount Hopkins, Arizona (31°40′30″ N, 110°57′8″ W), at about 1300 m elevation.

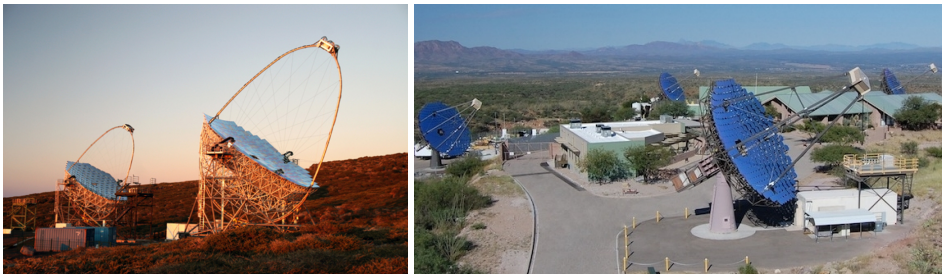

Figure 3.7: The MAGIC and VERITAS telescope systems. Sources: `mpg.de/593689/pressRelease20090415`, `veritas.sao.arizona.edu`

MAGIC was originally built as a single-dish telescope of 17 m mirror diameter in 2004. Later, a second telescope of the same dimension was added, at a distance of 85 m, to allow stereoscopic observations (Aleksić *et al.* 2012b). The large mirror size allows the MAGIC system to have a lower energy threshold than the other IACTs, see e.g. Aliu *et al.* (2008) and the effective detection areas shown in

Figure 4.2. The MAGIC observations which are used in Chapter 4 were made with the single telescope.

VERITAS, on the other hand, was planned as a multi-telescope from the beginning (Weekes *et al.* 2002). After design changes, a technical upgrade and the relocation of one of the telescopes (e.g. Perkins *et al.* 2009; Zitzer 2012), it now consists of four 12 m dish size telescopes in a close-to-rectangular array of about 100 m side length. Correspondingly, the instrumental sensitivity of VERITAS is similar to that of the H.E.S.S. array.

Results of dark matter searches with H.E.S.S., MAGIC and VERITAS and the corresponding references can be found in Section 4.2.

The future of IACT observations, beyond the upgraded H.E.S.S., MAGIC and VERITAS systems, will be determined by the "Cherenkov Telescope Array" (CTA). It is planned to consist of two sites, one in the northern and one in the southern hemisphere, each array having 50–100 telescopes of three different sizes. Acharya *et al.* (2013) introduce the concept, and Doro *et al.* (2013) discuss the prospects of dark matter searches with CTA. See also Section 6.2.

Chapter 4

Combined likelihood analysis of dark matter searches

The dwarf spheroidal galaxies (dSph) surrounding the Milky Way (McConnachie 2012; Walker 2013; Battaglia *et al.* 2013) are considered rewarding targets for dark matter searches with Cherenkov telescopes. In the framework of hierarchical structure formation (Section 2.1.2), they are understood to populate relatively small dark matter haloes that have formed early in the Universe. Correspondingly, these haloes feature high dark matter densities and concentrations (Section 2.1.3). In addition, the dSph galaxies typically show no recent star formation and supernova activity, and only small amounts of gas which could serve as target material for cosmic ray protons, so that there is very little "astrophysical" γ-ray production expected in these galaxies. Therefore, all three major IACT collaborations (see Chapter 3) have searched for DM annihilation signals from several different dwarf galaxies. A collection of target objects and references can be found in Table 4.1, see also Doro (2014).

Many of these searches suffer from the rather small amount of IACT observation time that can typically be dedicated to potential new sources. Therefore, a combination of the observations — often referred to as "source stacking"— seems a promising approach to enhance the sensitivity. Such combinations of dSph observations by the *Fermi*-LAT telescope have yielded the most stringent limits on the DM annihilation cross-section so far (Ackermann *et al.* 2011; Geringer-Sameth & Koushiappas 2011; Ackermann *et al.* 2014). In contrast to *Fermi*, a Cherenkov telescope cannot be used to observe *all* known dwarf galaxies, being located at either the northern or the southern hemisphere. The differences in the effective detection area and other observational parameters (like energy threshold or background rejection technique) between the IACTs is another obvious challenge in the combination of their data and the interpretation thereof.

Therefore, a new stacking technique is performed here, which is similar to what was introduced by Ackermann *et al.* (2011), and partly based on the work by Dickinson & Conrad (2013). It uses a combination of the *likelihood functions* of

the dSph dark matter searches, thus taking into account the different observational circumstances. In addition, the uncertainties on the DM halo profiles of the dwarf galaxies can be taken into account in a consistent and meaningful manner.

In principle, this "combined likelihood stacking" method can be used not only for dwarf spheroidal observations, but for all dark matter searches with Cherenkov telescopes. As an example, the H.E.S.S. result on the Fornax galaxy cluster is included in the following analysis.

4.1 The likelihood stacking technique

4.1.1 The likelihood function and its use

The *likelihood function* or simply "likelihood" is a common concept in statistical analyses (e.g. James 2006; Beringer *et al.* 2012), being a means of comparing observational or experimental *data* with the parameters of a theoretical *model*. Typically, one considers the observable parameter (set) x, depending on the model parameter(s) μ by a probability distribution function $p(x|\mu)$ that is assumed to be known *a priori*. Then, having measured the data x_d, the *likelihood* $\mathscr{L}$ of the model parameter μ, given the data, is defined as the *probability* (density) to observe x_d, given μ. For example, considering the Poissonian probability mass function

$$P(x|\mu) = \frac{\mu^x}{x!} e^{-\mu} , \tag{4.1}$$

the likelihood function $\mathscr{L}(\mu)$ is precisely this Poissonian probability to observe the data x_d, calculated for the possible values of the model parameter μ:

$$\mathscr{L}(\mu)\big|_{x_d} = P(x_d|\mu) . \tag{4.2}$$

A typical usage of the likelihood function is the estimation of the most probable model parameter value for a given set of data. This can be achieved by maximizing the likelihood or, correspondingly, by minimizing the function $-\ln\mathscr{L}$, which often simplifies the calculation.

Another useful feature of the likelihood function is its behaviour with respect to variations of the model parameters, which allows its use in the estimation of *confidence intervals* for a measured parameter, or upper or lower *limits* on the parameter value. The method used to perform this calculation is the *maximum likelihood ratio test*. Considering for simplicity the one-dimensional case of a likelihood that is a function of the data d and model parameters $\pi = (p, n)$, of which p is the single parameter of interest and n a set of *nuisance* parameters, the *profile likelihood function* is defined as

$$\mathscr{PL}(p') = \frac{\max\left(\mathscr{L}(p = p', n)\big|_d\right)}{\max\left(\mathscr{L}(\pi)\big|_d\right)} . \tag{4.3}$$

The maximization[1] in the denominator is performed over the complete range of π, while in the numerator, the maximization of $\mathscr{L}$ is performed over the subspace of π values defined by the parameter of interest having a particular value p'. Hence, one compares the maximal likelihood of the null hypothesis ($p = p'$) with that of the alternative hypothesis (p free), and the profile likelihood $\mathscr{PL}(p')$ expresses this comparison for the whole range of the parameter p'. Evidently, the values of $\mathscr{PL}$ lie between zero and one.

This definition of the profile likelihood has two consequences: First, it depends only on the parameter of interest, because the nuisance parameters are "automatically" taken into account in the calculation of $\mathscr{PL}(p')$. Second, since the two hypotheses are nested, Wilks' theorem (Wilks 1938) can be applied, which states that the values of $-2\ln\mathscr{PL}$ follow a $\chi^2(k)$ distribution, in the approximation of large samples and under some general assumptions. Protassov *et al.* (2002) summarize these *regularity conditions*, e.g. requiring that the null hypothesis parameter value p' must not lie on the boundary of the allowed parameter space.

In the χ^2 distribution, k is the number of degrees of freedom by which the nested hypothesis is reduced with respect to the other. Here, the parameter $p = p'$ is fixed, so that $k = 1$ in this case. Using Wilks' approximation, the function

$$\lambda(p') = -2\ln\mathscr{PL}(p')\,, \tag{4.4}$$

whose minimum is zero by construction, can be used to estimate confidence intervals or limits[2]. To this end, the value of λ is compared to the properties of the cumulative χ^2 distribution: For example, the p' values which result in a value of $\lambda(p') = 1\,(4)$ correspond to an 68.3% (95.5%) two-sided confidence interval for the estimated parameter.

The defining property of confidence intervals in the Frequentist sense is to have proper *coverage* (see Cousins 1995). This means that the intervals must be constructed such that they actually contain the true parameter value at the fraction of repeated experiments (possibly determined by simulations) that corresponds to the stated confidence level. Rolke *et al.* (2005) have shown that the coverage of confidence intervals derived with the profile likelihood method is quite good even for small event numbers ($N \sim 6$) and non-Gaussian distributions, when the large sample approximation is no longer valid. Cowan *et al.* (2011) describe slightly modified test statistics, also based on the maximum likelihood ratio, which also have good asymptotic behaviour even for event numbers smaller than ten. Finally, the *Fermi*-LAT collaboration has performed extensive coverage tests for their combined likelihood dark matter analysis (Ackermann *et al.* 2011), so that one may be reasonably confident that the method presented here also fulfills this criterion.

[1] More generally, the *supremum* rather than the maximum of the likelihoods should be considered, but this distinction is neglected here for the sake of simplicity.

[2] Note that the notation here is different from that of other authors, e.g. James (2006), where λ denotes the likelihood ratio 4.3.

4.1.2 The likelihood function of IACT dark matter searches

Considering Cherenkov telescope observations, where γ-ray events are counted in "on"- and "off"-regions in either coordinate or parameter space (cf. Chapter 3), the likelihood function can be defined as the product of the two corresponding Poissonian distributions. For a particular measurement yielding the event numbers $N_{\rm on}$ and $N_{\rm off}$, it is then expressed in terms of the two parameters s and b denoting the expectation value of *signal* and *background* events:

$$\mathscr{L}(s,b)\big|_{N_{\rm on},N_{\rm off}} = P(N_{\rm on}|s+\alpha b)\times P(N_{\rm off}|b)\,, \tag{4.5}$$

where α is the normalization factor between on- and off-region. (Typically, the off-region is larger, and hence $\alpha < 1$.)

In the particular case of dark matter searches, a model prediction for the parameter s can be given once a model of particle DM is chosen and the DM distribution of the object under consideration is known, cf. Section 2.3.1. Explicitly,

$$s\left(\langle\sigma v\rangle, m_\chi, J\right) = \frac{\langle\sigma v\rangle}{8\pi m_\chi^2}\times T_{\rm obs}\times J\times\int^{m_\chi}\mathrm{d}E\,A_{\rm eff}(E)\,\frac{\mathrm{d}N}{\mathrm{d}E}(E)\,. \tag{4.6}$$

The expected signal s depends on the dark matter properties $\langle\sigma v\rangle$ and m_χ, which are taken as "free" parameters here, and the γ-ray spectrum $\mathrm{d}N/\mathrm{d}E$ resulting from DM annihilations, which is fixed by the dark matter model. The signal also depends on the effective collection area $A_{\rm eff}(E)$ of the telescope during the observation time $T_{\rm obs}$ (cf. Chapter 3), and the halo factor J, which depends on the observational target (Section 2.3.1). Please note that following Ackermann *et al.* (2011) and Charbonnier *et al.* (2011), the halo factor is defined as

$$J(\Delta\Omega) = \int\mathrm{d}\Omega\int\mathrm{d}\ell\;\rho^2_{\rm DM} = \bar{J}(\Delta\Omega)\times\Delta\Omega \tag{4.7}$$

in the present chapter and in Appendix B.

All these parameters have to be included in the calculation of the likelihood function. The background expectation b is also a parameter of the likelihood, but it can be estimated from the data. In the likelihood analysis, it is treated as a nuisance parameter.

In addition to the Poissonian count statistics, the uncertainty on the halo factor can be incorporated in the likelihood function. Several authors (Walker *et al.* 2011; Charbonnier *et al.* 2011; Martinez *et al.* 2009; Ackermann *et al.* 2011) have determined how this uncertainty results from the analysis of dSph observations. In such analyses, the J factors are derived from the radial profiles of the stellar velocity dispersion around dwarf spheroidal galaxies (see Section 2.1.4). Using Monte Carlo simulations of stellar velocity distributions in dark matter haloes, and Bayesian analyses of the simulated and observational data, these authors find that the posterior distributions of J values derived for dwarf spheroidals

are approximately log-normal. Perhaps somewhat surprisingly, these J factor distributions do not depend strongly on the inner slope γ of the dark matter density profile (cf. Section 2.1.3). In fact, Charbonnier *et al.* (2011) could place tighter constraints on the J factors than on the halo parameters, as different combinations of scale radius and scale density would yield the same J factor.

Following these analyses, the probability density function for the true value of J, given the median value J_m and variance σ_J^2 of the posterior, is given by:

$$f_{\mathrm{PDF}}(J) = \frac{1}{\ln(10)\, J \sigma_J \sqrt{2\pi}} \exp\left\{ -0.5 \frac{\left[\log(J) - \log(J_m)\right]^2}{\sigma_J^2} \right\} \tag{4.8}$$

Here and in the remainder of this chapter, "log" always denotes the logarithm to base ten, as opposed to the natural logarithm "ln", and $\log J$ is to be understood as the logarithm of the *numerical value* of J, i.e. $\log\left(J / \mathrm{GeV^2 cm^{-5}}\right)$. The uncertainty σ_J has the same dimension as $\log J$ and is therefore unitless. See Appendix B for a brief discussion of how the mean, mode, and median values of a log-normal distribution relate to the central value of the corresponding normal distribution.

Since the prior distributions of the J values are approximately flat (see Appendix A), the same expression $f_{\mathrm{PDF}}(J)$ can be used as the likelihood function of the parameter J, given the "data" J_m and σ_J. Thus, the full likelihood function of a dark matter search result is defined as the likelihood given a certain value of the signal expectation s (depending on J), times the likelihood of this particular J value to be realized:

$$\begin{aligned} &\mathscr{L}\left(\langle\sigma v\rangle, m_\chi, J, b\right)\big|_{N_{\mathrm{on}}, N_{\mathrm{off}}, \alpha, J_m, \sigma_J} = \\ &\quad P\left(N_{\mathrm{on}} \,|\, s\left(\langle\sigma v\rangle, m_\chi, J\right) + \alpha b\right) \times P\left(N_{\mathrm{off}} | b\right) \times f_{\mathrm{PDF}}(J)\big|_{J_m, \sigma_J} . \end{aligned} \tag{4.9}$$

4.1.3 The combination of likelihood functions

The likelihood of a dark matter search result (Equation 4.9) is a function of both dark matter-related and observation-related parameters. Therefore, combining the likelihood functions of several observations is a useful method to gain additional insight about the universal dark matter properties, while keeping track of the observational circumstances of each singular result. Generally, the combination of several likelihoods is simply their product:

$$\mathscr{L}_{\mathrm{combined}} = \mathscr{CL} = \prod \mathscr{L}_i \,. \tag{4.10}$$

In the case of dark matter searches, the DM parameters $\langle\sigma v\rangle$, m_χ and $\mathrm{d}N/\mathrm{d}E$ can be assumed to be the same for all observations, while the observational parameters and J factors differ. Hence, for a set of M observations,

$$\mathscr{CL}\left(\langle\sigma v\rangle, m_\chi, \{J, b\}\right)\big|_{\{D\}} = \prod_{i=1}^{M} \mathscr{L}_i\left(\langle\sigma v\rangle, m_\chi, J_i, b_i\right)\big|_{D_i} , \tag{4.11}$$

where $\{J, b\}$ and $\{D\}$ denote the complete *sets* of nuisance parameters, i.e. the J values and background parameters, and observational data $D_i = \left(N_{\mathrm{on},i}, N_{\mathrm{off},i}\right)$, respectively. The annihilation spectrum $\mathrm{d}N/\mathrm{d}E$ is considered fixed and therefore no longer explicitly included here. The observational parameters α_i, $T_{\mathrm{obs},i}$ and $A_{\mathrm{eff},i}$ are implicit ingredients of the calculation as well.

Using this combined likelihood, the profile likelihood for the parameter $\langle\sigma v\rangle'$ can be constructed as

$$\mathscr{PL}(\langle\sigma v\rangle') = \frac{\max\left(\mathscr{CL}(\langle\sigma v\rangle = \langle\sigma v\rangle')\right)}{\max\left(\mathscr{CL}\right)}\,, \tag{4.12}$$

while keeping the dark matter mass m_χ fixed, in order to derive bounds on the value of the annihilation cross-section. The nuisance parameters J_i and b_i are taken into account by the maximization procedure.

It should be noted at this point that Dickinson & Conrad (2013) have performed a thorough investigation of the statistical properties of a similar combined likelihood analysis. Instead of the dark matter parameters $\langle\sigma v\rangle$ and m_χ, they concentrated on the estimation of the signal and background parameters s and b. Also, rather than being influenced by the J factor uncertainties, their likelihood function incorporated systematic uncertainties on the background normalization factor α. Nonetheless, their treatment of these uncertainties as an additional term in the multiplicative likelihood was quite similar to what is performed here. Concerning the performance of the combined likelihood method, Dickinson & Conrad (2013) used numerical simulations to test the estimation of signal significances, the statistical power of the method and the coverage of derived confidence intervals. In all cases, the combined likelihood method performed at least as good as a traditional "data stacking" approach, and sometimes markedly better.

4.1.4 Computational implementation

For the analysis presented in this chapter, all likelihood functions were calculated numerically. Since, e.g., the integration of the γ-ray spectrum over the effective area (Equation 4.6) had to be performed for each considered dark matter particle mass, it turned out too costly to compute the likelihood anew for each iteration in the maximization process. Therefore, the calculations were executed for a grid of fifty times fifty values in the parameters m_χ and $\langle\sigma v\rangle$, distributed logarithmically from 100 GeV to 100 TeV and 10^{-26} to 10^{-17} $\mathrm{cm}^3\mathrm{s}^{-1}$, respectively. The profile likelihoods were then interpolated linearly between the grid points for the maximizations of the likelihood and the computation of the upper limits.

All calculations were performed using the Python programming language[3], its SciPy (Jones *et al.* 2001) and NumPy (Oliphant 2007) extensions[4] and the IPython

[3] python.org
[4] scipy.org, numpy.org

interface[5] (Pérez & Granger 2007). The results were visualized with Matplotlib[6] (Hunter 2007).

4.2 Observational parameters and data

In order to perform a likelihood analysis as described in the previous section, published results of dark matter searches with Cherenkov telescopes were utilized. Table 4.1 summarizes these observations and their results in terms of the event numbers, the α factor, the resulting number of excess events $N_{\text{excess}} = N_{\text{on}} - \alpha \times N_{\text{off}}$, and the observation time. In addition to DM searches concerning dwarf spheroidal galaxies, the H.E.S.S. result on the Fornax galaxy cluster (see Chapter 5 and Abramowski *et al.* 2012, 2014) was considered for comparison.

Target	Telescope	N_{on}	N_{off}	α	N_{excess}	T_{obs} (sec)	Ref.
Sculptor	H.E.S.S.	117	2283	0.04	25.7	42480	[1]
Carina	H.E.S.S.	86	1858	0.05	-6.9	53280	[1]
Sagittarius	H.E.S.S.	437	4270	0.10	14.2	39600	[2]
Segue 1	MAGIC	52978	53301	1.0	-323.0	105912	[3]
	VERITAS	1082	12479	0.08	33.8	172080	[4]
Draco	MAGIC	10883	10996	1.0	-113.0	28080	[5]
	VERITAS	305	3667	0.09	-28.4	66185	[6]
Ursa Minor	VERITAS	250	3084	0.09	-30.4	68080	[6]
Fornax	H.E.S.S.	160	122	1.0	38.0	52200	[7]

Table 4.1: Observational results used in the combined likelihood analysis: Shown are the targets of observation, the telescope, the γ-ray event numbers, the on-off-ratio α (cf. Chapter 3), the resulting number of excess events, the observation time T_{obs} and the corresponding publication. Note that for the MAGIC observations and that of the Fornax cluster, $\alpha = 1$ by definition. The references are: [1] Abramowski et al. (2011a); [2] Aharonian et al. (2008, 2010); [3] Aleksić et al. (2011); [4] Aliu et al. (2012); [5] Albert et al. (2008a); [6] Acciari et al. (2010); [7] Abramowski et al. (2012, 2014).

4.2.1 J distributions

The dark matter halo factors for the different dwarf galaxies were also taken from published analyses, summarized in Table 4.2. All J values were derived for signal integration angles $\vartheta_{\text{max}} = 0.1°$.

Charbonnier *et al.* (2011) and Essig *et al.* (2010) stated uncertainties to their most probable values. For the other two targets, Sagittarius dSph and the Fornax cluster, a factor of two uncertainty (at 1σ) was assumed. Viana *et al.* (2012) state that this is the spread of J values they find under the assumption of NFW halo

[5] ipython.org
[6] matplotlib.org

profiles for Sagittarius. In the case of Fornax, this factor is chosen (somewhat arbitrarily) to reflect the results of different analyses cited in the publication and in Chapter 5. While Ackermann *et al.* (2011) reported symmetrical uncertainties for their dwarf halo analyses, Charbonnier *et al.* (2011) have found asymmetrical intervals in some cases. For the analysis presented here, the σ_J value corresponding to a *downward* fluctuation of J was used, assuming that this is the more important case for the calculation of *limits* on dark matter signals. However, possible *larger* values of J are thus artificially suppressed.

The observations of the two dwarf spheroidals Willman 1 (Acciari *et al.* 2010; Aliu *et al.* 2009) and Boötes 1 (Acciari *et al.* 2010) were not utilized. The irregular kinematic properties of Willman 1 (Willman *et al.* 2011) prevent the derivation of its DM halo properties in the usual way of using the Jeans equations, which depends on thermal equilibrium and spherical symmetry (see Section 2.1.4, Walker (2013) or Battaglia *et al.* 2013). Similarly, the elongation of Boötes 1 does not allow for spherical modelling, which lets Acciari *et al.* (2010) refrain from publishing the halo parameter uncertainties, only stating that they are "large". Therefore, these objects were not included in the likelihood analysis presented here.

Possible γ-ray flux enhancements due to dark matter substructures in the dwarf spheroidals are expected to be much smaller than in the case of galaxy clusters (Chapter 5), probably yielding a factor of less than ten (see e.g. Kuhlen *et al.* (2008), Pieri *et al.* (2009), Sánchez-Conde *et al.* (2011) and the references therein). Therefore, they are not considered in the analysis presented here.

Figure 4.1 shows the probability distributions of the J factors as summarized in Table 4.2. The *median* value J_m of the distributions is additionally indicated, corresponding to the maximum of the Gaussian distribution of $\log J$.

Target	$\log\left(J_m / \mathrm{GeV^2 cm^{-5}}\right)$	σ_J	Reference
Sculptor	17.9	0.2	Charbonnier *et al.* (2011)
Carina	17.1	0.1	Charbonnier *et al.* (2011)
Sagittarius	17.3	0.3	Viana *et al.* (2012)
Segue 1	19.0	0.6	Essig *et al.* (2010)
Draco	17.8	0.2	Charbonnier *et al.* (2011)
Ursa Minor	18.3	0.3	Charbonnier *et al.* (2011)
Fornax	17.4	0.3	Abramowski *et al.* (2012, 2014)

Table 4.2: Summary of the J distributions used in the likelihood analysis. All values were derived for signal integration angles $\vartheta_{\max} = 0.1°$. The second row shows the logarithm of the median J_m of the log-normal distributions, the third row shows their uncertainties σ_J. Note that for Segue 1, Essig et al. (2010) quote J values derived by Simon et al. (2011) and Martinez et al. (2011). The central value for Sagittarius is taken from Viana et al. (2012), assuming a factor of two for the uncertainty (see main text). The Fornax cluster is added for comparison: using model SR10, a10 with medium substructure boost (cf. Chapter 5 and Abramowski et al. 2012, 2014), and again an uncertainty of roughly a factor of two.

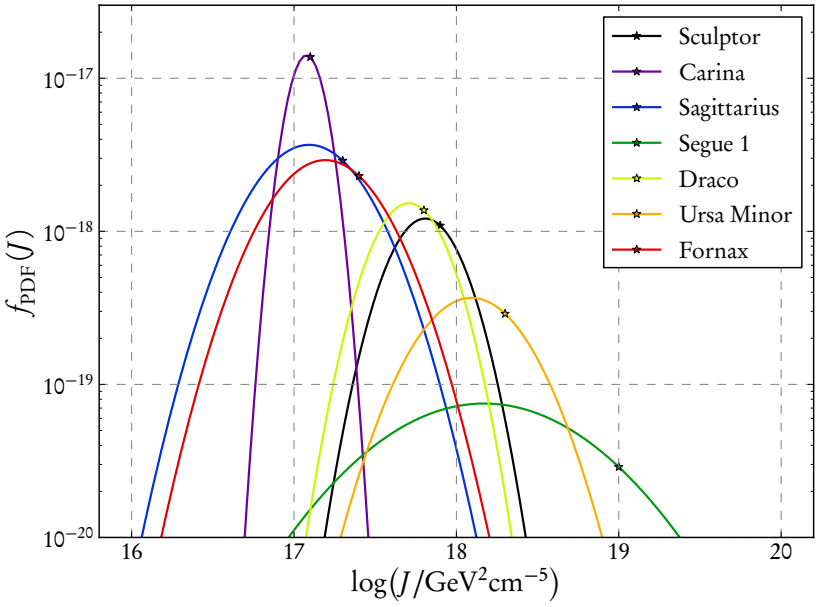

Figure 4.1: The log-normal probability distributions of the J factors as summarized in Table 4.2. The median values are indicated by a star.

4.2.2 Effective detection areas

Another ingredient for the calculation of the combined likelihood function 4.11 is the energy-dependent effective detection area A_{eff} of the Cherenkov telescopes (see Section 3.3). Unfortunately, it is not common in VHE γ-ray astronomy to publish these alongside the observational results, even though they depend on the zenith angle and event reconstruction technique, so that they may be different for each observation. Therefore, the best *available* information about the different effective areas was used, followed by a cross-check of the resulting limits against the published values (Section 4.3.1).

Since the effective area of a telescope is estimated using Monte Carlo simulations of air showers and the detector response, it can be expressed both as a function of the *true* energy E_{true} of the γ-ray event and of its *reconstructed* energy, E_{reco}. It appears reasonable to make use of the former, $A_{\mathrm{eff}}(E_{\mathrm{true}})$, as long as no energy cut is applied to the event sample. However, this information was not always available.

The H.E.S.S. collaboration published effective areas for different zenith angles in Aharonian *et al.* (2006b). The effective area for a zenith angle of 20 degrees was chosen for this analysis, since this value corresponds rather well to the respective average zenith angles of the H.E.S.S. observations (except Carina). Here, the curve labelled $A_{\mathrm{eff}}(E_{\mathrm{reco}})$ was used.

An effective area of the MAGIC-I telescope was published in a PhD thesis

(Gaug 2006). Since all dark matter searches considered here were performed with the single-telescope system and not the newer stereo system MAGIC-II (Cortina *et al.* 2009), this A_{eff} is a reasonable estimate of the state of the telescope during the published observations. However, as the analysis results were presented as γ-ray event numbers above certain energy thresholds, these thresholds were imposed in this work as well. Their values are $E_{\text{th}} = 100$ GeV for Segue 1 and 140 GeV for Draco.

Effective areas of the VERITAS telescope system were also published in a PhD thesis (Wood 2010). Here, different A_{eff}'s were shown for the observations of Draco, Segue 1 and Ursa Minor, so that the respective effective area could be used for the cross-check and the combined likelihood analysis. Figure 4.2 shows the effective areas that were collected for this study.

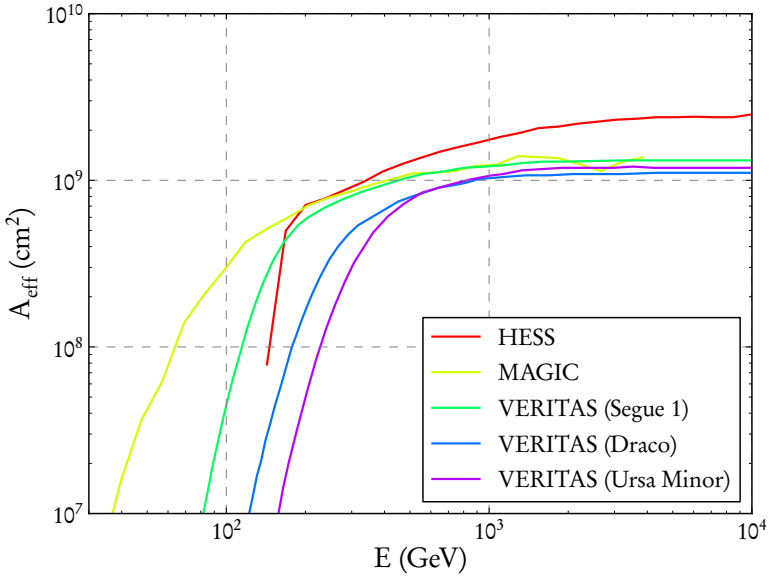

Figure 4.2: Effective collection areas of H.E.S.S. (Aharonian et al. 2006b), MAGIC (Gaug 2006) and VERITAS (Wood 2010). While those of H.E.S.S. and MAGIC were reported for rather generic cases, the effective areas of VERITAS correspond directly to the DM searches used in this analysis.

4.2.3 γ-ray spectra from DM annihilations

The final state particles of dark matter annihilation events, and hence the resulting γ-ray spectrum, depend on the specific DM particle that is realized in nature — or chosen for analysis. In supersymmetric DM models, for example, the branching fractions into quarks, leptons or vector bosons depend on the bino, wino or higgsino content of the neutralino, cf. Section 2.2.3. Therefore, in order to

be as model-independent as possible, it is worthwhile to analyse the combined likelihoods assuming several different final states. Three possibilities are considered here: Annihilation into $b\bar{b}$, W^+W^- and $\tau\bar{\tau}$ pairs, each with a branching fraction of 100%, and neglecting virtual internal bremsstrahlung in the WW case (Bringmann *et al.* 2008, see Section 5.3.2). The *real* dark matter particle may not annihilate to such pure final states, but the γ-ray spectrum from annihilations with non-unitary branching ratios would lie somewhere between these "extreme" cases.

For the combined likelihood, the γ-ray spectrum parametrizations of Cembranos *et al.* (2011) were utilized[7]. Another commonly used parametrization is the one provided by Bergström *et al.* (1998) for the case of annihilations to W/Z bosons. Figure 4.3 shows the corresponding γ-ray spectra for a dark matter particle mass of 1 TeV.

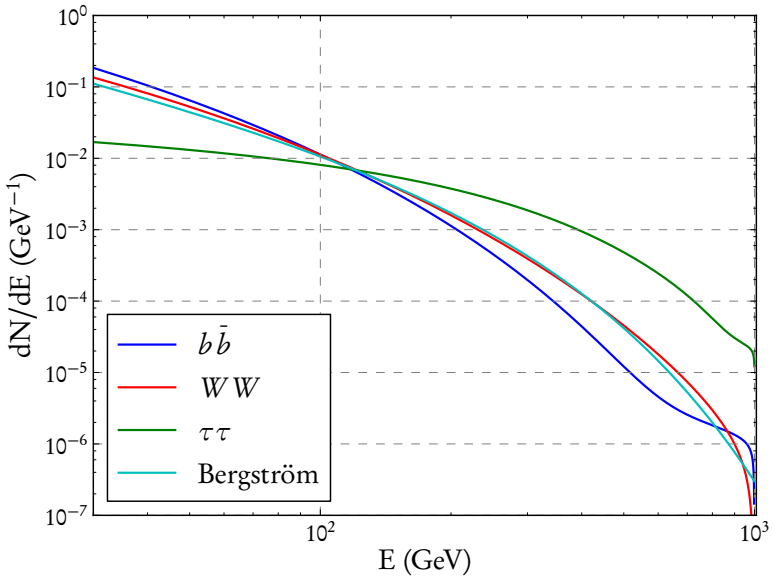

Figure 4.3: γ-ray spectra from dark matter annihilations into $b\bar{b}$, W^+W^- and $\tau\bar{\tau}$ pairs, for a dark matter particle of mass $m_\chi = 1$ TeV. Parametrizations are taken from Cembranos et al. (2011). In addition, the photon spectrum parametrization derived by Bergström et al. (1998) for annihilations to W/Z bosons is shown.

[7] In some cases, the parametrizations had to be slightly modified or amended, e.g. in the case of DM mass ranges for which Cembranos *et al.* (2011) provided a plot of the spectrum, but not the parameters. See also Cembranos *et al.* (2013) for an assessment of the uncertainties related to such γ-ray spectra.

4.3 Results

4.3.1 Cross-check with published data

In order to test the validity of the gathered information about the telescopes and observations, the attempt was made to reproduce the published results. In most of these dark matter searches (Table 4.1), constraints on the dark matter particle properties were derived as upper limits on the total annihilation cross-section, assuming a certain final state of the annihilation (e.g., $b\overline{b}$ or W^+W^-) and the corresponding γ-ray spectrum, as a function of the DM particle mass m_χ. These limits are typically calculated using the following formula:

$$\langle\sigma v\rangle_{\mathrm{UL}} = \frac{8\pi}{T_{\mathrm{obs}}} \frac{m_\chi^2}{J(\Delta\Omega)\Delta\Omega} \frac{N_\gamma^{\mathrm{UL}}}{\int_{E_{\mathrm{th}}}^{m_\chi} \mathrm{d}E_\gamma A_{\mathrm{eff}}\left(E_\gamma\right) \frac{\mathrm{d}N_\gamma\left(E_\gamma\right)}{\mathrm{d}E_\gamma}}\,, \tag{4.13}$$

where $E_{\mathrm{th}} = 0$ is assumed in many, but not all cases, implying that all γ-ray events are counted without imposing an energy threshold E_{th}.

A somewhat exceptional example is the MAGIC publication on Draco (Albert *et al.* 2008a), in which the derived γ-ray limits were compared directly to particular supersymmetric DM models and their respective γ-ray yields. For all other observations, the results calculated using the effective areas described in Section 4.2.2 could be compared with the published "$\langle\sigma v\rangle$ over m_χ" figures. In order to achieve good agreement, some of the utilized effective areas had to be adjusted. This was achieved by cutting off the effective area at a threshold energy, especially when the zenith angle of the observation was higher, e.g. in the case of Carina. In these cases, the energy threshold cited for the derivation of γ-ray flux limits in the publications was used, see Table 4.3.

A somewhat peculiar aspect of the published results is that the upper limit on the number of γ-ray events, N_γ^{UL}, is calculated using different methodologies. While in the H.E.S.S. publications, the method of Feldman & Cousins (1998) is cited even though it depends on *exact* knowledge of the expected background, the MAGIC and VERITAS papers cite "the" Rolke method (Rolke *et al.* 2005) without specifying the details, e.g. which background distribution or detection efficiency was assumed[8].

Nevertheless, the published values of N_γ^{UL} were used for the cross-checks shown below, together with the J factors that were assumed in the original publications. Table 4.3 summarizes the specific parameters of the analyses considered for the cross-check and Figure 4.4 shows the results. Column six of this table presents the final state of the dark matter annihilation, which determines the γ-ray

[8] As a side note, it may be noted that the value of N_γ^{UL} reported by Aliu *et al.* (2012) seems to be calculated in a different way than the ones quoted by Acciari *et al.* (2010) for the other dwarfs, given the published values of N_{on}, N_{off} and α.

spectrum and hence influences the limits. In all H.E.S.S. publications, limits were derived using (among others) the Bergström *et al.* (1998) parametrization of a photon spectrum from annihilation into W/Z bosons. The same spectrum was used here. The Segue 1 publication by VERITAS showed results for annihilations into both $b\overline{b}$ and $\tau\overline{\tau}$ pairs, so that both spectra could be used for comparison. The MAGIC collaboration also published Segue 1 limits for $b\overline{b}$ and $\tau\overline{\tau}$ spectra, but the $\tau\overline{\tau}$ results were calculated using a sophisticated method of determining the ideal energy threshold which could not be reproduced here. Hence, only the $b\overline{b}$ limits were included in the cross-check. For the $b\overline{b}$ and $\tau\overline{\tau}$ final state cross-checks, the photon spectrum parametrizations of Cembranos *et al.* (2011) were used, which may be different from the ones used in the publications, cf. Cembranos *et al.* (2013). Nevertheless, reasonable agreement was found for all compared published limits.

Target	Telescope	N_γ^{UL}	E_{th} (GeV)	J $\left(10^{17}\,\mathrm{GeV^2cm^{-5}}\right)$	Final state
Sculptor	H.E.S.S.	32.4	220	2.5	W/Z
Carina	H.E.S.S.	8.6	320	4.0	W/Z
Sagittarius	H.E.S.S.	56.0	—	398.0	W/Z
Segue 1	VERITAS	135.9	—	126.0	$b\overline{b}$
	VERITAS	135.9	—	126.0	$\tau\overline{\tau}$
	MAGIC	453.0	100	79.4	$b\overline{b}$
Draco	VERITAS	18.8	—	15.8	$\tau\overline{\tau}$
Ursa Minor	VERITAS	15.6	—	25.1	$\tau\overline{\tau}$
Fornax	H.E.S.S.	71.0	260	1.6	W/Z

Table 4.3: Cross-check parameters. Columns 3–5 show the upper limit on the number of γ-ray events, the energy threshold (where applied, cf. main text) and the J factor as they were stated in the original publication. The references can be found in Table 4.1. Column six shows the final state particles of dark matter self-annihilations, determining the γ-ray spectrum.

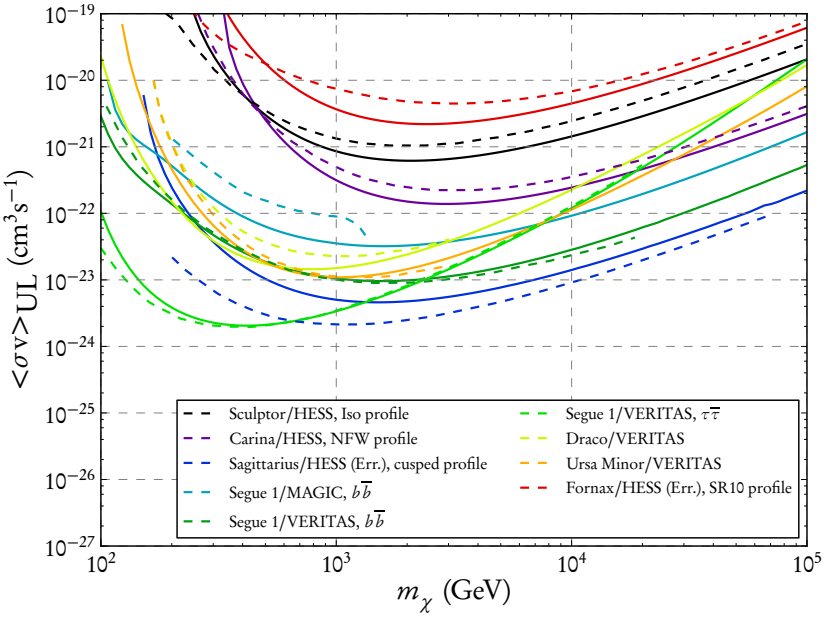

Figure 4.4: Cross-check results. The solid lines show the upper limit on the annihilation cross-section $\langle\sigma v\rangle$ as they could be derived in this work, while the dashed lines reproduce the published limits. References can be found in Table 4.1. Specific parameters of the published results, such as particular halo profiles or annihilation final states, are shown in the legend.

4.3.2 Single-observation likelihood limits

After the cross-checks had proven successful, the likelihood function of each single observation was calculated, using the respective J factor *distribution*, in order to derive limits on the annihilation cross-section. These "single likelihood limits" could then be compared to the "standard" limits, calculated with Equation 4.13, but with the J values fixed to the *mode* (see Appendix B) of their probability distributions.

Hence, both the validity of the likelihood method and the effect of including the J uncertainties could be tested. In addition, although it may appear counterintuitive to lay much weight on the single-object likelihoods when the main goal is the *combination* of the likelihood functions, it turns out that the combined likelihood can be derived from the single ones in a relatively simple way, see Section 4.3.3.

Profile likelihoods

As explained in Section 4.1.1, the result of maximising and normalising the likelihood function is the profile likelihood $\mathscr{PL}$, which depends on the dark matter mass and annihilation cross-section as the only remaining free parameters. The

logarithmic profile likelihood function

$$\lambda\left(\langle\sigma v\rangle, m_\chi\right) = -2\ln\mathscr{PL}\left(\langle\sigma v\rangle, m_\chi\right) \tag{4.14}$$

can be used to derive limits on the annihilation cross-section $\langle\sigma v\rangle$ for a particular dark matter mass m_χ. This "log-likelihood" often follows an approximately parabolic shape, at least around its minimum. However, as long as there is no indication for a γ-ray signal from dark matter annihilations, no *lower* bound on the parameter $\langle\sigma v\rangle$ can be expected, except for the physical boundary $\langle\sigma v\rangle \geq 0$. Correspondingly, the λ functions may not be symmetrical parabolae, but rather flat in the direction of smaller cross-sections. Therefore, only *upper* limits on $\langle\sigma v\rangle$ are derived here, by finding the cross-sections $\langle\sigma v\rangle_{\mathrm{UL}}$ where the log-likelihood has the value

$$\lambda\left(\langle\sigma v\rangle_{\mathrm{UL}}\right) = 2.706\,, \tag{4.15}$$

which corresponds to a one-sided limit at 95% confidence level (C.L.). It must be stressed that in the computation of λ, the cross-sections are being compared against their *maximum likelihood* values (which correspond to $\lambda = 0$), but *not* against $\langle\sigma v\rangle = 0$. Doing so would violate the regularity conditions of the maximum likelihood ratio test, as explained by Protassov *et al.* (2002).

Figure 4.5 shows the log-likelihood functions $\lambda(\langle\sigma v\rangle)$ for all individual observations, assuming annihilations into $b\overline{b}$ pairs, as a function of the cross-section parameter $\langle\sigma v\rangle$. Each line shows the likelihood for one particular DM particle mass, with lighter colours corresponding to lighter masses. For the cross-section limits, fifty different mass values were considered, distributed in equal logarithmic differences over the range 100 GeV – 100 TeV. For the sake of clarity, Figure 4.5 shows only every fourth mass value. As expected, the likelihoods flatten out towards lower annihilation cross-sections.

Some of the profile likelihoods show a distinct minimum at $\langle\sigma v\rangle$ values in the range from 10^{-22} to 10^{-18} cm^{3}s^{-1}. If significant, this would indicate the presence of a γ-ray signal, possibly dark matter-induced. However, $\lambda(\langle\sigma v\rangle)$ does not exceed a value of six for cross-sections that are *smaller* than at the minimum, corresponding to a significance of roughly 2.5σ (for a two-sided confidence interval), so that a γ-ray signal detection cannot be claimed[9].

Similarly, the profile likelihood functions for annihilations into W^+W^- and $\tau\overline{\tau}$ pairs were calculated. These are shown in Appendix C.

[9] In fact, the event numbers from the Sculptor observation by Abramowski *et al.* (2011a) also yield a significance of 2.5σ, when calculated with Equation 17 of Li & Ma (1983).

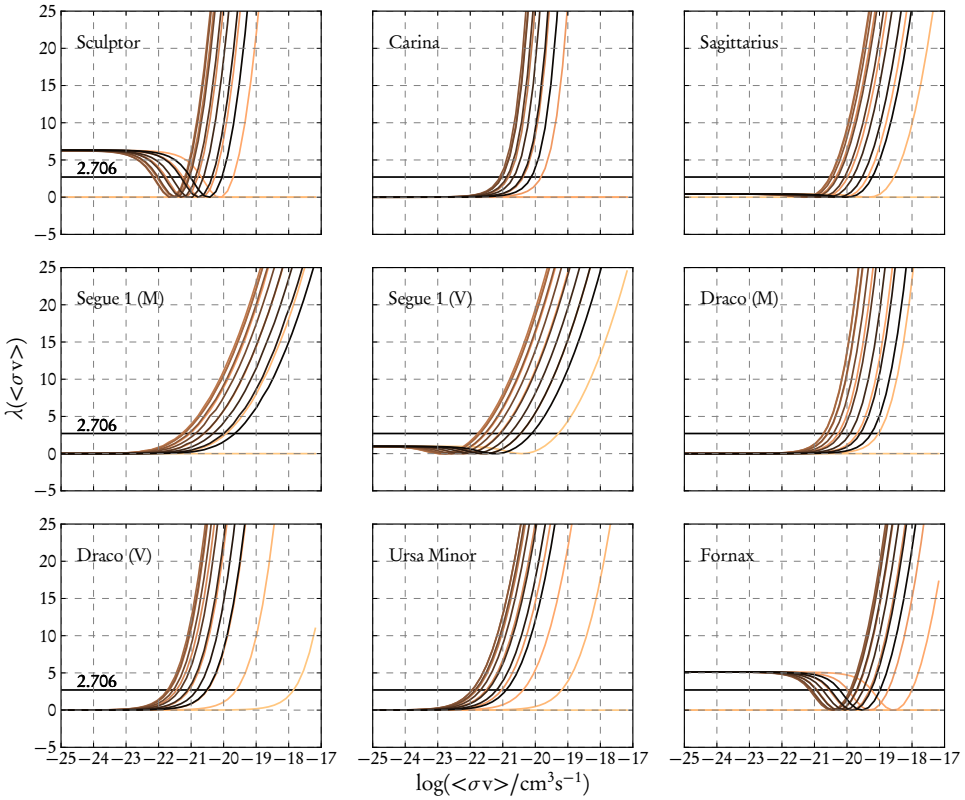

Figure 4.5: The logarithmic profile likelihood functions $\lambda(\langle\sigma v\rangle)$ of the different observations, calculated for DM annihilations to $b\bar{b}$ pairs. (M) and (V) indicate observations by MAGIC and VERITAS, respectively. Each curve corresponds to one particular dark matter mass m_χ in the range from 100 GeV to 100 TeV, with lighter colours indicating lighter masses. The intersections of the likelihoods with the lines drawn at $\lambda = 2.706$ indicate the 95% C.L. upper limits on the annihilation cross-section $\langle\sigma v\rangle_{\mathrm{UL}}$. (In the cases of Sculptor and Fornax, this applies to the respective intersections at higher *values of $\langle\sigma v\rangle$.)*

Comparison of single-observation limits

From the profile likelihoods shown in Figures 4.5, C.1 and C.2, upper limits $\langle\sigma v\rangle_{\mathrm{UL}}$ on the dark matter annihilation cross-section were calculated according to Equation 4.15 for each particular dark matter particle mass and for all different final states. Figure 4.6 shows the limits that were derived for $b\bar{b}$ annihilation in this way.

Additionally, "simple" limits are shown, which were calculated according to Equation 4.13. Here, the J factors are fixed to the *modes* of their respective distributions, corresponding to the maximum likelihood values of the log-normal distributions, if these were considered separately. The upper limits on the number of γ-ray events are those shown in Table 4.4. These were calculated using the "Rolke method" for Poissonian signal and background and known efficiency $\varepsilon = 1$,

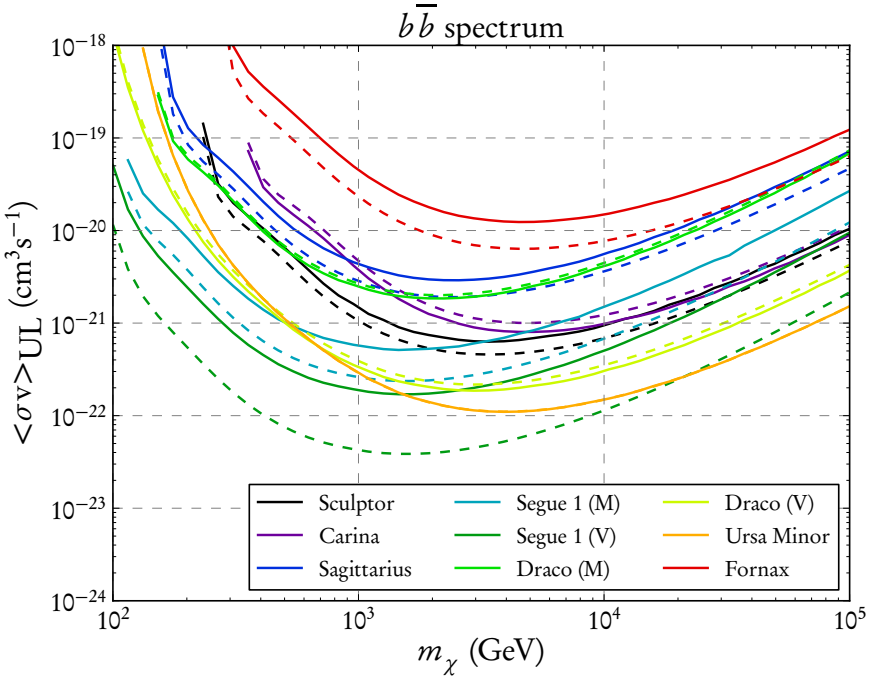

Figure 4.6: Comparison of single-observation limits. The solid lines show the upper limits on the self-annihilation cross-section $\langle \sigma v \rangle$, as a function of the dark matter particle mass m_χ, that were derived using the likelihood method. The dashed lines show the "simple" limits as explained in the main text. Colours indicate the different observations, with (M) *and* (V) *corresponding to measurements by MAGIC and VERITAS, respectively. (In the case of Ursa Minor, the dashed line lies on top of the solid one.)*

with the implementation provided by Lundberg *et al.* (2010).

It is visible that in most cases, the cross-section limits derived with the likelihood method are similar to the "simple" limits, but a little *weaker*. This reflects the uncertainty on the J parameters, as well as the fact that there is no longer a separately calculated limit on the number of γ-ray events. This is also the reason why in some cases where the J uncertainty is small, i.e. Carina, Draco and Ursa Minor, the likelihood limit is as good as or even better than the "standard" one. However, the standard method uses the 95% C.L. limit on N_γ together with the *maximum* likelihood value of J, rendering the resulting *coverage* of these limits somewhat dubious.

Observation	N_γ^{UL} (published)	N_γ^{UL} (Rolke)
Sculptor	32.5	48.5
Carina	8.6	14.3
Sagittarius	56.0	58.3
Segue 1 (M)	453.0	393.0
Segue 1 (V)	135.9	102.0
Draco (M)	231.0	198.2
Draco (V)	18.8	18.8
Ursa Minor	15.6	15.6
Fornax	71.0	71.2

Table 4.4: Results of re-calculating the upper limits on the number of γ-ray events. The right column shows the N_γ^{UL} values calculated using the "Rolke method" for Poissonian signal and background and known efficiency $\varepsilon = 1$, using the algorithm provided by Lundberg et al. (2010).

Maximum likelihood parameters

As explained before, the log-likelihood functions $\lambda_i(\langle\sigma v\rangle)$ are derived by maximizing the likelihoods with respect to the nuisance parameters J_i and b_i. It is instructive to consider the corresponding values of these parameters for a fixed mass, over the range of possible annihilation cross-sections. The upper panels of Figure 4.7 show the behaviour of the *maximizing* parameters $J_{c,i}$ and $b_{c,i}$ as a function of $\langle\sigma v\rangle$; the lower panels show the corresponding values of the log-likelihood functions.

It is visible (and intuitively clear) that for larger cross-sections, and hence larger expected signal, smaller values of J_c and the background estimate b_c are more likely. The left panels of Figure 4.7 show that in some cases where the number of excess events is positive, i.e. Sculptor, Fornax and Segue 1 (VERITAS), there is a peak in the plot of $\log J_c$ over $\log\langle\sigma v\rangle$ and a corresponding turnover in the $\lambda - J_c$ curve. This indicates that the profile likelihood method "finds" those particular values of J and $\langle\sigma v\rangle$ that correspond best to the positive γ-ray signal.

On the other hand, the right panels show that the relative deviations of the background estimation from the number of "off" events, b_c/N_{off}, remain very small for all cases except Fornax. There, $\alpha = 1$ and both N_{on} and N_{off} are rather small. Hence, the maximum likelihood is influenced more strongly by the event numbers than in the other cases, where the J factor variations have a stronger impact. It is important to remember that $\lambda(\langle\sigma v\rangle)$ is *not* a function that depends *directly* on the parameters J and b. Instead, e.g. the steep slopes in the $\lambda - b$ plane of panel d) only show that strong variations of the λ functions can be accomodated without the *need* for large variations of the corresponding parameter value b_c. It should not be misunderstood as a sign that small changes in b necessarily produce large λ deviations.

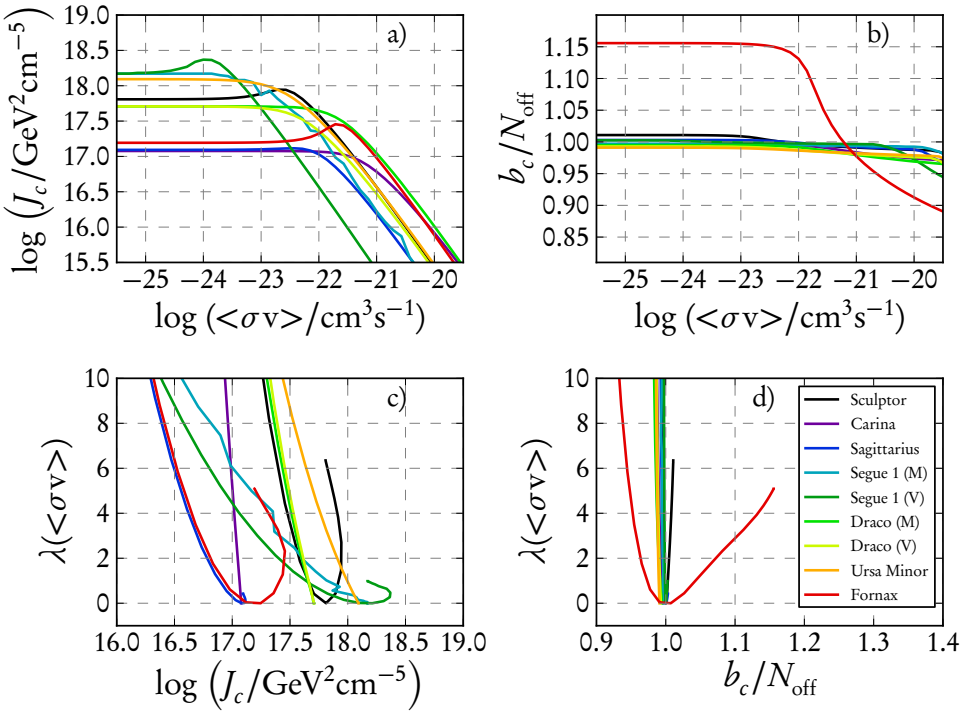

Figure 4.7: Analysis of the maximum likelihood parameters for $m_\chi = 1098.5$ GeV and DM annihilations to $b\bar{b}$ pairs. Panels a) and b) show the parameters J_c and b_c that maximize the likelihood for given values of $\langle\sigma v\rangle$, while panels c) and d) show the corresponding values of the log-likelihood function $\lambda(\langle\sigma v\rangle)$. Colours indicate the different observations as shown in the legend of panel d).

It is also illuminating to examine the values of J_c and b_c that correspond to the upper limits on the annihilation cross-section. These are shown in Table 4.5 for $m_\chi = 1098.5$ GeV, together with the respective upper limit on $\langle\sigma v\rangle$. Also shown are the mode of the J distribution, $\hat{J}$, and the number of "off"-events, which could be considered the first-order expectations for J_c and b_c. It is visible that the values of J_c and b_c are always smaller than their counterparts. The *size* of this difference apparently depends on the uncertainty of the J distribution. Probably, this behaviour is caused by the likelihood function having to "counteract" the effect of a relatively large annihilation cross-section, which would produce a larger number of signal counts than is found in the data.

Observation	$\log\langle\sigma v\rangle_{\mathrm{UL}}$	$\log J_c$	$\log \hat{J}$	σ_J	b_c	N_{off}
Sculptor	-20.9	17.59	17.81	0.2	2276.6	2283
Carina	-20.5	17.05	17.08	0.1	1844.3	1858
Sagittarius	-20.4	16.74	17.09	0.3	4250.6	4270
Segue 1 (M)	-21.3	17.54	18.17	0.6	53059.0	53301
Segue 1 (V)	-21.7	17.22	18.17	0.6	12458.5	12479
Draco (M)	-20.6	17.56	17.71	0.2	10869.4	10996
Draco (V)	-21.5	17.58	17.71	0.2	3630.7	3667
Ursa Minor	-21.6	17.89	18.09	0.3	3049.7	3084
Fornax	-19.4	16.68	17.19	0.3	116.4	122

Table 4.5: Results of calculating the single-observation profile likelihoods for $m_\chi = 1098.5\,\mathrm{GeV}$ and DM annihilations to $b\bar{b}$ pairs: This table shows the upper limits on $\langle\sigma v\rangle$ and the corresponding values J_c and b_c (for halo factor and background expectation, respectively) that provide the maximum likelihood for these particular cross-sections. The mode of the J distribution, denoted by $\hat{J}$, its uncertainty σ_J, and the number of "off"-events are shown for comparison. $\langle\sigma v\rangle$ and J are in units of $\mathrm{cm^3 s^{-1}}$ and $\mathrm{GeV^2 cm^{-5}}$, respectively.

4.3.3 Combined likelihood limits

One of the attractive features of the *combined likelihood stacking* method is the consistent treatment of all particular observational parameters. The common parameters of interest, cross-section $\langle\sigma v\rangle$ and mass m_χ, and the observation-specific nuisance parameters are all incorporated in *one* likelihood function. However, in order to actually make inferences about the dark matter parameters, the *profile* likelihood must be computed. This makes it necessary to maximise the combined function with respect to *all* other free parameters at the same time. This can be computationally costly and difficult.

However, it turns out that the particular case considered here allows a simple remedy: Since the profile likelihood functions are always calculated for *one* particular point in a grid of the parameters cross-section $\langle\sigma v\rangle$ and DM mass m_χ, these common parameters can be considered *fixed* for each calculation. Therefore, the single-observation likelihoods no longer share any common parameters, and the combined likelihood can be factorized. Thus, for each pair of $\langle\sigma v\rangle$ and m_χ values, the maximum of the combined function can be found by maximizing the single likelihoods $\mathscr{L}_i$ one at a time. For each single function, only the two observation-specific nuisance parameters J_i and b_i need to be varied, which greatly simplifies the maximization.

Equation 4.16 shows how the sequence of multiplication/summation and maximization is inverted, neglecting the m_χ dependence for clarity:

$$\ln\max\mathscr{CL}(\langle\sigma v\rangle) = \ln\max\left[\prod_i \mathscr{L}_i(\langle\sigma v\rangle)\right] = \sum_i \ln\left[\max\mathscr{L}_i(\langle\sigma v\rangle)\right]. \quad (4.16)$$

It is important to note that this inversion is only valid for fixed $\langle\sigma v\rangle$ values: The maxima of the *separate* single likelihoods $\mathscr{L}_i(\langle\sigma v\rangle)$ may well lie at *different* values of $\langle\sigma v\rangle$. Therefore, the *global* maximum of the combined likelihood with respect to the parameter $\langle\sigma v\rangle$, i.e. $\max[\mathscr{CL}]$, cannot be computed as a simple sum of the $\mathscr{L}_i$ maxima. Instead, it must be evaluated *after* all $\max[\mathscr{CL}(\langle\sigma v\rangle)]$ values have been calculated from Equation 4.16. Concerning the combined logarithmic *profile* likelihood function, this makes $\lambda_{\text{combined}} \neq \sum_i \lambda_i$, although the numerical calculation of these two values is closely related.

Hence, for each value of the dark matter particle mass m_χ, the combined λ function was computed as follows:

$$\begin{aligned}\lambda_{\text{combined}}(\langle\sigma v\rangle) &= -2\ln\mathscr{PL}_{\text{combined}} \\ &= -2\ln\left\{\frac{\max[\mathscr{CL}(\langle\sigma v\rangle)]}{\max[\mathscr{CL}]}\right\} \\ &= -2\left\{\left[\sum_i \ln\left(\max\left[\mathscr{L}_i(\langle\sigma v\rangle)\right]\right)\right] - \ln\left(\max[\mathscr{CL}]\right)\right\}\end{aligned} \tag{4.17}$$

The results of these calculations are shown in Figure 4.8 for the three considered final states of DM annihilation. Each line in the figure corresponds to one particular m_χ value. As in Figure 4.5, only every fourth mass is shown, in order to improve the visibility of the individual curves.

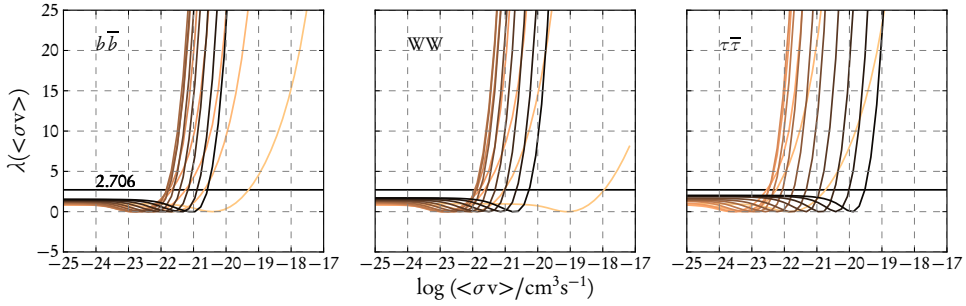

Figure 4.8: The combined logarithmic profile likelihood functions $\lambda(\langle\sigma v\rangle)$ for DM annihilations to different final states. Each curve corresponds to one particular dark matter mass m_χ in the range from 100 GeV *to* 100 TeV*, with lighter colours indicating lighter masses. The intersections of the likelihoods with the lines drawn at $\lambda = 2.706$ indicate the 95% C.L. upper limits on the annihilation cross-section $\langle\sigma v\rangle_{\text{UL}}$. These limits are shown in Figure 4.9.*

Combined limits

From these profile likelihoods, the *combined upper limit* on the annihilation cross-section $\langle \sigma v \rangle$ was derived. Figure 4.9 shows the result, together with the respective limits from the single-observation likelihoods, for dark matter annihilations to $b\bar{b}$ final states. Analogous figures for the other final states are shown in Appendix C.

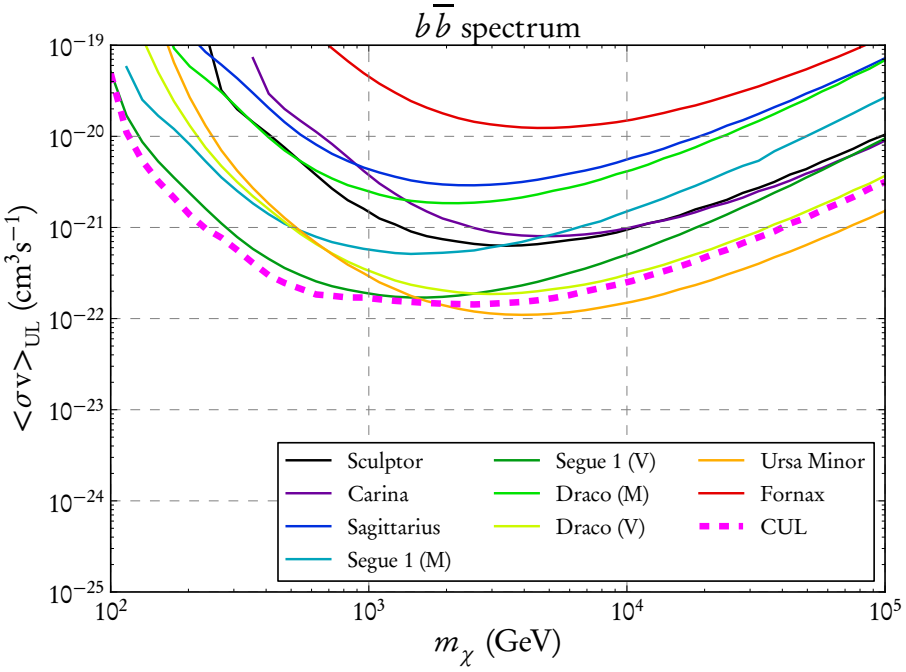

Figure 4.9: Upper limits (95% C.L.) on the DM self-annihilation cross-section $\langle \sigma v \rangle$, for annihilations to $b\bar{b}$ pairs. Solid lines indicate the limits derived from the likelihood functions of the separate observations, while the thick dashed line (CUL) shows the limit derived with the combined likelihood method. Section 4.3.4 explains why the combined limit is not always better than all single-observation limits. Figures C.3 and C.4 show the corresponding results for dark matter annihilations to W^+W^- and $\tau\bar{\tau}$ pairs, respectively.

It is visible that for dark matter masses $m_\chi > 2$ TeV, the combined limit is actually *higher* than the limit derived from the single VERITAS observation of Ursa Minor. This is explained in detail in the next section. For lower masses, however, the combination of the likelihood functions results in lowered $\langle \sigma v \rangle$ limits, as might have been expected.

Figure 4.10 shows the resulting cross-section limits for all considered final states, together with the corresponding limits obtained by the *Fermi*-LAT collaboration (Ackermann *et al.* 2011). When comparing these results, it should be kept in mind that the utilized J distributions were not the same: In particular, the uncertainties on Segue 1 and Ursa Minor, which are the main drivers of the combined

IACT limit (see Section 4.3.4), are assumed a little smaller by Ackermann *et al.* (2011). Unfortunately, it is not possible to compare these J differences directly, due to the larger integration angle $\Delta\Omega$ used for the *Fermi*-LAT observations and the corresponding J calculations.

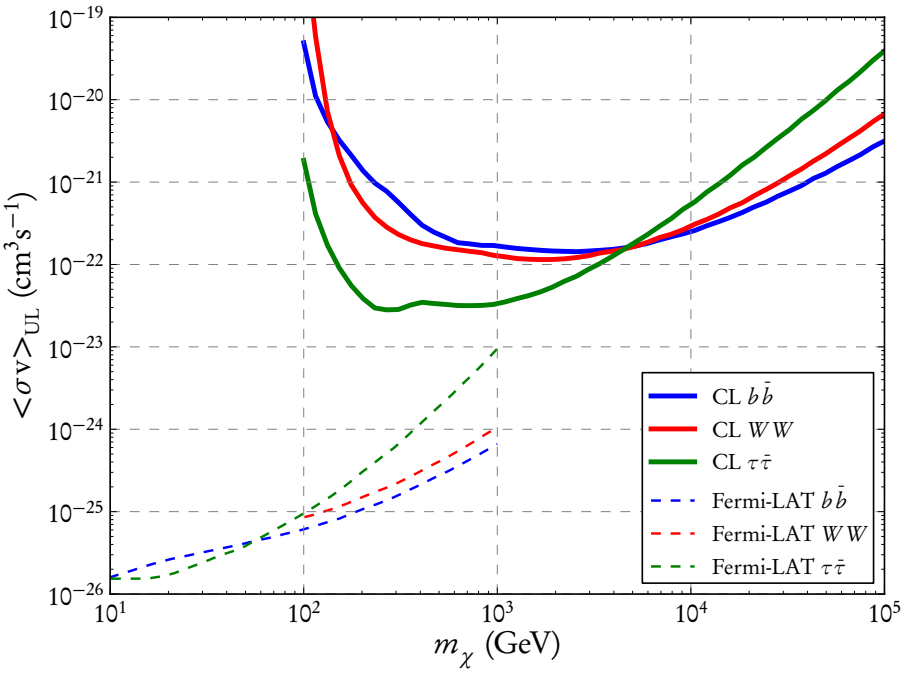

Figure 4.10: Results of the combined likelihood (CL) analysis of IACT dark matter searches. Solid lines show the upper limits on the dark matter self-annihilation cross-section $\langle\sigma v\rangle$ as a function of the dark matter mass m_χ. Colours indicate the three different annihilation final states. These upper limits at the 95% confidence level are derived from the complete set of IACT observations and include the uncertainties stemming from the J distributions. The "wiggle" in the $\tau\bar{\tau}$ limit at $m_\chi \sim 400$ GeV is caused by the inclusion of the Sculptor observation with its positive number of excess γ-ray events, compare Figure C.6 in Appendix C. For comparison, dashed lines show the upper limits obtained from Fermi-LAT observations (Ackermann et al. 2011).

4.3.4 The combination of likelihoods: A closer look

It may seem surprising that the combination of likelihood functions, and thus a "stacking" of several different data sets, results in a deterioriation rather than an improvement of the constraints that can be derived from the data. However, this was clearly the case for the limit on the dark matter self-annihilation cross-section $\langle\sigma v\rangle$ in the previous section. As it turns out, this behaviour can be related to the likelihood functions of the different single observations:

It was shown in Section 4.3.3, Equation 4.17, how the combined λ function can be expressed as a sum over the maximized single-observation log-likelihoods, minus the offset provided by the global maximum. It is instructive to take a closer look at the effects of this summation. Figure 4.11 shows the single-object log-likelihoods $\lambda(\langle\sigma v\rangle)$ together with their respective combinations, for two different sets of data and two dark matter mass values.

In the upper panels, a relative decline in the log-likelihood of Sculptor is clearly visible for the cross-section range from 10^{-22} to 10^{-21} cm^{3}s^{-1}. This is caused by a positive number of excess events, corresponding to a non-significant γ-ray signal. However insignificant, this decline counteracts the rise in the λ functions of the other observations. Therefore, the *combined* likelihood is smaller and the corresponding upper limit on $\langle\sigma v\rangle$ is *higher* than it would be if Sculptor were not included at all. The same potentially applies for all observations with a positive number of signal counts, if the corresponding cross-section is in the range where other observations might provide an upper limit.

In the lower panels of Figure 4.11, on the other hand, the single likelihoods combine as "expected", yielding a lowered limit on $\langle\sigma v\rangle$. One can also see, however, that the combined λ function is strongly dominated by the Carina likelihood for $m_\chi = 9103$ GeV.

In order to test for the size of these effects, likelihood combinations of different sets of data were performed, removing the observations with "positive signal" one after another. In addition, the two VERITAS observations of Segue 1 and Ursa Minor were combined, because these provide the most stringent single-object limits in the dark matter mass ranges below and above ~ 2 TeV, respectively. Figure 4.12 shows the resulting upper limits on the cross-section, for annihilations to $b\bar{b}$. It can be seen that the Sculptor data in particular have a strong impact on the combined limit. On the other hand, the Fornax cluster data do not play a significant role, even though the dip in their likelihoods is comparable to that of Sculptor's. This is because the maximum likelihood value of $\langle\sigma v\rangle$ corresponding to the γ-ray "excess" occurs at higher cross-sections, see Figure 4.5. Probably, this behaviour is due to a combination of the relatively small J factor of Fornax, the energy threshold at 260 GeV and the positive fluctuation of γ-ray events.

Comparing the green, cyan and magenta lines, it also becomes clear that the combined likelihood limit is not only determined by the data from the two VERITAS observations of Segue 1 and Ursa Minor. The other data sets also play a relevant role, despite the distinct influence of Segue 1 on the limits in the mass ranges below and above a few TeV, respectively.

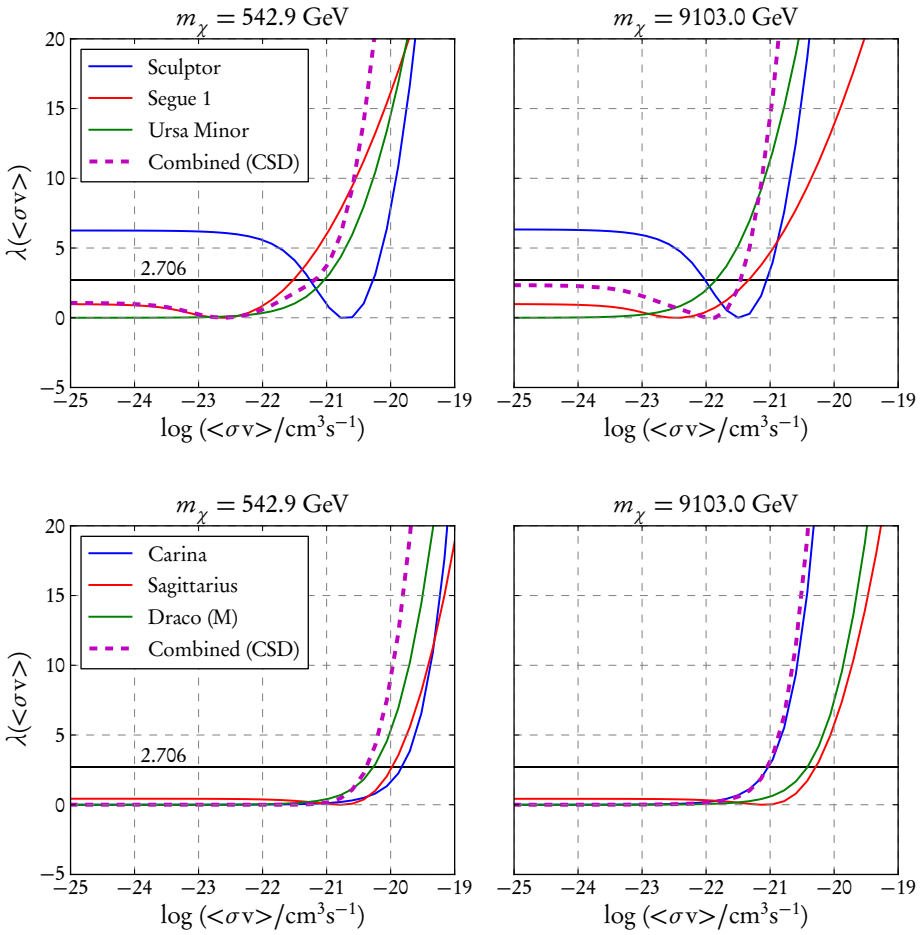

Figure 4.11: A closer look at the profile likelihoods of single observations, and the effect of their combination: The upper panels show the λ functions of Sculptor, Segue 1 (VERITAS) and Ursa Minor together with the combination (SSU) of these three likelihoods, for two different DM particle masses. The lower panels show the likelihoods of Carina, Sagittarius and Draco (MAGIC), again together with their combination (CSD). It is visible how the non-significant "signal" from Sculptor lowers the combined likelihood in the first case, while there is almost no such effect in the second combination.

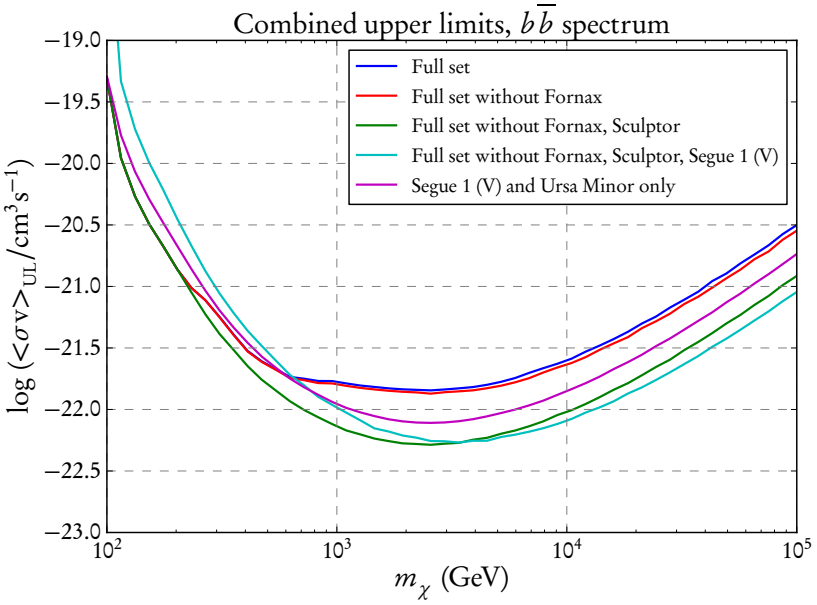

Figure 4.12: Comparison of combined limits on $\langle\sigma v\rangle$, for DM self-annihilations to $b\bar{b}$ pairs. The upper limits (95% C.L.) are derived from the different sets of data indicated in the legend. In particular, the strong effect of the Sculptor and Segue 1 observations on the combined limit is clearly visible. Appendix C shows the corresponding figures for DM annihilations to W^+W^- and $\tau\bar{\tau}$ pairs.

A final test case

In order to show that the combined likelihood method *can* provide valuable results, i.e. cross-section limits that improve over the results from single observations, a hypothetical test case was constructed: Since the VERITAS observations of Segue 1 and Ursa Minor provided the most stringent limits, the effect of combining several observations *exactly like these* was investigated. More precisely, a combined likelihood analysis was performed that used both of the two data sets *five* times. Figure 4.13 shows the resulting upper limit on the annihilation cross-section, for single observations of the two targets, and for the combination of $2 \times 5 = 10$ data sets.

Essentially, the combination of five equal data sets means the summation of five equal log-likelihoods. It results in a combined λ function that is five times steeper, and hence in a lowered upper limit on $\langle\sigma v\rangle$, as is visible in Figure 4.13. The figure also shows, for $m_\chi \sim 1.5$ TeV, that the improvement can be even larger than the factor $\sim \sqrt{10}$ that could be expected from simply collecting ten times as much data.

Obviously, real data sets will never be exactly equal. Nevertheless, this test case shows that a tighter limit on the annihilation cross-section can be expected if the

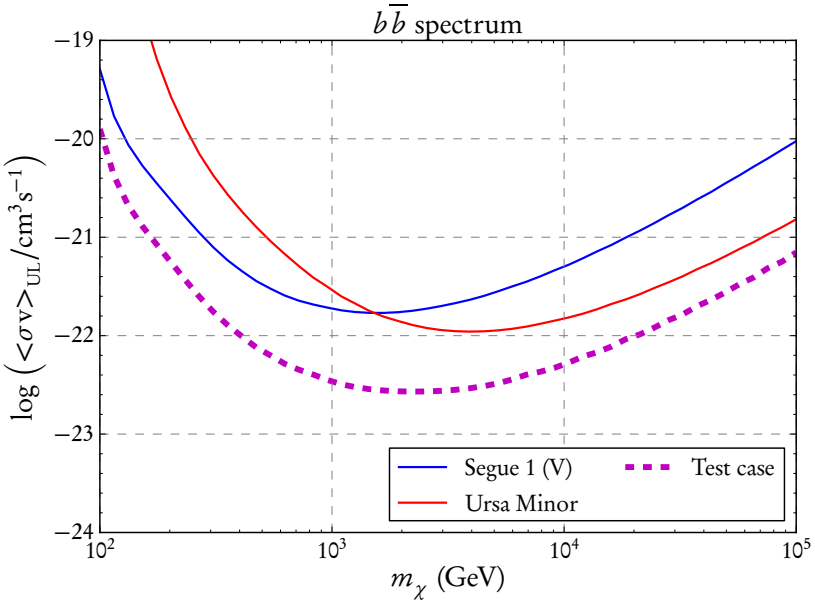

Figure 4.13: Artificial test case: While the 95% C.L. upper limits on $\langle\sigma v\rangle$ from Segue 1 and Ursa Minor (solid lines) are those derived from the actual VERITAS data, the dashed line shows the limit that would be produced by the five-fold combination of these two datasets. Shown here is the case of dark matter self-annihilation to $b\bar{b}$ pairs; corresponding results for W^+W^- and $\tau\bar{\tau}$ final states are shown in Figures C.7 and C.8.

combined data fulfill two criteria: First, the likelihoods should depend on $\langle\sigma v\rangle$ in a roughly similar fashion. Otherwise, the combined profile log-likelihood will be dominated in the crucial region between zero and 2.706 by the data set that gives the lowest limit in itself. Secondly, data sets which indicate an actual signal, although insignificant, can strongly influence the combined likelihood. This may even cause the combined limit to be worse than single-target limits, as was seen in this section. It is certainly not an acceptable remedy for this effect to simply exclude such data sets from the analysis, as the result would be strongly biased. It may, however, be helpful to concentrate on data sets that are *roughly* similar in their statistical uncertainties and $\langle\sigma v\rangle$ sensitivity, in order to avoid strong effects from outliers.

4.4 Summary and conclusions

A new statistical technique, which may be called *combined likelihood stacking*, has been introduced for the combination of dark matter searches that were performed with different imaging air Cherenkov telescopes (Section 4.1). It integrates published results from a variety of telescopes and astronomical targets (Section 4.2) in a way that is both methodologically solid and flexible. No significant signal

of γ-rays from dark matter self-annihilations was found, neither in the separate observations nor in their combination. Therefore, upper limits were derived on the velocity-weighted annihilation cross-section $\langle\sigma v\rangle$, for dark matter particle masses m_χ in the range from 100 GeV to 100 TeV. The results are summarized below.

Apart from the event numbers and background suppression factors, which are usually made public, the combined likelihood method relies on the effective detection areas of the observing instruments. For most of the results presented here, these were taken from publications not directly related to the dark matter searches, which induces some degree of uncertainty. Obviously, this could be improved if the effective areas corresponding to each measurement were made public by the telescope collaborations. Nevertheless, the performed cross-checks (Section 4.3.1, Figure 4.4) showed that the induced errors on the cross-section limits were on a reasonable level, no larger than a factor of two for most observations and most of the m_χ range.

In addition to the (unprecedented) combination of data from different telescopes, the combined likelihood method allows a consistent statistical treatment of the observational uncertainties related to the dark matter haloes, as parametrized by the "J factor" probability distributions (Sections 4.1.2 and 4.2.1). Following the example of the *Fermi*-LAT collaboration (Ackermann *et al.* 2011), and using J factor PDFs published elsewhere (see Section 4.2.1 for the references), this is the first time that this treatment has been applied to dark matter searches with Cherenkov telescopes.

Using the combined likelihood method, upper limits on the dark matter self-annihilation cross-section $\langle\sigma v\rangle$ have been calculated both for the single observations (Section 4.3.2) and for their combination (Section 4.3.3). The single-target calculations show that including the J factor uncertainties can strongly influence the resulting limit (Figure 4.6). Differences up to a factor ~ 3 are induced by properly taking account of these uncertainties, in particular for the VERITAS observation of Segue 1. These differences stem from the likelihood-based estimations of the nuisance parameters J and b (halo factor and background expectation, respectively), which are explored in Figure 4.7 and Table 4.5.

Figure 4.9 shows how the $\langle\sigma v\rangle$ limit from the *combined* likelihood analysis compares with the single-observation limits, for dark matter annihilating to $b\overline{b}$ pairs. Corresponding results for DM annihilations to W^+W^- and $\tau\overline{\tau}$ pairs are shown in Appendix C, Figures C.3 and C.4. The "combined limits" reach values $\langle\sigma v\rangle_{\mathrm{UL}} \approx 10^{-22}$ cm^{3}s^{-1} for dark matter particles masses $m_\chi \sim 1$ TeV. In the $\tau\overline{\tau}$ case, the harder γ-ray spectrum results in limits $\langle\sigma v\rangle_{\mathrm{UL}} \approx 3\times10^{-23}$ cm^{3}s^{-1} for DM masses below 1 TeV. Figure 4.10 shows a compilation of the combined limits for the three different annihilation final states.

The effect of combining different data sets on the $\langle\sigma v\rangle$ limit is mixed: Depending on the DM particle mass and the included data sets, the resulting cross-section limit can be *lower* than the single-observation limits, but sometimes also *higher*.

This depends on the particular shape of the individual likelihood functions, as is explored further in Section 4.3.4. Figure 4.12 shows the combined upper limit for different combinations of data sets.

In addition, an artifical combination of the most constraining single-target data sets, the VERITAS observations of Segue 1 and Ursa Minor, was tested. In this case, the combined likelihood method results in lowered $\langle \sigma v \rangle$ limits, see Figure 4.13. The improvement is comparable to or better than what would be expected from a naive extrapolation of additional observation time.

Comparison with *Fermi*-LAT results (Figure 4.10) illustrates a deficiency of IACT dark matter searches: While the all-sky coverage of the *Fermi* satellite allowed Ackermann *et al.* (2014) to observe and analyze 25 dwarf spheroidal galaxies, the number of dwarfs observed by ground-based telescopes is still rather small. H.E.S.S. in particular is somewhat hampered by the fact that most of the known dwarf galaxies were found in the northern hemisphere, not observable from Namibia. However, this situation may improve with new and upcoming astronomical surveys like PanSTARRS (Kaiser *et al.* 2002), the DES (The Dark Energy Survey Collaboration 2005), the Southern Sky Survey (Keller *et al.* 2007) and the LSST (Ivezic *et al.* 2008). Many more dwarf galaxies are expected to be found (e.g. Koposov *et al.* 2008; Tollerud *et al.* 2008). A recent example is the discovery of a new Milky Way satellite in the southern hemisphere by Belokurov *et al.* (2014). However, its relatively large distance of 170 kpc makes it a suboptimal target for a dark matter search with the H.E.S.S. telescopes.

Further prospects for the future development of dwarf galaxy dark matter searches can be found in Chapter 6.

Chapter 5

A search for dark matter in the Fornax cluster with H.E.S.S.

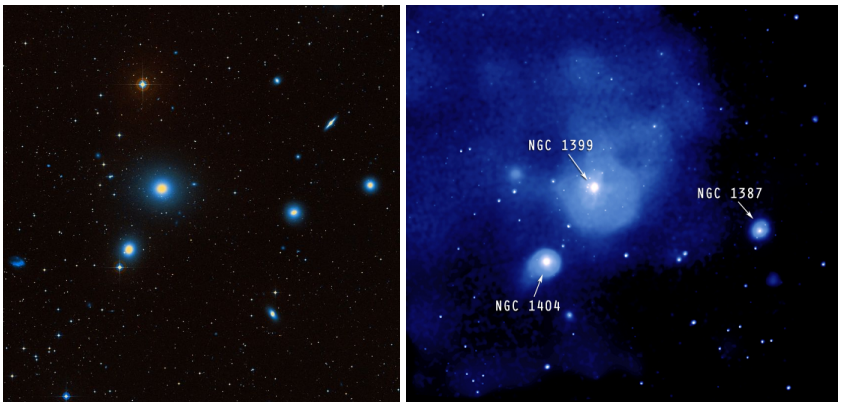

Figure 5.1: The central part of the Fornax cluster of galaxies. Left: optical image (DSS2, `wikisky.org`*); right: X-ray image (*`chandra.harvard.edu/photo/2004/fornax/more.html`*). The brightest galaxy towards the middle is NGC 1399; southeast of it, NGC 1404, at an angular distance of about 10'.*

Clusters of galaxies are the largest virialized structures in the Universe (e.g. Voit 2005; Kravtsov & Borgani 2012). Their internal dynamics are dominated by dark matter, with the deepest troughs of the gravitational potential at or close to their central galaxies. This makes galaxy clusters interesting search targets for signals of dark matter annihilations. For instance, the MAGIC (Aleksić *et al.* 2010) and *Fermi*-LAT (Ackermann *et al.* 2010) collaborations have performed dedicated analyses in the γ-ray channel, while a search for neutrinos from DM annihilations has been performed with IceCube (Aartsen *et al.* 2013). Possible radio signals from dark matter in clusters have also been investigated, e.g. by Storm *et al.* (2013).

Theoretical modelling of the expected γ-ray flux from DM annihilations has been performed by Colafrancesco *et al.* (2006), Jeltema *et al.* (2009) and Pinzke *et al.*

(2009), among other authors. Sánchez-Conde *et al.* (2011) have explicitly compared the flux expectation from galaxy clusters with that from dwarf spheroidal galaxies, cf. Chapter 4. Their conclusion depends on the role played by substructures in the DM haloes of clusters, a topic that will be investigated in Section 5.1.

Clusters of galaxies can also act as sources of γ-rays produced by the interaction of hadronic cosmic rays (CR) with the intracluster medium. Jeltema *et al.* (2009) and Pinzke *et al.* (2011) have compared the respective flux expectations for both dark matter-induced and cosmic ray-induced γ-rays. Both conclude that the Fornax cluster shines particularly bright in γ-rays from DM annihilations, while the CR-induced flux is relatively low. While in principle it is possible to model the γ-ray flux fraction from CR interactions, and thus to put tighter constraints on a possible dark matter contribution, the uncertainties induced by this procedure are rather high. Therefore, the cosmic ray contribution to the γ-ray flux was neglected completely in the analysis presented here.

The results presented in this chapter were produced in close collaboration with Aion Viana[1] and published by the H.E.S.S. collaboration (Abramowski *et al.* 2012), with an erratum concerning the published figures (Abramowski *et al.* 2014). The observational results (in terms of event numbers) that are shown in the publication were produced by Aion, using the "model" analysis framework (see Chapter 3 and Section 5.2 below). I provided a cross-check using the Hillas-based analysis framework set up at Hamburg University. Both the published values and the cross-check results are reproduced below. The calculation of limits on the γ-ray flux and on dark matter parameters was always performed by both of us, using the published event numbers. While the figures for the H.E.S.S. publication were also produced by Aion, this chapter shows the corresponding figures I made for comparison. I have corrected the normalization error that made the erratum necessary.

5.1 Dark matter in the Fornax galaxy cluster

The cluster of galaxies in the constellation Fornax (Abell S0373) is located in the southern hemisphere at the distance $d = (19.9 \pm 0.4)$ Mpc (see Tonry *et al.* 2001). Its central cD galaxy, NGC 1399, resides at RA $= 03^{\mathrm{h}}38^{\mathrm{m}}29\overset{\mathrm{s}}{.}3$ and Dec $= -35°27'00\overset{''}{.}7$ (J2000.0). It was observed with the H.E.S.S. telescopes with the initial aim to study its quiescent supermassive black hole (Pedaletti *et al.* 2008, 2011). However, several authors ranked Fornax as a promising target for dark matter searches (Jeltema *et al.* 2009; Pinzke *et al.* 2009; Pinzke *et al.* 2011). Therefore, these data were re-analysed using a method particularly suited to this type of target, see Section 5.2.

Compared to other clusters like Virgo or Coma, Fornax is rather light, with an X-ray-determined mass of about 10^{14} $M_\odot$ (Reiprich & Böhringer 2002). Concerning the expected dark matter signal, this is partly ameliorated by its relative

[1] aion.viana@mpi-hd.mpg.de

proximity: Table 5.1 compares several galaxy clusters that have been observed with Cherenkov telescopes. In contrast to Fornax, γ-ray observations of Virgo are dominated by the emission of its central radio galaxy M87 (average flux $\Phi(E > 730\,\mathrm{GeV}) \approx 0.5 \times 10^{-13}$ cm^{-2}s^{-1}, Aharonian *et al.* 2006c). Coma is located further away and can only be observed with H.E.S.S. at high zenith angles, leading to a high energy threshold (cf. Chapter 3 and Aharonian *et al.* 2009). This applies even more so for the Perseus cluster, which has been observed with MAGIC (e.g. Aleksić *et al.* 2012a).

	D (Mpc)	M (10^{14} M$_\odot$)	Right ascension	Declination
Fornax	20.0	0.9	$03^h38^m27\overset{s}{.}9$	$-35°26'54''$
Virgo	16.5	4.0	$12^h30^m47\overset{s}{.}3$	$+12°20'13''$
Coma	100.0	13.0	$12^h59^m48\overset{s}{.}7$	$+27°58'50''$
Perseus	72.3	6.7	$03^h19^m47\overset{s}{.}2$	$+41°30'47''$

Table 5.1: Clusters of galaxies. Distance D and mass M are quoted here as compiled by Weinmann et al. *(2011), where the corresponding references can be found. The equatorial coordinates (J2000) were extracted from NED,* `ned.ipac.caltech.edu`.

However, in order to estimate the expected γ-ray flux from dark matter annihilations, not only the mass of the cluster needs to be known, but also the dark matter density profile, which is the subject of the next section.

5.1.1 Mass profiles of Fornax and NGC 1399

There are several different methods to determine the mass profile of galaxies or galaxy clusters, as was described in Section 2.1.4. In the case of the Fornax cluster and its central elliptical galaxy NGC 1399, the following studies have been performed: Saglia *et al.* (2000) analysed the stellar velocity dispersion of NGC 1399 and found that the "gravitational potential is dominated by the luminous component out to the last data point", which was located at the angular distance $r_a = 97''$ from the centre. Schuberth *et al.* (2010) have observed the globular cluster system around NGC 1399 out to larger radii, with the largest projected radius $r = 80$ kpc corresponding[2] to $r_a = 14.5'$. This allowed them to trace the dark matter halo of NGC 1399, though with uncertainties related to apparently different dynamical histories of "red" (metal-rich) and "blue" (metal-poor) globular clusters. Drinkwater *et al.* (2001) performed a dynamical analysis of 108 member galaxies of Fornax out to about 1.4 Mpc, or $r_a = 250'$.

In addition to these analyses, which use optical observations of dynamical tracers of the gravitational potential, X-ray studies of the cluster (cf. Section 2.1.4) have also been used to derive mass profiles. Ikebe *et al.* (1996) and Paolillo *et al.*

[2]Following Schuberth *et al.* (2010), a distance of 19 Mpc to Fornax is assumed in the remainder of this chapter. Therefore, an angle of 1′ is equivalent to a distance of 5.5 kpc perpendicular to the line of sight.

(2002) show evidence for distinct dark matter haloes on both the scales of the central galaxy and the cluster as a whole, but Schuberth *et al.* (2010) do not confirm the onset of the cluster halo. Figure 22 of their publication shows a comparison of different profiles and is therefore reproduced here, see Figure 5.2.

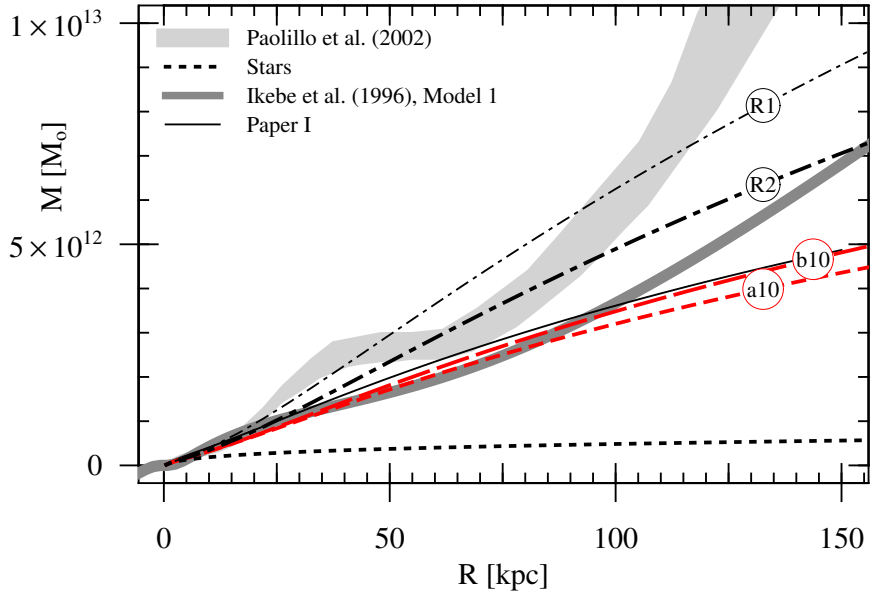

Figure 5.2: Enclosed mass profiles of the galaxy NGC 1399 in the centre of the Fornax cluster. This is Figure 22 of Schuberth et al. *(2010). The grey shaded area and thick grey line show the mass profiles (or profile ranges) derived by Paolillo* et al. *(2002) and Ikebe* et al. *(1996), who find a transition from the galactic DM halo to that of the cluster, and a corresponding "shoulder"-like feature in the DM mass profile. This is not observed by Schuberth* et al. *(2010), whose results are labelled* a10 *and* b10*. Note that the tracer data from which these profiles are derived extend to a projected radius of 80 kpc. (The lines labelled* Paper 1, R1 *and* R2 *are from Richtler* et al. *(2008), while the black short-dashed line shows the stellar mass alone.)*

Yet a different approach is to use X-ray observations which yield the virial mass of the cluster (Reiprich & Böhringer 2002) together with the mass-concentration relation ($c(M)$, Equation 2.10) predicted for cold dark matter haloes to match a DM density profile to the cluster's mass. This approach has been used for the *Fermi*-LAT dark matter analysis of galaxy clusters, including Fornax (Ackermann *et al.* 2010).

The different measurements of galaxy or cluster mass and mass profiles yield different results, although they are generally consistent with a profile of the Navarro-Frenk-White (NFW) type (see Equation 2.5, Section 2.1.3, Navarro *et al.* (1996) and Navarro *et al.* 1997). There is, however, significant spread in the NFW halo parameters r_s and ρ_s. Table 5.2 summarises the halo models and the corresponding dark matter "halo factors" $\bar{J}$ (cf. Section 2.3.1). These factors are

NFW profile			$\vartheta_{\max}$:	0.1°	0.5°	1.0°
Model	r_s (kpc)	ρ_s $(10^{-3}\,M_\odot pc^{-3})$	$\bar{J}$ $(10^{21}\,GeV^2cm^{-5})$			
SR10 a_{10}	34	8.8		15.0	0.6	0.2
SR10 a_6	200	0.6		7.0	0.5	0.1
DW01	220	0.5		6.2	0.5	0.1
RB02	98	5.8		112.0	6.5	1.7
Burkert profile						
Model	r_c (kpc)	ρ_c $(10^{-3}\,M_\odot pc^{-3})$	$\bar{J}$ $(10^{21}\,GeV^2cm^{-5})$			
SR10 $a_{10,b}$	12	72.8		15.0	0.6	0.2
SR10 $a_{6,b}$	94	3.1		2.4	0.5	0.1
$\Delta\Omega$ $(10^{-6}$ sr)				9.57	239	957

Table 5.2: Dark matter halo models for NGC 1399 and the Fornax galaxy cluster. The first three columns show the selected profiles discussed in Section 5.1.1 with their respective NFW or Burkert halo parameters $r_{s/c}$ and $\rho_{s/c}$. The last three columns show the astrophysical factor $\bar{J}$ for the three different integration angles $\vartheta_{\max}$. The model abbreviations are explained in the main text. For convenience, the last row shows the solid angles corresponding to the three values of $\vartheta_{\max}$. A plot of these halo profiles is shown in Figure 5.3.

computed as

$$\bar{J}(\Delta\Omega) = \frac{1}{\Delta\Omega}\int_{\Delta\Omega} d\Omega \int_{\text{l.o.s.}} dl\ \rho^2(r(l))\ , \tag{5.1}$$

along the line of sight (l.o.s.) of an observation and within a cone of solid angle $\Delta\Omega = 2\pi\,(1-\cos\vartheta_{\max})$. Hence, the value of the $\bar{J}$ factor depends on the halo profile $\rho(r)$ as well as the integration angle $\vartheta_{\max}$.

Table 5.2 shows that the dark matter halo derived by Drinkwater *et al.* (2001), DW01, agrees quite well with model *a6* of Schuberth *et al.* (2010), SR10. This model is derived from the dynamics of the "blue" globular clusters. However, Schuberth *et al.* (2010) recommend "to use a dark halo based on the red GCs alone", since these appear to trace the galaxy's mass profile more faithfully. Model *a10* is derived from these observations. These data sets can also be fitted by cored "Burkert" profiles (Equation 2.7, Section 2.1.3), the parameters of which are shown in the last two rows.

On the other hand, Model RB02 denotes the NFW halo parameters computed from the X-ray mass (Reiprich & Böhringer 2002) with the $c(M)$ relationship (Buote *et al.* 2007). This procedure results in a heavier dark matter halo, which yields a considerably higher $\bar{J}$ factor.

The dark matter halo profiles $\rho(r)$ given in Table 5.2 are illustrated in Figure 5.3. Figure 5.4 shows, in dashed lines, the volume integral $\Lambda(r) = \int^r dV\rho^2$

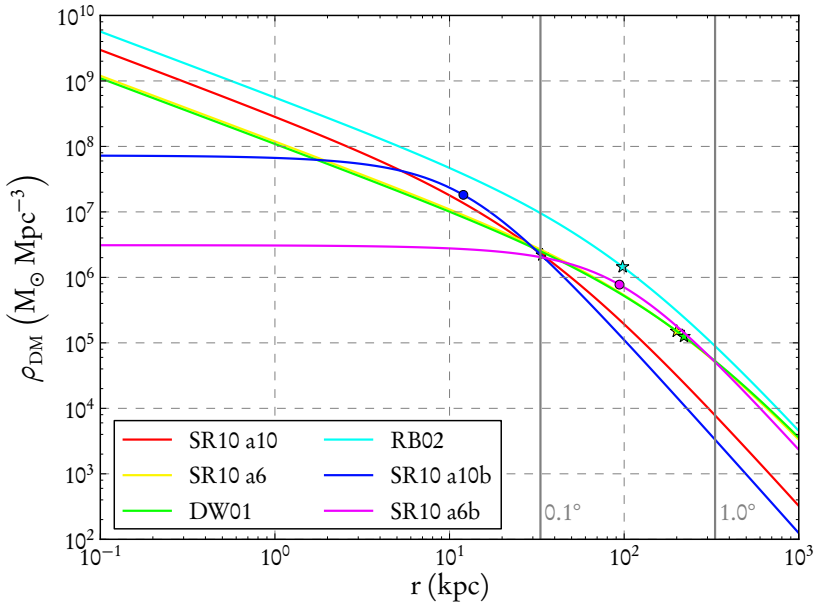

Figure 5.3: Dark matter density profiles of the Fornax galaxy cluster. The lines of different colours correspond to the halo models given in Table 5.2, with the scale (core) radii of the NFW (Burkert) haloes indicated by a star (circle). Grey vertical lines indicate the angular distances 0.1° and 1.0° from the cluster centre, for a distance of 19 Mpc to Fornax.

over spherical regions with radius r from the cluster centre. The γ-ray luminosity from dark matter self-annihilations within such a sphere would be proportional to this integral. In addition, the logarithmic differential $\mathrm{d}\Lambda/\mathrm{d}\log r \propto r^3\rho^2$ is shown. This may serve to indicate the "shells" of equal radial distance that yield the strongest DM annihilation signal. (The angular dependence of the actual $\bar{J}$ value is more difficult to evaluate, therefore it is not shown in this plot.)

It is visible in Figure 5.3 how the NFW halo profiles differ from the cored Burkert profiles in the inner few kpc. However, this is also where the stellar mass actually dominates the density profile, so that baryonic effects may have altered the dark matter density in this region. On the other hand, Figure 5.4 shows that for all haloes, the DM annihilation flux is dominated by the radial distance range $r \sim 10 - 100$ kpc. Therefore, the innermost slope of the DM density is not particularly important in this case: The $\bar{J}$ factors from the two SR 10 a_{10} models are almost the same, regardless of whether a cored or an NFW profile is used. For all DM haloes, almost the entire γ-ray flux originates from within their virial radii, which lie in the range from a few hundred kpc to about 1 Mpc.

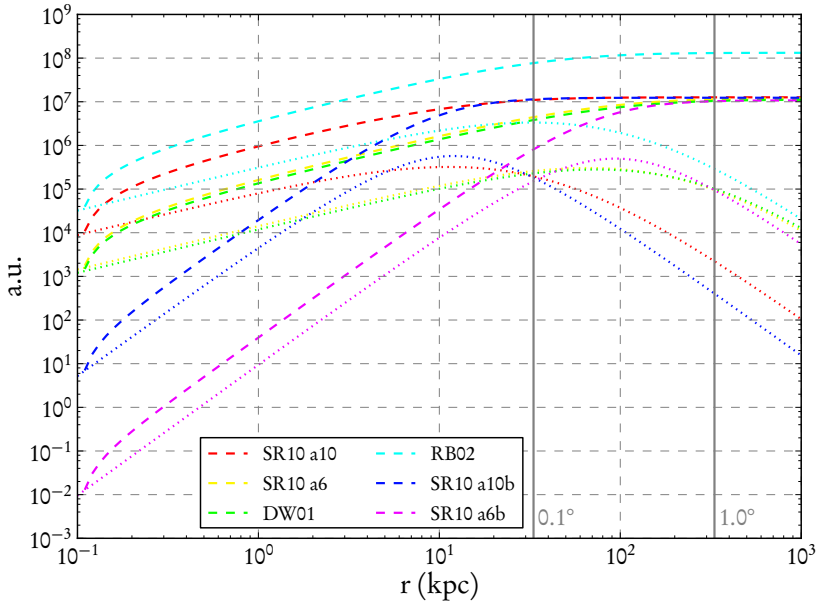

Figure 5.4: Dark matter self-annihilation luminosities. Corresponding to the halo profiles shown in Figure 5.3, the dashed lines show the radial profile of the expected signal $\propto \int^r \mathrm{d}V\,\rho^2$. *The dotted lines show the differential flux contribution* $\propto r^3\rho^2$ *per radial unit* $\mathrm{d}\log r$. *All values are in arbitrary units. Potential flux enhancement from substructures, as discussed in Section 5.1.2, is* not *considered here. Again, the grey vertical lines indicate the angular distances 0.1° and 1.0° from the cluster centre.*

5.1.2 Flux enhancement from DM halo substructure

As mentioned in Section 2.1.2, simulations of cold dark matter structure formation predict numerous substructures within the dark matter haloes of galaxies, and hence also within galaxy clusters. (Obviously, galactic DM haloes *are* substructures of their main cluster halo, and the elliptical galaxy NGC 1404 even lies within the virial radius of NGC 1399.)

These subhaloes have a higher dark matter density than the smooth halo component by which they are surrounded, and therefore enhance the γ-ray flux from dark matter annihilations. Pinzke *et al.* (2009) have utilized the results of the *Aquarius* halo simulation (Springel *et al.* 2008b) to compute this additional flux from DM substructure. The enhancement factor or "boost" from this contribution with respect to the annihilation luminosity $\mathscr{L}_{\mathrm{sm}}$ from the smooth halo can be defined as

$$B_{\mathrm{sub}}(\Delta\Omega) = 1 + \frac{\mathscr{L}_{\mathrm{sub}}(\Delta\Omega)}{\mathscr{L}_{\mathrm{sm}}(\Delta\Omega)}\,, \tag{5.2}$$

where $\Delta\Omega$ denotes the solid angle of integration. Pinzke *et al.* (2009) obtained the

luminosity from substructures inside a *sphere* of radius r as

$$\mathscr{L}_{\rm sub}(r) = 0.8\, C\, \mathscr{L}_{\rm sm}(r_{200}) \times (r/r_{200})^{0.8(r/r_{200})^{-0.315}} . \tag{5.3}$$

Here, $\mathscr{L}_{\rm sm}(r_{200})$ is the luminosity from the smooth halo inside the virial radius r_{200}, which they take as the radius of a sphere enclosing a mean density 200 times the critical density of the universe (cf. Section 2.1.3). The normalization

$$C = (M_{\rm min}/M_{\rm lim})^{0.226} \tag{5.4}$$

depends on $M_{\rm min} = 10^5\ {\rm M}_\odot$, the smallest halo mass resolved by the Aquarius simulation, and the intrinsic limiting substructure mass $M_{\rm lim}$ (also known as "free-streaming mass", Section 2.1.2), which depends on the properties of the dark matter particles. Factoring the halo-independent source term out of the γ-ray luminosity yields

$$\mathscr{L}(r) \propto \int_{V(r)} {\rm d}V \rho^2 = \Lambda(r) , \tag{5.5}$$

which is valid for both the smooth and the structured part of the dark matter halo. Therefore, by differentiating Equation 5.3 with respect to the radius, one can compute the *effective* squared substructure density profile as

$$\tilde{\rho}^2_{\rm sub}(r) = A(r) \times \frac{0.8\, C\, \Lambda_{\rm sm}(r_{200})}{4\pi r^2 r_{200}} \left(\frac{r}{r_{200}}\right)^{-B(r)} , \tag{5.6}$$

where

$$A(r) = 0.8 - 0.252\, \ln(r/r_{200}) \tag{5.7}$$

and

$$B(r) = 1.315 - 0.8 \times (r/r_{200})^{-0.315} . \tag{5.8}$$

This effective substructure density can be used to calculate the subhalo flux contribution not only from within a sphere, but also for any other volume. In particular, this applies to the *cone* of solid angle $\Delta\Omega$ in which the halo factor $\bar{J}(\Delta\Omega)$ is calculated.

The absolute value of the substructure enhancement depends strongly on the free-streaming mass $M_{\rm lim}$. Below this mass scale, gravitationally bound subhaloes cannot form, due to the relative motion of the dark matter particles. However, $M_{\rm lim}$ is many orders of magnitude below the resolution limit of dark matter simulations. A conventional value is $M_{\rm lim} = 10^{-6}\ {\rm M}_\odot$ (Diemand *et al.* 2006), although a broad range of values down to $M_{\rm lim} = 10^{-12}\ {\rm M}_\odot$ is possible for different particle dark matter models (Bringmann 2009). Pinzke *et al.* (2009) derive the lower limit $M_{\rm lim} > 5 \times 10^{-3}\ {\rm M}_\odot$, but this depends on a particular model of dark matter (Bergström *et al.* 2009), annihilating to $\mu\mu$ pairs with a cross-section determined by a fit to the CR positron fraction as measured by the *PAMELA* satellite (Adriani *et al.* 2009).

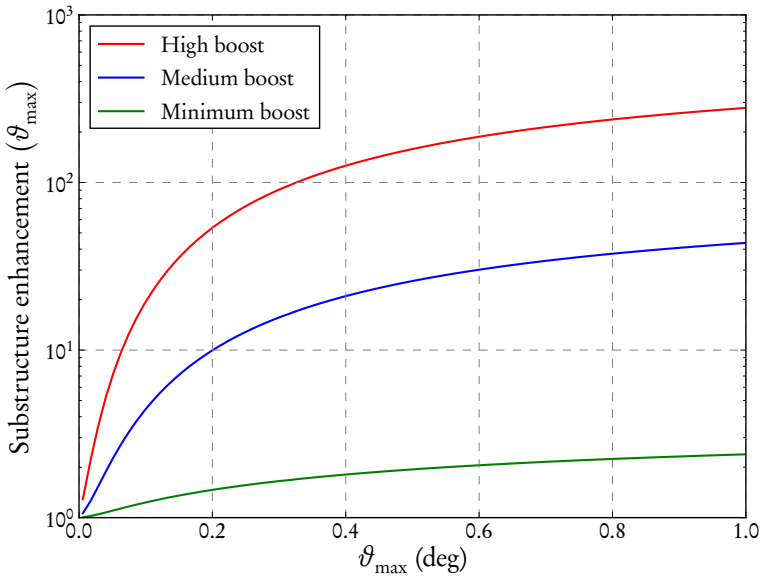

Figure 5.5: Boost factors, i.e. the enhancement from dark matter substructures with respect to the γ-ray flux from a smooth halo, as a function of the opening angle of integration $\vartheta_{\max}$. The high boost results from the conventional value of the free-streaming mass $M_{\lim} = 10^{-6}$ M$_\odot$, while the medium boost corresponds to $M_{\lim} = 5 \times 10^{-3}$ M$_\odot$ as derived by Pinzke et al. (2009). The minimal boost is calculated by setting $M_{\lim} = M_{\min} = 10^5$ M$_\odot$. All boost factors were computed using Equations 2.19 and 5.6 for the NFW halo SR10 a_{10}.

For the analysis presented here, the substructure boost was calculated for three different values. $M_{\lim} = 10^{-6}$ M$_\odot$ and $M_{\lim} = 5 \times 10^{-3}$ M$_\odot$ induce a *high* and a *medium* value of the enhancement, respectively. In addition, a "minimal" boost was computed by setting $M_{\lim} = M_{\min} = 10^5$ M$_\odot$ in Equation 5.6, so that no extrapolation beyond the resolution of the Aquarius simulation was performed.[3]

Figure 5.5 shows the enhancement factor for all three scenarios, computed for the NFW halo model SR10 a_{10}, as a function of the opening angle $\vartheta_{\max}$ of the $\bar{J}$ factor integration. It may be noted that Nezri *et al.* (2012) have analyzed the effect of different models of dark matter substructure on this γ-ray flux enhancement, and found that the uncertainties can amount to one or two orders of magnitude. Hence, the differences between the models used here can serve to indicate these theoretical uncertainties. See also Anderhalden & Diemand (2013), who argue that the $c(M)$ relation of DM haloes is no longer a power law at the small scales below typical simulation resolutions. This results in much smaller substructure luminosity boost factors, on the order of a few for a Milky Way-like halo, but Anderhalden & Diemand (2013) do not show results for clusters of galaxies.

The large possible boost factors derived for large integration angles provide a reason to perform a γ-ray observation in *extended* search regions, as opposed to

[3] This calculation was not presented by Abramowski *et al.* (2012, 2014).

$\vartheta_{\max}$	0.1°	0.5°	1.0°
Minimal boost	1.2	1.9	2.4
Medium boost	4.4	25.8	43.6
High boost	19.4	158.3	278.6

Table 5.3: Substructure enhancement. Shown here are the numerical values of the boost factors depicted in Figure 5.5 that correspond to the three different integration angles $\vartheta_{\max}$ used in Section 5.3.2. See the main text for the definition of minimal, medium and high boost.

the typical search for *pointlike* signals. Table 5.3 shows the enhancement values for integration angles of 0.1°, 0.5° and 1.0°. The corresponding analysis results are reported in Section 5.2.

5.2 H.E.S.S. observations and data analysis

The *High Energy Stereoscopic System* (H.E.S.S.) and its observation techniques are described in Chapter 3. As mentioned earlier in the present chapter, dedicated observations of NGC 1399 were carried out in autumn 2005 (Pedaletti *et al.* 2008), which were later utilized for the present analysis. The standard H.E.S.S. data quality selection (Aharonian *et al.* 2006b) was applied, and only observation runs including all four telescopes were used. After these requirements, the collected data amount to a total effective live time of 14.5 hours. The mean zenith angle of 21° provides for a low energy threshold, with $E_{\min} = 260$ GeV being the energy at which the γ-ray acceptance reaches 20% of its maximum value for the analysis of a pointlike region.

As mentioned earlier, the results presented by Abramowski *et al.* (2012, 2014) were derived using the "model" analysis procedure (de Naurois & Rolland 2009). I performed a Hillas-type analysis similar to (Aharonian *et al.* 2006b), depending on an independent calibration chain, which yielded compatible cross-check results shown below. Table 5.4 shows some of the selection cuts used in my analysis.

The largest angle of signal integration, $\vartheta_{\max} = 1.0°$, prohibited the use of the "reflected region" or "ring" background estimation techniques. Therefore, the

N_{tel}	IA	ND	MRSW (signal)	MRSW (backgr.)	$\vartheta_{\max}$ (signal)
2	80 p.e.	2.0°	0.1–1.1	1.3–2.0	0.1°, 0.5°, 1.0°

Table 5.4: Some of the event selection cuts used in the Hillas-based template analysis. Shown are the number of telescopes N_{tel} by which each event was recorded, the minimal image amplitude (IA) in photoelectrons, and the maximal nominal distance (ND) of the reconstructed shower position from the source. Also shown are the intervals in the mean reduced scaled width *parameter (MRSW) that defined the signal ("on") and background ("off") regions. See Aharonian* et al. *(2006) for the definition of these parameters. For completeness, the three signal integration angles are also mentioned.*

$\vartheta_{\max}$	N_{on}	$\overline{N_{\mathrm{off}}}$	N_γ	N_γ^{UL}	Significance
0.1°	160	122	38	71	2.3σ
0.5°	3062	2971	91	243	1.2σ
1.0°	11677	11588	89	388	0.6σ

Table 5.5: "Model" analysis results: Numbers of VHE γ-ray events from the direction of the Fornax galaxy cluster, using three different opening angles for the observation. Column 1 shows the angle $\vartheta_{\max}$, Columns 2 and 3 the numbers of γ-ray candidates in the "on" region (N_{on}) and the normalized *number of γ-rays in the "off" region ($\overline{N_{off}}$), respectively. Column 4 shows the resulting number of excess events N_γ, and Column 5 gives the 95% C.L. upper limit on the number of events according to Feldman & Cousins (1998). The significance of the numbers of γ-ray excess events is stated in Column 6, according to Equation 17 of Li & Ma (1983).* ***These are the results that were used for the calculation of upper limits shown in Section 5.3.2 and in the H.E.S.S. publication by Abramowski et al. (2012, 2014).***

"template" method was employed (see Rowell 2003 and Section 3.3.1). For the smaller signal angles, the reflected region method was used to provide a successful cross-check of the template-based results.

No significant VHE γ-ray signal was detected for any of the three different opening angles of signal integration $\vartheta_{\max}$. Hence, upper limits at 95 % confidence level (C.L.) were computed for the *total* number of γ-ray events, see Tables 5.5 and 5.6. Limits were also derived on the number of events above $E_{\min}$, see Table 5.7.

Within the *model* analysis framework, the number of background events in the signal sample was estimated by a "skymap" correction of the background sample: The ratio of the detector acceptances between "γ-like" and "hadron-like" events was determined as a (binwise) function of the shower direction, and this correction was then applied to the background sample. Therefore, no *global* on-off normalization factor α was derived, and the Tables 5.5 and 5.7 show the acceptance-corrected number of "off"-events $\overline{N_{\mathrm{off}}}$. Hence, the background normalization factor as defined by Li & Ma (1983) is exactly $\alpha = 1$. This procedure overestimates the statistical uncertainty on the background estimation, thus making the resulting upper limits somewhat conservative[4]. This is not the case in the Hillas analysis, where an averaged α value was determined, see Table 5.6. As Tables 5.5 and 5.6 show, no significant excess was measured for any of the considered signal regions.

The left panel of Figure 5.6 shows a skymap of the central region of Fornax, with the colour scale corresponding to the local significance (Li & Ma 1983, Equation 17) of the γ-ray signal as determined with the model analysis. The white circle shows an 0.1° region around the centre of NGC 1399. The right panel shows the distribution of these significances, which is well approximated by a normal Gaussian, indicating that there is no significant pointlike excess over the examined

[4] Assuming $\alpha = 0.1$ and a corresponding number of "off" events would produce upper limits N_γ^{UL} which are up to 20% lower than for $\alpha = 1$.

$\vartheta_{\max}$	BET	N_{on}	N_{off}	α	N_γ	N_γ^{UL}	Significance
0.1°	RR	292	3229	0.09	-1.5	33.5	-0.1σ
0.5°	RR	7193	25162	0.29	-96.0	106.5	-1.0σ
0.5°	T	7216	61201	0.12	24.9	200.8	0.1σ
1.0°	T	26658	222543	0.12	144.0	480.0	1.0σ

Table 5.6: "Hillas" analysis results: Numbers of VHE γ-ray events from the direction of the Fornax galaxy cluster, using three different opening angles $\vartheta_{\max}$ as shown in Column 1. Column 2 indicates the background estimation technique (BET, see Section 3.1.1). For the angles $\vartheta_{\max} = 0.1°$ and 0.5°, the reflected region (RR) method was used here. For the larger signal angles, the template (T) method was employed, so that $\vartheta_{\max} = 0.5°$ was covered by both techniques. Columns 2 and 3 show the numbers of γ-ray candidates in the "on" and "off" regions, respectively. With the on/off normalization factor α given in Column 4, the resulting number of excess events N_γ is shown in Column 5. Column 6 gives the 95% C.L. upper limit on the number of events according to Feldman & Cousins (1998). As in Table 5.5, the last column shows the corresponding significance. ***These are the cross-check results I produced using the Hillas-type analysis.*** *(The slight N_{on} discrepancy in the two 0.5° analyses stems from a difference in the angular binning method.)*

region. The same is true for the Hillas-based analysis, whose results are shown in Figure 5.7.

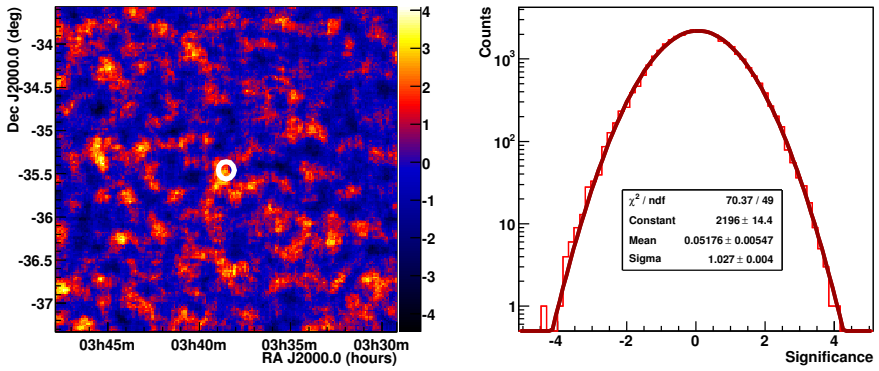

Figure 5.6: Results of the "model" analysis. Left: Significance map in equatorial coordinates, calculated according to Equation 17 of Li & Ma (1983). The map is oversampled with a top-hat function of radius 0.1°*. The white circle denotes the* 0.1° *integration region, and the colour scale shows the local significance.*
Right: Distribution of the significances over the skymap. The solid line is a Gaussian fitted to the data. One can see that the significance distribution is well approximated by a Normal distribution with mean ≈ 0 *and standard deviation* ≈ 1.

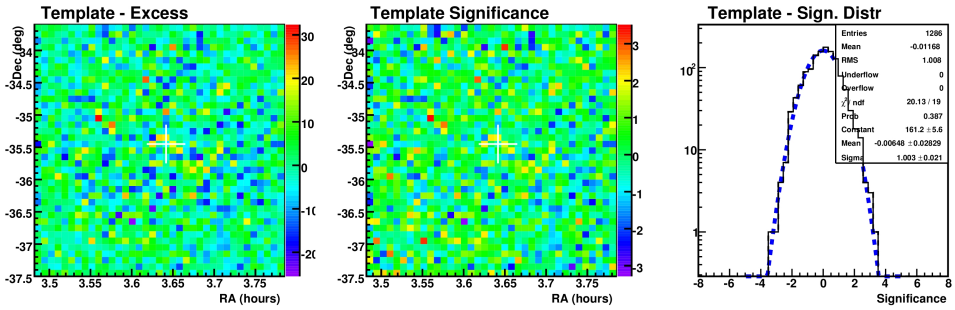

Figure 5.7: Results of the "Hillas" analysis. The left and middle panels show skymaps of the number of excess events and the corresponding significance, respectively. (In contrast to Figure 5.6, these skymaps are not *oversampled.) The right panel shows the distribution of significances over the skymap. Again, it is well described by a (0,1) normal distribution, with no indication for an excess of positive significances.*

In addition to the event numbers and the observation time T_{obs}, the effective detection area $A_{\mathrm{eff}}(E)$ of the telescope system is needed to calculate limits on the possible parameters of dark matter annihilations (cf. Section 5.3.2). Figure 5.8 shows the effective area corresponding to the Fornax observations. It was derived from Monte Carlo simulations corresponding to the zenith angles of the observation runs and then averaged over the whole data set. This effective area was computed in the "model" analysis and used for the calculation of dark matter limits in the following section. (In Figure 5.8 and for the integrations in Section 5.3, $A_{\mathrm{eff}}(E)$ was interpolated between the energy bins of the Monte Carlo simulation. See also Section 4.2.2.)

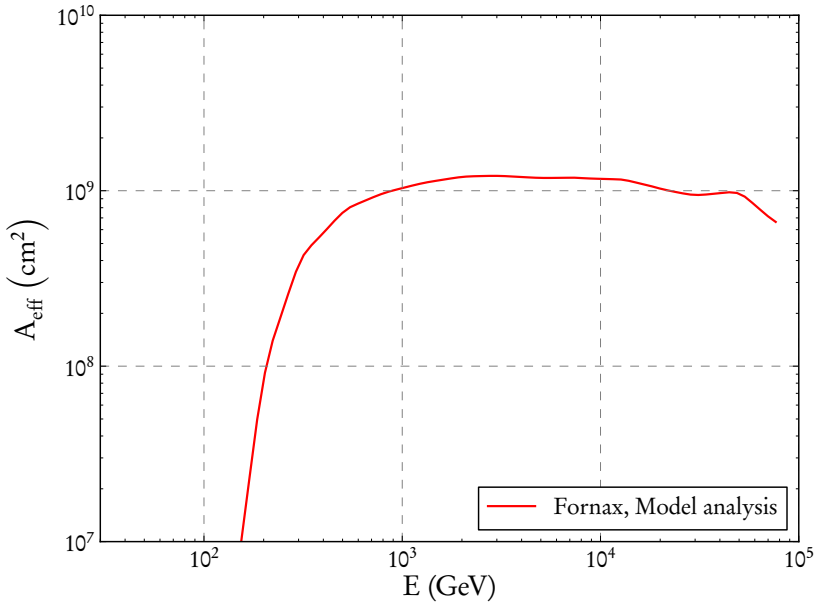

Figure 5.8: The effective detection area for the H.E.S.S. observations of the Fornax cluster of galaxies. Shown is $A_{\mathrm{eff}}(E)$ as gained from Monte Carlo simulations, averaged over the corresponding zenith angles of the observation runs. This is the effective area resulting from the "model" analysis.

5.3 Interpretation of the results

The results of the H.E.S.S. observations of the Fornax cluster were interpreted in two separate steps: First, limits on the number of γ-ray events above the energy threshold were converted into limits on the integral γ-ray flux from Fornax. Second, limits on the *total* number of detected γ-ray events were translated into limits on the annihilation cross-section of dark matter, using the halo parameters derived in the previous section and several different models of particle dark matter.

5.3.1 Upper limits on the integrated γ-ray flux from Fornax

The basic definition of the integrated γ-ray flux Φ_γ is the number of events N_γ that fall onto a given area A within a time T, i.e. $\Phi_\gamma = N_\gamma/(A \times T)$. However, it has to be taken into account that the effective detection area $A_{\rm eff}$ of Cherenkov telescopes is a function of the γ-ray energy, and that the γ-rays follow a differential energy spectrum $\mathrm{d}N_\gamma/\mathrm{d}E_\gamma$. Integrating over the product of these two and normalizing by the integrated spectrum yields an "averaged" effective area:

$$\langle A_{\rm eff} \rangle = \frac{\int_{E_{\rm th}}^{\infty} \mathrm{d}E_\gamma \, A_{\rm eff}\left(E_\gamma\right) \frac{\mathrm{d}N_\gamma}{\mathrm{d}E_\gamma}\left(E_\gamma\right)}{\int_{E_{\rm th}}^{\infty} \mathrm{d}E_\gamma \frac{\mathrm{d}N_\gamma}{\mathrm{d}E_\gamma}\left(E_\gamma\right)} \,. \tag{5.9}$$

Equation 5.9 makes two things visible: First, the γ-ray spectrum $\mathrm{d}N_\gamma/\mathrm{d}E_\gamma$ has to be known (or specified) *a priori* in order to compute this average. Secondly, if the spectrum diverges for $E_\gamma \to 0$, a lower energy threshold $E_{\rm th}$ may have to be defined, in order to make the integral in the denominator finite.

As an illustration, Figure 5.9 shows the integrand $A_{\rm eff} \times \mathrm{d}N_\gamma/\mathrm{d}E_\gamma$ for the γ-ray spectrum from dark matter annihilations to $b\overline{b}$ pairs (see the discussion and Figure 5.11 below). Here, a DM particle mass $m_\chi = 10$ TeV is assumed, effectively cutting off the integration at this γ-ray energy.

Using $\langle A_{\rm eff} \rangle$ and an upper limit on the event number $N_\gamma^{\rm UL}$, the corresponding limit on the γ-ray flux above the energy threshold can be derived as follows:

$$\Phi_\gamma^{\rm UL}\left(E_\gamma > E_{\rm th}\right) = \frac{N_\gamma^{\rm UL}\left(E_\gamma > E_{\rm th}\right) \int_{E_{\rm th}}^{\infty} \mathrm{d}E_\gamma \frac{\mathrm{d}N_\gamma}{\mathrm{d}E_\gamma}\left(E_\gamma\right)}{T_{\rm obs} \int_{E_{\rm th}}^{\infty} \mathrm{d}E_\gamma \, A_{\rm eff}\left(E_\gamma\right) \frac{\mathrm{d}N_\gamma}{\mathrm{d}E_\gamma}\left(E_\gamma\right)} \,. \tag{5.10}$$

Table 5.7 shows upper limits on the number of γ-ray events above the threshold energy $E_{\rm min} = 260$ GeV for the three different angles of signal integration. In addition, it shows upper limits on the γ-ray flux, computed for power-law spectra of the form $\mathrm{d}N_\gamma/\mathrm{d}E = \Phi_0 \times (E/E_0)^{-\Gamma}$ and the two indices $\Gamma = 1.5,\ 2.5$. These values were chosen because the spectra of standard astrophysical VHE γ-ray sources often follow power laws of index $\Gamma \sim 2$ to 3 (Hinton & Hofmann 2009), while the photon spectra from dark matter annihilations may be steeper, with $\Gamma \sim 1.5$ (e.g. Bergström *et al.* 1998; Bovy 2009).

Another possible approach is to compute the γ-ray flux limit under the assumption of an energy spectrum that is determined by a particular model of particle dark matter. For instance, dark matter annihilations to different final states produce distinctly different γ-ray spectra, see Section 2.3.1 and Figure 4.3.

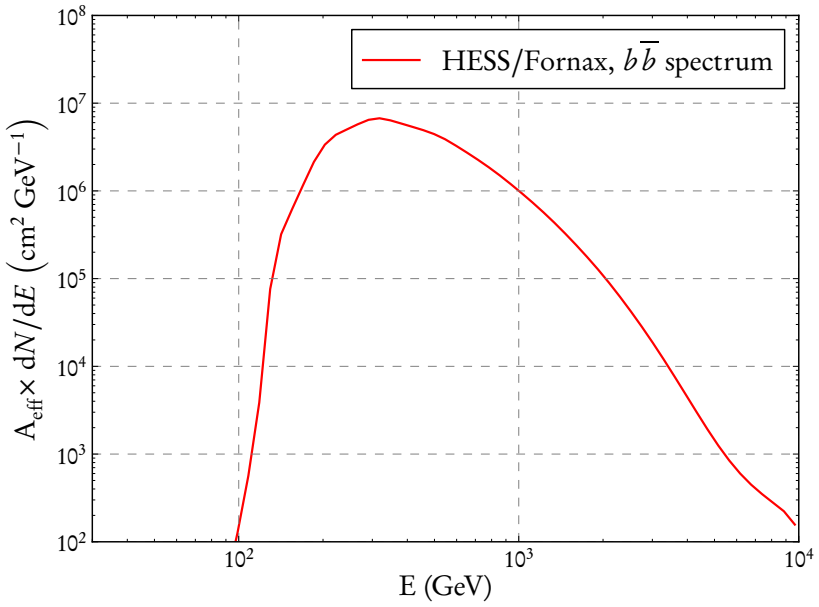

Figure 5.9: The product of effective area A_{eff} and γ-ray spectrum $\mathrm{d}N_\gamma/\mathrm{d}E_\gamma$, for the photon spectrum from dark matter annihilations to $b\bar{b}$ pairs and a DM particle mass $m_\chi = 10$ TeV. The corresponding effective area is shown in Figure 5.8, and the γ-ray spectrum is shown in Figure 5.11.

These can be inserted into Equation 5.10, effectively cutting off the integrations at $E_\gamma = m_\chi$. Note, however, that no corresponding high-energy cut is applied to the γ-ray event sample. Nevertheless, the γ-ray flux limits become a function of the dark matter mass m_χ, as is shown in Figure 5.10 for annihilations into $b\bar{b}$, W^+W^- and $\tau\bar{\tau}$ pairs. Here, the γ-ray spectrum parametrizations of Cembranos *et al.* (2011) were used, which are shown in Figure 5.11. (The photon spectra computed by Cirelli *et al.* (2011) were used for the Fornax publication by Abramowski *et al.* 2012, 2014.)

Note that for the dark matter flux limits (Figure 5.10), an averaged effective area was used, while for the power-law spectra (Table 5.7), a slightly more sophisticated algorithm was available which allowed to consider the zenith-angle dependence of $A_{\mathrm{eff}}(E)$ for each observation run.

5.3.2 Upper limits on the dark matter annihilation cross-section

The prediction for the γ-ray flux from dark matter annihilations, Equation 2.19, can be inverted in order to draw conclusions about the DM model parameters from a γ-ray observation: Assuming that the halo factor $\bar{J}$ is fixed and that the γ-ray spectrum $\mathrm{d}N_\gamma/\mathrm{d}E_\gamma$ is specified by the dark matter model, an upper limit on

$\vartheta_{\max}$	$N_\gamma^{\mathrm{UL}}(E_\gamma > E_{\min})$	$\Phi^{\mathrm{UL}}_{E_\gamma > E_{\min}}\left(10^{-12}\,\mathrm{cm}^{-2}\mathrm{s}^{-1}\right)$	
		$\Gamma = 1.5$	$\Gamma = 2.5$
0.1°	41.3	0.8	1.0
0.5°	135.1	2.3	3.3
1.0°	403.5	6.8	10.0

Table 5.7: Upper limits on the VHE γ-ray flux from the direction of Fornax, assuming a power-law spectrum with index $\Gamma = 1.5$ or 2.5. Column 1 shows the opening angle of the integration region, Column 2 the upper limits on the number of observed γ-rays above the minimum energy $E_{\min} = 260$ GeV, calculated at 95% confidence level. Columns 3 and 4 list the 95% C.L. limits on the integrated flux limits above the minimum energy. They were computed for the two power-law indices according to Equation 5.10.

the number of γ-ray events N_γ^{UL} can be translated into a limit on the annihilation cross-section $\langle\sigma v\rangle$ as a function of the DM mass m_χ:

$$\langle\sigma v\rangle_{\mathrm{UL}}\left(m_\chi\right) = \frac{8\pi}{T_{\mathrm{obs}}}\frac{m_\chi^2}{\bar{J}(\Delta\Omega)\Delta\Omega}\frac{N_\gamma^{\mathrm{UL}}}{\displaystyle\int_0^{m_\chi} \mathrm{d}E_\gamma\, A_{\mathrm{eff}}(E_\gamma)\frac{\mathrm{d}N_\gamma(E_\gamma)}{\mathrm{d}E_\gamma}}\,. \tag{5.11}$$

The remaining parameters are the observation time T_{obs} and the effective detection area A_{eff}.

In the analysis presented here, no lower energy cutoff was imposed on the γ-ray event sample, so that the integration in Equation 5.11 starts at $E_\gamma = 0$. However, there is the energy threshold induced by the effective area $A_{\mathrm{eff}}\left(E_\gamma\right)$, see Figure 5.9.

No particular models of particle dark matter (cf. Section 2.2) were chosen for the analysis presented here. Instead, a set of annihilation final states were considered that produce distinct γ-ray spectra, which should encompass a wide range of cold dark matter models with masses in the TeV range. These final states are:

a) pairs of b quarks: $b\overline{b}$

b) pairs of W bosons: W^+W^-

c) pairs of τ leptons: $\tau\overline{\tau}$

d) pairs of muons: $\mu\overline{\mu}$

e) W^+W^- bosons, including photons from internal bremsstrahlung.

The photon spectrum parametrizations for annihilations to $b\overline{b}$, W^+W^- and $\tau\overline{\tau}$ pairs were published by Cembranos *et al.* (2011). As mentioned before, this is

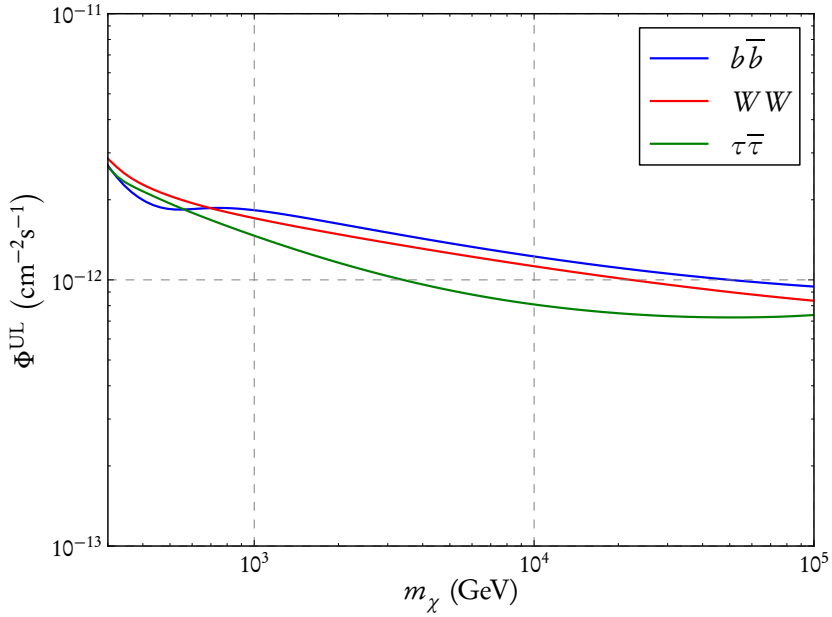

Figure 5.10: Upper limits at 95% C.L. on the γ-ray flux above $E_{\mathrm{min}} = 260\,\mathrm{GeV}$ from dark matter self-annihilations into different final states, as a function of the DM mass m_χ. These limits are calculated from the number of γ-ray events above E_{min} as shown in Table 5.7. The integration angle $\vartheta_{\mathrm{max}} = 0.1°$ was used.

in contrast to the Fornax publication by Abramowski *et al.* (2012, 2014), where the results by Cirelli *et al.* (2011) were used. See Cembranos *et al.* (2013) for an assessment of the considerable uncertainties related to Monte Carlo QCD event generators, which are commonly used for the computation of γ-ray spectra from the fragmentation and hadronization of DM annihilation final states.

The annihilation to muon pairs is an example of the class of "leptophilic" dark matter models (see, for example, Bergström *et al.* (2009) or Meade *et al.* 2010), which were designed to explain the rise in the CR positron fraction that was measured by the *PAMELA* satellite (Adriani *et al.* 2009). The γ-ray spectrum used here is that of final state photon radiation, for which a parametrization was provided by Bovy (2009), Equation 11.

The last point in the list above refers to the electromagnetic correction to the photon spectrum put forward by Bergström (1989), Bergström *et al.* (2005) and Bringmann *et al.* (2008) for the case of supersymmetric dark matter. Since Bringmann *et al.* (2008) showed that this effect can arise in the annihilation of dark matter to W bosons, their approximation (Equation 3.7) is used here as an additional contribution to the γ-ray spectrum from W boson fragmentation. Note that this approximation is only valid for small mass differences between the wino as dark matter particle and the next-to-lightest supersymmetric particle, i.e. a chargino here. (See also Section 2.2.3.)

The abbreviation IB for internal bremsstrahlung denotes this feature. Strictly speaking, IB refers to two different effects, namely *virtual internal bremsstrahlung* (VIB) from charged virtual particles in the annihilation process, and final state radiation (FSR) from the external "legs" of the corresponding Feynman diagrams. Bringmann *et al.* (2008) note that the expected FSR is relatively small for the wino case considered here, which instead features large VIB contributions. Hence, the double-counting of FSR photons induced by simply adding the IB parametrization to the γ-ray spectrum (which already contains FSR photons) should not have a large effect.

Electro*weak* corrections, as computed by Ciafaloni *et al.* (2011), Bell *et al.* (2011) or Bringmann & Calore (2014), are not considered here. While Bringmann & Calore (2014) state that these corrections may produce a "very sizeable" enhancement even in the VHE regime, they influence mainly the γ-ray yield at low energies ($E_\gamma < 0.1 m_\chi$). In addition, these corrections are strongly model-dependent, requiring e.g. the particular SUSY particle spectrum to be calculated. Such computations were beyond the scope of this work.

Figure 5.11 shows the γ-ray spectra from annihilations to these different final states for a dark matter particle of mass $m_\chi = 1$ TeV, weighted with E_γ^2.

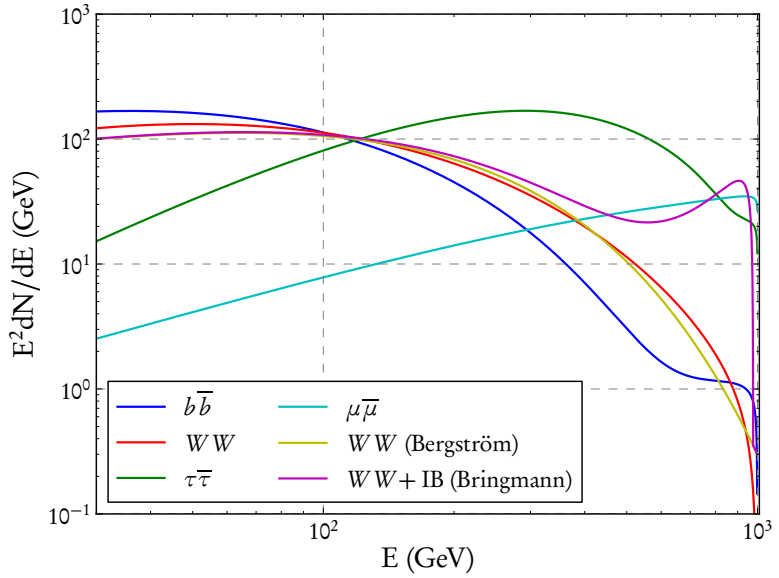

Figure 5.11: VHE γ-ray spectra from the annihilation of $m_\chi = 1$ TeV dark matter particles. See the main text for an explanation of the different models shown here. Note that the spectra $\mathrm{d}N/\mathrm{d}E$ are weighted with the factor E^2; similar, but unweighted spectra are shown in Figure 4.3. "Bergström" refers to the popular spectrum parametrization by Bergström et al. (1998), which is shown here for comparison.

Figure 5.12 shows upper limits on the dark matter self-annihilation cross-section $\langle\sigma v\rangle_{\mathrm{UL}}$ for these different dark matter models, computed according to Equation 5.11. For these limits, the integration angle $\vartheta_{\mathrm{max}} = 0.1°$ was used, with the corresponding $\bar{J}$ factor from the Fornax halo model SR10 a_{10} (Table 5.2) and not considering any substructure boosts. The limit on the number of γ-ray events is $N_{\gamma}^{\mathrm{UL}} = 71$, cf. Table 5.5.

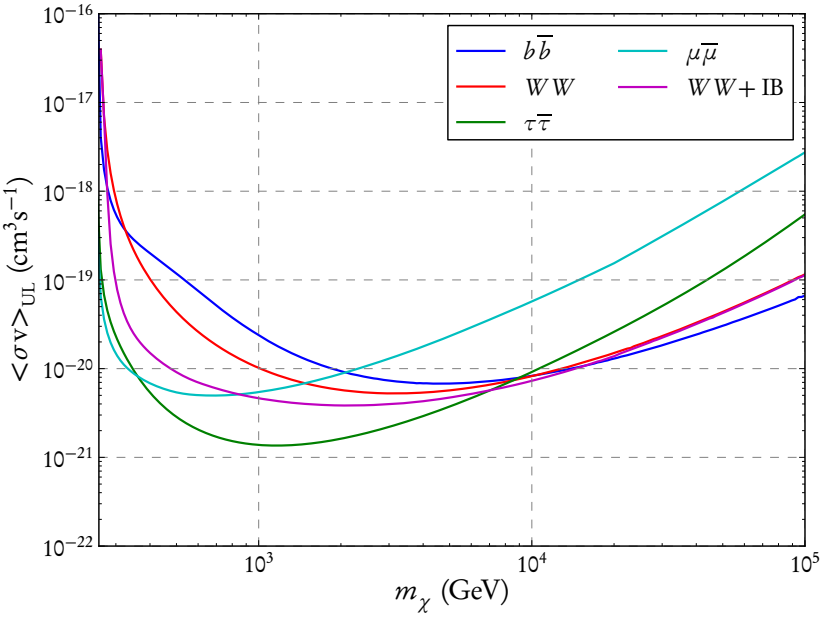

Figure 5.12: Upper limits at 95% C.L. on the annihilation cross-section $\langle\sigma v\rangle$, as a function of the dark matter particle mass m_{χ}. Colours indicate the different final states as explained in the main text. The integration angle $\vartheta_{\mathrm{max}} = 0.1°$ was used for these limits, together with the corresponding $\bar{J}$ factor from the Fornax halo model SR10 a_{10} and no substructure boost. See Tables 5.2 and 5.5 for the $\bar{J}$ value and N_{γ}^{UL}, respectively.

The effect of assuming *other* halo models is explored in Figure 5.13. Since the halo factor $\overline{J}$ is a simple divisive factor in Equation 5.11, this is equivalent to a trivial rescaling of the corresponding cross-section limits. Again, $\vartheta_{\mathrm{max}} = 0.1°$ is used here. The models a_{10} and $\mathrm{a}_{10,b}$ have the same numerical $\overline{J}$ value (within the rounding uncertainty), therefore only the first is shown in the plot. Here, annihilation to $b\overline{b}$ pairs is assumed.

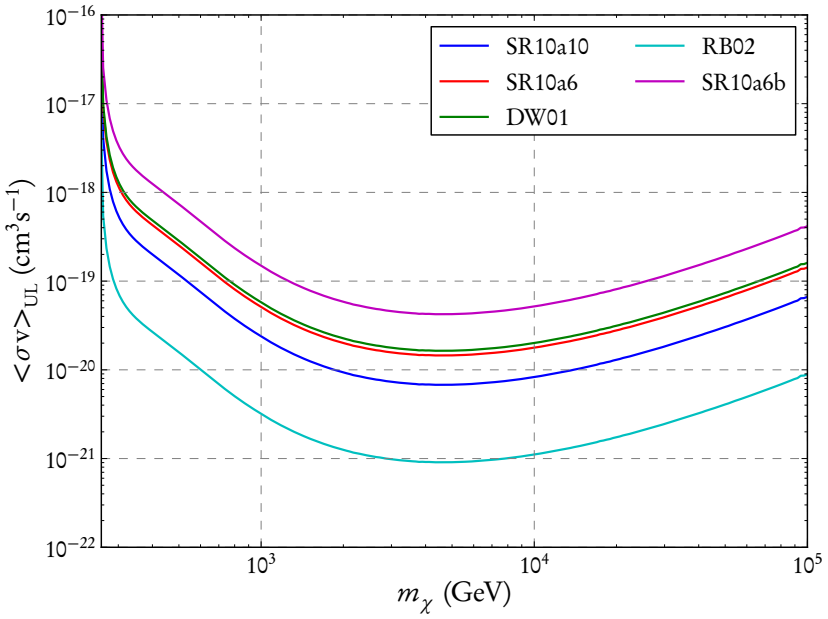

Figure 5.13: 95% C.L. upper limits on $\langle\sigma v\rangle$ for different Fornax halo profiles and $\vartheta_{\mathrm{max}} = 0.1°$. The abbreviations in the legend are explained in Section 5.1.1 and the corresponding $\overline{J}$ values are shown in Table 5.2. The substructure boost, which would be different for the different haloes, was not considered here. Dark matter annihilation to $b\overline{b}$ pairs was assumed.

Finally, the effect of flux enhancements due to substructure of the dark matter halo was tested. Figure 5.14 shows the limits derived for all three different integration angles, i.e. $\vartheta_{\mathrm{max}} = 0.1°$, 0.5° and 1.0°, and assuming no boost at all (Table 5.2) or the "medium" and "high" boost factors listed in Table 5.3. The enhancement was computed for the dark matter halo SR10 a_{10}. The different limits on the number of γ-ray events are shown in Table 5.5. Again, the cross-section limits are computed for annihilation to $b\bar{b}$ final states.

This figure shows how dark matter substructure effects, if real, may boost the cross-section limits (or detection prospects) by orders of magnitude. It also illustrates how such substructures would change the "appearance" of the Fornax cluster in γ-rays, making it brighter at large radial distances. Hence, observations of large solid angles become more sensitive than "point-like" analyses. Nevertheless, it has to be kept in mind that the magnitude of this enhancement is subject to sizable uncertainties.

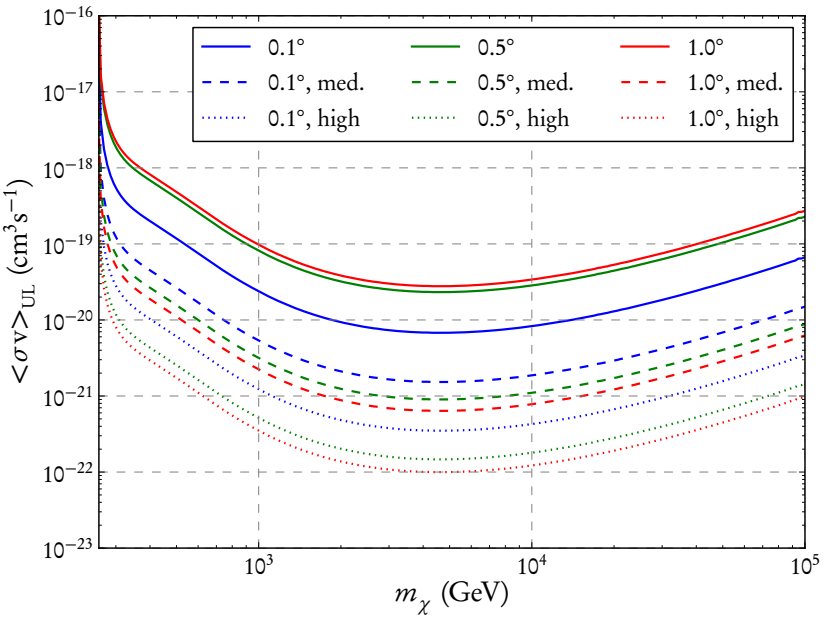

Figure 5.14: 95% C.L. upper limits on $\langle\sigma v\rangle$ for different integration angles and dark matter substructure boosts. Annihilation to $b\bar{b}$ pairs and the halo model SR10 a_{10} were assumed. Solid lines show the limits with no substructure enhancement, dashed lines show the limits for medium *boosts and dotted lines show the limits for* high *boosts. Colours indicate the integration angles ϑ_{max}. This figure illustrates the interplay of the different $\bar{J}$ values (see Table 5.2), substructure boosts (Table 5.3) and event number limits (Table 5.5).*

5.3.3 The Sommerfeld effect and wino dark matter

The PAMELA measurements mentioned above provoked many interpretations in terms of particle dark matter models. Broadly speaking, these needed to fulfill two criteria: The annihilation to hadronic particles had to be suppressed in order to not overproduce cosmic ray antiprotons, hence the "leptophilic" models, and the annihilation cross-section needed to be higher than the naive expectation of its "thermal" value, $\langle \sigma v \rangle_0 = 3 \times 10^{-26}$ cm^{3}s^{-1} (see Chapter 2).

One mechanism invoked to provide this boost is the *Sommerfeld effect*, named after its first description in the realm of electron scattering (Sommerfeld 1931). It is a velocity-dependent, non-perturbative quantum-mechanical effect which occurs in scattering processes: If the relative velocity of two scattering particles is sufficiently low, the probability of the reaction can be enhanced by multiple exchange of the force carrier bosons.

In terms of dark matter physics, this corresponds to a boosted effective annihilation cross-section *today*, compared to its value during thermal freeze-out, when the relative velocities of DM particles were higher. This can be expressed by the (velocity-dependent) boost factor S:

$$\langle \sigma v \rangle_{\mathrm{eff}} = S \times \langle \sigma v \rangle_0 \,. \tag{5.12}$$

Hisano *et al.* (2004) showed that this can be the case for wino dark matter (cf. Moroi & Randall 2000), which annihilates to W bosons via the electroweak force. Later, Arkani-Hamed *et al.* (2009) and other authors (see Feng *et al.* 2010 and references therein) realized that non-standard model force carrier particles ϕ which are sufficiently light (e.g., $m_\phi \sim 250$ MeV) could provide both the necessary annihilation boost *and* a kinematic preference for dark matter annihilations to leptons.

Here, however, the Sommerfeld effect from the *weak* interaction is explored, following Lattanzi & Silk (2009). These authors computed the boost resulting from multiple exchange of Z bosons for different relative velocities $\beta = v_{\mathrm{rel}}/c$ and dark matter particle masses above 1 TeV. Apart from the velocity dependence, they found resonant features appearing for particular DM masses, corresponding to quasi-bound states during the annihilation process. These resonances occur in any type of Sommerfeld enhancement, depending on the interplay of coupling strength, force carrier mass and dark matter particle mass. However, for dark matter particles annihilating via Z exchange, $\alpha_{\mathrm{weak}} \sim 0.3$ and $m_Z \sim 90$ GeV are given. This fixes the DM masses for which resonant annihilation would occur.

Under the assumption that this holds true for wino dark matter annihilating to W bosons[5], the Sommerfeld boost was included in the calculation of a limit to the high-β cross-section $\langle \sigma v \rangle_0$, shown in Figure 5.15. The velocity dispersion of stars and globular clusters around NGC 1399 is of the order of a few hundred km s^{-1} (Schuberth *et al.* 2010), and the same may be assumed for the mean relative

[5] see also Hryczuk & Iengo (2012)

velocity of dark matter particles, so that $\beta \approx 10^{-3}$ and the corresponding boost was applied.

Since this was intended to be the most stringent (hence least conservative) limit on $\langle \sigma v \rangle$ that could be derived within the modelling assumptions, the $\bar{J}$ factor was calculated for the integration angle $\vartheta_{\mathrm{max}} = 1.0°$ and a high substructure boost from the halo model SR10 a_{10}. (Using the model RB02 would result in an additional boost factor ~ 10.) The W^+W^- photon spectrum including internal bremsstrahlung was assumed.

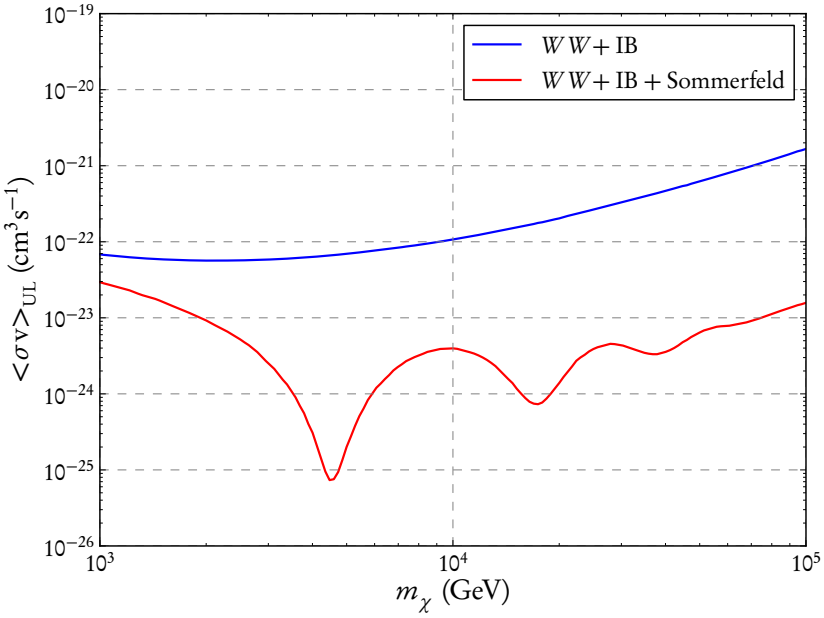

Figure 5.15: Upper limits on the dark matter annihilation cross-section during thermal freeze-out $\langle \sigma v \rangle_0$, i.e. in the limit of high relative velocity of the annihilating particles. The limits at 95% C.L. are calculated for annihilation to W^+W^- pairs, including internal bremsstrahlung, and for a dark matter halo of type SR10 a_{10} with high substructure boost (cf. Section 5.1.2). The integration angle $\vartheta_{\mathrm{max}} = 1.0°$ was used. The red line is derived under the assumption of a Sommerfeld boost $S = \langle \sigma v \rangle_{\mathrm{eff}} / \langle \sigma v \rangle_0$ as derived for $\beta = 10^{-3}$ by Lattanzi & Silk (2009), while the blue line shows the limit without this boost.

Figure 5.15 shows that under these assumptions, which provide for boosts up to several orders of magnitude, the 95% C.L. upper limits on the annihilation cross-section almost reach its predicted value during thermal freeze-out, i.e. $\langle \sigma v \rangle_0 = 3 \times 10^{-26}$ cm^{3}s^{-1}.

5.4 Summary and conclusions

In this chapter, observations of the Fornax cluster of galaxies with the H.E.S.S. telescopes were used to derive bounds on a possible signal from dark matter self-

annihilations. In Section 5.1, several mass profiles of Fornax and its central galaxy NGC 1399 were collected from published literature. From these halo profiles, the corresponding $\bar{J}$ factors were derived, which are necessary ingredients for the computation of the expected DM signal (Table 5.2). In addition, the signal boost from DM substructures was calculated for different limiting subhalo masses (Section 5.1.2, Table 5.3), following Springel *et al.* (2008b) and Pinzke *et al.* (2009). The flux enhancement expected for large distances from the cluster centre motivated the analysis of extended signal regions, which is described in Section 5.2. Angular radii of 0.1°, 0.5° and 1.0° from the centre were analyzed using the "model" framework and the "template" background estimation technique. The H.E.S.S. observations amount to a live time of 14.5 hours, at a mean zenith angle of 21°.

As no significant γ-ray signal was detected (Table 5.5), upper limits on the integrated γ-ray flux were derived for power-law and DM annihilation spectra (Section 5.3.1). The 95% C.L. limits above the minimal energy $E_{\mathrm{min}} = 260\,\mathrm{GeV}$ range from 0.8 to 10.0×10^{-12} $\mathrm{cm}^{-2}\mathrm{s}^{-1}$, depending on the spectrum and the integration angle.

Finally, upper limits on the thermally averaged dark matter self-annihilation cross-section $\langle \sigma v \rangle$ were calculated, again at 95% confidence level (Section 5.3.2). Annihilation to several different final states was considered, corresponding to γ-ray spectra of different shapes (Figure 5.11). The effect of including virtual internal bremsstrahlung was also computed, Figure 5.12 shows the resulting limits. Figures 5.13 and 5.14 show how the upper limit on $\langle \sigma v \rangle$ changes under the assumptions of different halo models and substructure boosts, respectively. Finally, the Sommerfeld effect for wino-like dark matter was explored in Section 5.3.3.

Except in the case of a Sommerfeld boost, the upper limits on the annihilation cross-section reach their lowest levels at about 10^{-19} to 10^{-22} $\mathrm{cm}^3\mathrm{s}^{-1}$. Due to the interplay of the H.E.S.S. energy threshold and the expected γ-ray signal, the lowest limits are found for dark matter particle masses above 1 TeV.

The large spread in the upper limits reflects the uncertainty on the dark matter halo profile of the Fornax galaxy cluster. On top of this, the possible signal enhancement by dark matter substructures introduces another large factor of uncertainty. The work presented in this chapter quantified how these uncertainties affect the constraints on self-annihilating WIMP dark matter that can be derived from the H.E.S.S. observations of the Fornax cluster.

An outlook at possible further studies along these lines can be found in Chapter 6. In addition, it should be noted that the observations presented here have already been used to constrain models of *decaying* dark matter (Cirelli *et al.* 2012). Here, the expected signal scales with the DM *mass density* along the line-of-sight, instead of the squared density. Therefore, the large mass of galaxy clusters provides an advantage over dwarf galaxy observations, despite their larger distance (see also Dugger *et al.* 2010).

Chapter 6

Summary and outlook

6.1 Results and conclusions

This thesis presented searches for very high energy γ-ray signals from WIMP dark matter self-annihilations in astronomical entities of quite different scales: Dwarf spheroidal galaxies, as presented in Chapter 4, form the *smallest* dark matter-dominated galactic objects observed so far. Galaxy clusters, on the other hand, are the *largest* objects found in a gravitationally relaxed state, even though the Fornax cluster considered in Chapter 5 is a rather lightweight example of its class. As no significant γ-ray signal was found from either type of target, the observations were used to place upper limits on the velocity-averaged dark matter self-annihilation cross-section $\langle \sigma v \rangle$ for dark matter particle masses m_χ in the range between 100 GeV and 100 TeV.

Chapter 4 presented a novel technique of combining published results from dark matter searches with imaging air Cherenkov telescopes. For the first time, observations of different dwarf spheroidals taken with different telescope systems were combined in a statistically consistent way. In addition, the observational uncertainties relating to the halo factor, or "J factor", of each object could be taken into account. Upper limits on the DM self-annihilation cross-section were computed at a confidence level of 95%, *including* the expected error on J. Limits were derived both from the single observations of dwarf galaxies and from their combination. The *combined likelihood stacking* method was shown to be powerful, even though it became apparent that its results can be rather strongly affected by the properties of *single* data sets. A more detailed summary and conclusions can be found in Section 4.4.

Chapter 5, on the other hand, presented observations of a single target, the Fornax cluster of galaxies, taken with the H.E.S.S. telescopes. A number of different mass profile determinations from the literature were used to compute the $\bar{J}$ factor. In addition, the possible flux enhancement from dark matter substructures was calculated, which is particularly important at larger distances from the cluster centre. This motivated the analysis of extended signal regions, with an angular

radius up to $\vartheta_{\mathrm{max}} = 1.0°$. As in the case of the dwarf galaxy analysis, no significant γ-ray excess was found, and upper limits on the dark matter self-annihilation cross-section were derived for different annihilation channels. Again, a more detailed summary can be found in Section 5.4.

Both the dwarf and the cluster analyses depend strongly on the properties of dark matter haloes on sub-galactic scales. Hence, a significant part of this thesis was devoted to the quantification of the considerable uncertainties stemming from these imperfectly known "small-scale" DM features (see Section 2.1.5). In fact, systematic uncertainties about the halo factor affect very many indirect dark matter searches in γ-rays, but not always are they acknowledged as such. The J probability density functions used in Chapter 4 quantify these "known unknowns", but even they may be affected by systematic biases induced by the determination of the PDFs. The different sets of halo parameters collected in Section 5.1.1 for the central part of the Fornax galaxy cluster may serve as a warning: Even under the assumption of an NFW-type dark matter halo, the best-fitting profile parameters vary by large factors, depending on the method of measurement.

The observations of dwarf spheroidals as well as those of the Fornax galaxy cluster have yielded limits on the dark matter annihilation cross-section which lie, neglecting "special effects" like the Sommerfeld boost, orders of magnitude above the value $\langle \sigma v \rangle_0 = 3 \times 10^{-26}\ \mathrm{cm^3 s^{-1}}$ expected from thermal WIMP freeze-out. Generally, dark matter searches with Cherenkov telescopes suffer from their relatively high energy threshold, especially when compared to *Fermi*-LAT results. In fact, considering dark matter particle masses below ~ 1 TeV, only two IACT observations (Abramowski *et al.* 2011b; Aleksić *et al.* 2014) have produced limits which are comparable in strength to those from *Fermi*-LAT dwarf observations. The Milky Way halo, as shown by the H.E.S.S. result, seems to be the most promising observational target for a possible detection of dark matter signals. However, at energies below ~ 100 GeV, which are accessible with *Fermi*-LAT or H.E.S.S. II, the Galactic centre region is a very "crowded" part of the sky. There is a strong astrophysical γ-ray background signal, which has an irregular spatial distribution that is not easily modelled. Thus, it is rather difficult to identify a dark matter signal within the γ-ray flux from the Galactic centre. Observations of extragalactic sources like dwarf spheroidals and galaxy clusters may provide necessary and insightful cross-checks to those of the Milky Way, also in the future.

6.2 Future directions

As dark matter is such a mysterious and intriguing phenomenon, the efforts to detect its signals in a laboratory or in the sky are bound to continue. In particular, progress in γ-ray searches can be expected to develop along the following lines:

6.2.1 Improved constraints on the small-scale properties of dark matter haloes

These may come from more extensive observations, e.g. completing the satellite inventory of the Milky Way (e.g. Belokurov *et al.* 2014), improving kinematic constraints (e.g. Battaglia *et al.* 2013, Section 4) and exploring the dwarf populations of external galaxies (e.g. Miller *et al.* 2014). The dark matter content of dwarf galaxies may also be better understood by improved numerical simulations, see Pontzen & Governato (2014) for a recent review and Sections 2.1.4, 2.1.5 for further references. Studying the internal structure of these "small-scale" dark matter haloes, their population functions and their interaction with baryonic processes may have two important results: First, it should serve to clarify if dark matter can indeed be composed of WIMPs with masses in the GeV to TeV range. Secondly, if it is, the self-annihilation signal from dark matter (sub-) haloes can be calculated with better precision.

Certainly, these studies will be helpful for the interpretation of dwarf galaxy observations in γ-rays. If future constraints on their DM haloes are translated into computations of the corresponding $\bar{J}$ factors, preferably with PDFs parametrizing the uncertainties, these results could be directly included in the likelihood formalism introduced in Chapter 4. Obviously, this also applies to eventual observations of newly found dwarfs.

On the other hand, the discovery of a yet undetected, nearby galaxy cluster is presumably out of the question. Nevertheless, constraints on small-scale dark matter structures could help inform the interpretation of future cluster observations, so that the large uncertainties as reported in Chapter 5 would be reduced. In particular, it should be possible to compute, for each targeted cluster, the "substructure boost" from *visible* structures. These are the galaxies, of course, but also lensing and X-ray constraints could be combined to deduce the common gravitational potential of a galaxy cluster (Bartelmann *et al.* 2013). Finally, observations and simulations as presented by Aleksić *et al.* (2012a) may allow to better disentangle the γ-rays produced by *cosmic ray* interactions in clusters, if detected, from any DM-related signal.

6.2.2 Further observations and refined analyses with existing telescopes

The existing IACTs are continuously taking new data on well-known dwarf galaxies, see e.g. Lamanna *et al.* (2013) and Aleksić *et al.* (2014). Any results published in the future could be added to the likelihood combination presented in Chapter 4, if the data are presented in sufficient detail. It is important here that any J factor PDFs are provided for the angular observation scales of Cherenkov telescopes — e.g., the *Fermi*-LAT collaboration has recently published J values and uncertainties for many dwarf spheroidals, but only corresponding to the integration angle $\vartheta_{\mathrm{max}} = 0.5°$ best suiting the LAT (Ackermann *et al.* 2014).

In addition, the likelihood calculation itself could be improved. For example, the latest MAGIC observations of Segue 1, which could not yet be included in the work presented here, were interpreted using a "full likelihood method" that takes into account signal and background spectra and the instrument response function (Aleksić *et al.* 2014). The H.E.S.S. collaboration is also pursuing likelihood-based dark matter search techniques[1]. If these advanced likelihood functions were made public in the future, they might be used to replace the somewhat crude analysis of event numbers and effective areas included in the present combined likelihood method.

6.2.3 Better observatories

As mentioned in Chapter 3, the H.E.S.S. array was augmented with a very large fifth telescope, in order to reduce the energy threshold and enhance the low-energy sensitivity. Observations have begun and can be expected to provide important insights, e.g. testing the γ-ray line at about 130 GeV for which indications were found in *Fermi*-LAT data (e.g. Weniger 2012), see Bergström *et al.* (2012). *Fermi*-LAT dark matter searches will profit in the near future from improved data analysis software ("Pass 8", Atwood *et al.* 2013), which will also extend the energy range of the instrument to several hundred GeV. Succeeding *Fermi*, the GAMMA-400 satellite telescope (Moiseev *et al.* 2013) is supposed to be launched in 2019. It is planned to have a finer energy resolution than *Fermi*-LAT, which would ease the detection of spectral features.

Regarding ground-based γ-ray telescopes, the *Cherenkov Telescope Array* (CTA, Acharya *et al.* 2013) will be the next leap forward. Several features will enhance its dark matter detection capabilities, compared to present instruments:

- The energy range will be extended, which is most important at the lower end, increasing the reach for low-mass WIMPs. (This is particularly valid when compared to the four-telescope arrays of H.E.S.S. and VERITAS. The fifth telescope of H.E.S.S. phase II is in fact larger than the foreseen CTA telescopes, allowing a similar energy threshold.)
- The overall (point-source) sensitivity will be better by a factor of ten over a wide energy range. Obviously, this is helpful for a detection of the faint signals expected from dark matter annihilations.
- For a certain energy range, the field of view will be larger than those of current telescopes. This may ease the analysis of extended signal regions, e.g. for galaxy clusters or the region around the Galactic centre.
- Finally, an improved energy resolution will help to find spectral features, like annihilation lines or the DM particle mass edge.

[1] Chr. Farnier, private comm.

Galactic centre observations with CTA should allow limits on the DM annihilation cross-section that reach the "thermal" value, if no signal is found. Observations of dwarf galaxies and galaxy clusters, on the other hand, may not be so sensitive, but they are foreseen nonetheless (Doro *et al.* 2013). It should also be mentioned that CTA measurements of the *diffuse* γ-ray background will be analyzed for spectral (Bringmann *et al.* 2014) and spatial (Ripken *et al.* 2014) features that could be related to dark matter annihilations. However, such a signal would obviously lack the direct relation to a particular astronomical object, which is typically an asset of γ-ray dark matter searches. In addition, the contribution from other unresolved γ-ray sources must be estimated for these analyses, which introduces another factor of uncertainty.

Finally, the CTA will be organized as an "open observatory", with a certain amount of observation time dedicated to proposals from outside the experimental collaboration. This may provide the opportunity to extract and publish observational parameters in more detail than provided by present-day collaborations; for example, observational data might be analyzed in the form of likelihood functions, as it is already possible with the "*Fermi* Science Tools"[2].

If no γ-ray signal from DM annihilations is found with CTA, only a dedicated instrument like the *Dark Matter Array* proposed by Bergström *et al.* (2011) may provide help. In addition, this would definitely extend the reach of dark matter searches to regions in parameter space that are not easily, or not at all, accessible with collider-based or direct detection experiments.

6.2.4 Combination with complementary results from other experiments

Already now, dark matter searches with direct detection experiments and the detectors at the LHC strongly constrain the parameter space of dark matter models (see Section 2.3). While it is not always possible to relate the bounds from different observational techniques to each other, certain frameworks allow a complementary analysis: For example, the *Astrofit* package (Nguyen *et al.* 2012) was developed to incorporate astrophysical data in constraints on supersymmetric models. Using Astrofit, Bechtle *et al.* (2012) have demonstrated the effect that direct detection results (from XENON1T) can have on the SUSY parameter space; γ-ray limits on the annihilation cross-section were included in the fit, but did not provide strong constraints.

Nevertheless, with the advent of future γ-ray observatories, ever larger direct detection experiments and the full-energy LHC running planned to start in 2015, the combined analysis of complementary dark matter searches will certainly play a significant role. If, in the future, the LHC provides indications for any particular model of physics "beyond the standard model", this is just the better for indirect dark matter searches: Observers would gain a clearer view of what to look for in the sky.

[2] fermi.gsfc.nasa.gov/ssc/data/analysis/

6.3 Final remarks

As it was described in Chapter 2, it seems clear that *some* type of dark matter is immensely important for the development and structure of the universe, and there is good reason to believe that "new physics" may be expected at the TeV scale. Whether these two phenomena are indeed related, however, remains to be seen. The present experimental and observational efforts will provide important results within the next few years. But regardless of these outcomes, whether they "only" result in ever stronger parameter bounds or actually the detection of a promising signal: The refinement of analysis techniques, in particular for combining results from different experiments as it was presented in this thesis, will be highly important.

And so the case remains that dark matter may be weakly interacting, but it is certainly strongly captivating.

Appendices

Appendix A

Bayes' theorem, probabilities and likelihood functions

Chapter 4 relies heavily on likelihood functions, and partly on the posterior distributions of J factors (see also Appendix B). In the hope of minimizing possible confusion, a few definitions and properties of probabilities and likelihood functions are collected here.

A.1 Bayes' theorem

Bayes' theorem (Bayes 1764, see also Jaynes & Bretthorst (2003), Cousins (1995) and James 2006) relates the probability to observe a certain set of data D with the probability that a particular hypothesis H, concerning the data, is true. The theorem is often expressed as

$$P(H|D) = \frac{P(D|H) \times P(H)}{P(D)}\,, \tag{A.1}$$

where the different terms are defined as follows:

- $P(H|D)$ is the *posterior* probability: The probability that the hypothesis H is true, given the data D.
- $P(D|H)$ is usually called the *likelihood*: This is the probability to obtain the data D, if the hypothesis H is true.
- $P(H)$ is the *prior* probability for H to be true, *before* the data D are considered.
- $P(D) = \sum_H P(D|H)P(H)$, the *Bayesian evidence*, is the total probability to obtain the given data, summed over all possible hypotheses. This is mainly a normalization factor and often neglected.

Both the prior and the posterior probability are meaningful quantities only if probabilities are understood in the *Bayesian* sense, i.e. as a "degree of belief". An alternative framework is *Frequentism*, where a probability is defined as the limit of a relative frequency in a large number of trials. However, if the hypothesis of Equation A.1 is defined in terms of *model parameters*, the true values of these parameters are fixed by nature. Therefore, they are not randomly distributed, and it does not make sense to assign a Frequentist probability to these values.

Equation A.1 defines Bayes' theorem in terms of probabilities. However, the theorem becomes a little more intricate if, instead of probabilities P, probability *density* functions p are considered. These PDFs are defined for continuous random variables such that an *integration* is required to obtain a true probability: For example,

$$P(a < x < b) = \int_a^b \mathrm{d}x\, p(x) \tag{A.2}$$

for the random variable x. For any practical application, it is vital to take account of the differential $\mathrm{d}x$ related to the PDF $p(x)$, see e.g. the next section.

Incorporating such probability density functions, Bayes' theorem may be expressed as

$$p(H|D)\mathrm{d}H = \frac{p(D|H) \times (p(H)\mathrm{d}H)}{P(D)}\,. \tag{A.3}$$

Here, the terms $p\mathrm{d}H$ denote differential probabilities. The likelihood $p(D|H)$, on the other hand, is *no longer* a probability function once the data D are fixed. This is particularly important in the case of parameter transformations, as explained in the next section. In addition, likelihood functions are not *normalized* like probabilities, so that the integral $\int \mathrm{d}H\, p(D|H)$ over all possible H could be less or greater than one.

It should be noted that while posterior PDFs are inherently *Bayesian* quantities, the likelihood function is perfectly well-defined and meaningful in Frequentist statistics as well. (In fact, the maximum likelihood method was introduced by the eminent Frequentist R.A. Fisher, see e.g. Aldrich 1997; Stigler 2007.)

A.2 Parameter transformations

When a random variable x is replaced by another parameter $y = y(x)$, likelihood functions $\mathscr{L}$ and probability density functions transform differently:

While the *shape* of the likelihood function may change in such a parameter transformation, the *maximum likelihood* value stays invariant. That is, if the maximum of $\mathscr{L}(x)$ occurs at $\hat{x}$, the maximum of $\mathscr{L}(y)$ occurs at $y(\hat{x})$.

Conversely, PDFs transform as

$$p(y) = p(x)\frac{\mathrm{d}x}{\mathrm{d}y}\,, \tag{A.4}$$

so that the maximal value $p(\hat{y})$ does not typically occur at $y(\hat{x})$. An example is shown in the following appendix. Only the probabilities are conserved, i.e.,

$$\int_{y(x_1)}^{y(x_2)} \mathrm{d}y\, p(y) = \int_{x_1}^{x_2} \mathrm{d}x\, p(x)\,. \tag{A.5}$$

A.3 J factor PDFs

In Section 4.1.2, probability distributions of the J factors were used. These had been derived by other authors as the *posterior* distributions from the analysis of stellar velocity data. Hence, $p(J|J_m)$ denotes the probability density for the *true* value J, given the measured value J_m (Equation 4.8/B.8).

However, this PDF is taken as the *likelihood* $\mathscr{L}(J)$ of the model parameter J in the analysis of Chapter 4. This procedure has two caveats:

1. Using Equation 4.8/B.8 directly as a likelihood function means that the likelihood $\mathscr{L}(J)$ is no longer strictly log-normal. If $\mathscr{L}(J)$ were to be log-normal in J, the term J^{-1} in the equation would have to be replaced by J_m^{-1}.

2. This procedure is only valid if the J priors in the stellar velocity analyses are (reasonably) flat over the relevant ranges.

This was checked explicitly[1] for the publication by Ackermann *et al.* (2011). Concerning the J PDFs published by Charbonnier *et al.* (2011), the authors mention that the flat priors they use for dark matter halo parameters correspond to non-flat priors on J. However, they do not show the J prior or the likelihood function, and state that their J *result* is "robust" against variations of the priors. Therefore, and considering the similar data sets involved, it is assumed here that the resulting uncertainty of the posterior J distribution was not dominated by the shape of the effective J prior density in the analysis by Charbonnier *et al.* (2011). Hence, their posterior probabilities were used as approximations to the J likelihood as well.

Concerning Segue 1, Essig *et al.* (2010) state that the logarithmic likelihood for the J factor can be fitted with a Gaussian function, resulting in the values shown in Table 4.2. For Sagittarius dSph and the Fornax cluster, the J distribution functions are less well constrained. Nonetheless, it is assumed in Chapter 4 that these likelihoods follow a similar form.

[1] J. Conrad, private comm.

Appendix B

The "log-normal" J distributions

A random variable $x > 0$ is termed "log-normally" distributed if its natural logarithm $\ln x$ follows a normal (Gaussian) probability distribution with mean μ and variance σ^2. That is, with $y = \ln x$, the distribution of y is given by

$$f_N(y;\mu,\sigma) = \frac{1}{\sigma\sqrt{2\pi}} \exp\left\{-\frac{1}{2\sigma^2}(y-\mu)^2\right\} . \tag{B.1}$$

Making the parameter transformation $y \to x$ under the requirement that the differential probabilities are equal, i.e.

$$f_N(y)\,\mathrm{d}y = f_L(x)\,\mathrm{d}x\,, \tag{B.2}$$

and using the fact that $\frac{\mathrm{d}\ln x}{\mathrm{d}x} = \frac{1}{x}$, it follows that

$$f_L(x) = f_N(y(x)) \times \frac{\mathrm{d}y}{\mathrm{d}x} = f_N(y(x)) \times \frac{1}{x} . \tag{B.3}$$

Hence, the parameter x follows the distribution

$$f_L(x;\mu,\sigma) = \frac{1}{x\sigma\sqrt{2\pi}} \exp\left\{-\frac{1}{2\sigma^2}(\ln x-\mu)^2\right\} . \tag{B.4}$$

Unlike in the case of the normal distribution, the mode (i.e., the parameter value where the distribution has its maximum), median and mean of the log-normal distribution are not the same[1]. Instead,

$$\mathrm{Mode}(x) = e^{\mu-\sigma^2}\,, \tag{B.5}$$

$$\mathrm{Median}(x) = e^{\mu}\,, \tag{B.6}$$

$$\mathrm{Mean}(x) = e^{\mu+\sigma^2/2}\,. \tag{B.7}$$

[1]See, e.g., James (2006); note, however, that there is a sign error in the exponent of the expected value on Page 85, where a plus should replace the minus sign. (F. James, priv. comm.)

In Chapter 4, and following Ackermann *et al.* (2011), the probability distribution functions for the J factors are defined in terms of the logarithm to the base ten, i.e. $\log(J)$, as in Equation 4.8/B.8:

$$f_{\mathrm{PDF}}(J) = \frac{1}{\ln(10)\, J\, \sigma_J\, \sqrt{2\pi}} \exp\left\{ -0.5 \frac{\left[\log(J) - \log\left(J_m\right)\right]^2}{\sigma_J^2} \right\} \tag{B.8}$$

As mentioned there, $\log(J)$ is to be understood as the logarithm of the *numerical value* of J, i.e. $\log\left(J/\,\mathrm{GeV^2 cm^{-5}}\right)$. Matta *et al.* (2011) discuss why it is impossible to take the logarithm of dimensionful parameters.

The function f_{PDF} can be derived from the normal distribution by setting $y = \log J$, $\mu = \log J_m$ and $\sigma = \sigma_J$, according to the results of the analysis for each astrophysical object. Using the derivative

$$\frac{\mathrm{d}y}{\mathrm{d}J} = \frac{1}{J \times \ln(10)}\,, \tag{B.9}$$

Equation 4.8/B.8 results analogously to the usual log-normal distribution.

In order to compute the mode, median and mean values of this J distribution, one can use the identity $\ln J = \log J \times \ln 10$ and make the appropriate replacements $\mu \to \ln\left(J_m\right)$ and $\sigma \to \ln(10)\, \sigma_J$ in Equations B.5–B.7. Hence,

$$\begin{aligned}
\mathrm{Mode}(J) &= \exp\left\{ \ln\left(J_m\right) - \left(\ln(10)\sigma_J\right)^2 \right\} \\
&= J_m \times \exp\left\{ -\left(\ln(10)\sigma_J\right)^2 \right\}, \\
\mathrm{Median}(J) &= \exp\left\{ \ln\left(J_m\right) \right\} \\
&= J_m\,, \\
\mathrm{Mean}(J) &= \exp\left\{ \ln\left(J_m\right) + \left(\ln(10)\sigma_J\right)^2 /2 \right\} \\
&= J_m \times \exp\left\{ \left(\ln(10)\sigma_J\right)^2 /2 \right\}\,.
\end{aligned}$$

Figure B.1 shows the J distribution f_{PDF} of Segue 1 with all these values indicated. Figure B.2 shows in addition the corresponding *normal* distribution f_N of the *logarithmic* J values, with $y = \log_{10} J$, $\mu = \log_{10} J_m = 19.0$ and $\sigma = 0.6$. This figure shows that the mode of the normal distribution corresponds to the median of the log-normal distribution.

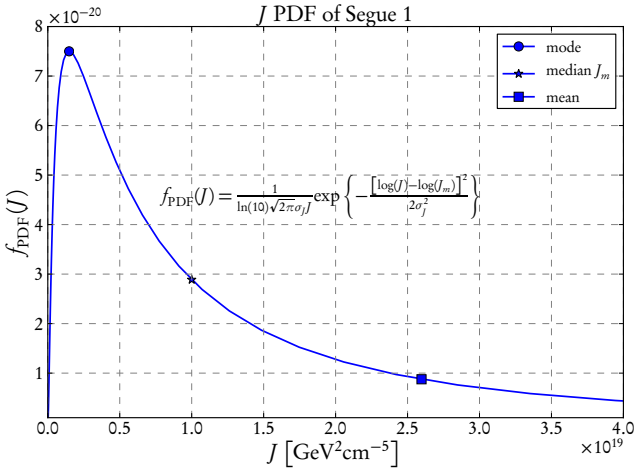

Figure B.1: The J distribution function of Segue 1, with $\log\left(J_m\right) = 19.0$ *and* $\sigma_J = 0.6$ *as derived by Essig* et al. *(2010). Mode, median and mean value of the distribution are indicated.*

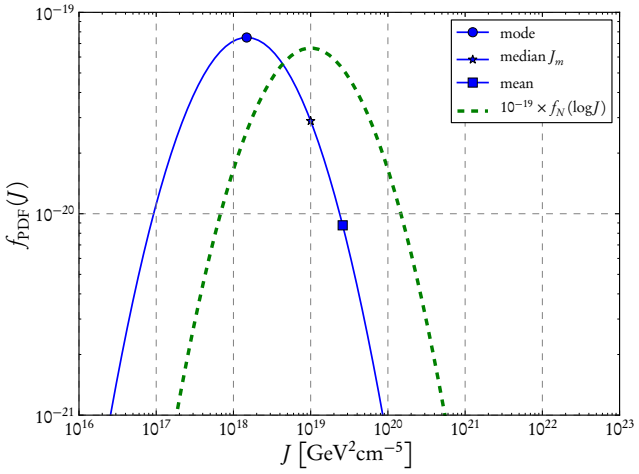

Figure B.2: The same J distribution function of Segue 1 as in Figure B.1, shown as a solid blue line, on logarithmic scales. In addition, the corresponding normal distribution of $\log J$*, i.e.* $f_N\left(\log J; \log J_m, \sigma_J\right)$*, is shown as a dashed green line, scaled by a factor* 10^{-19} *for visibility. One can see that the mode of the normal distribution, lying at* $\log\left(J_m\right) = 19.0$*, corresponds to the median of the log-normal distribution.*

Appendix C

Combined likelihood analysis: Additional figures

In Chapter 4, several of the figures were shown only for the case of dark matter self-annihilations to $b\overline{b}$ final states. In this appendix, the corresponding figures for W^+W^- and $\tau\overline{\tau}$ final states are shown.

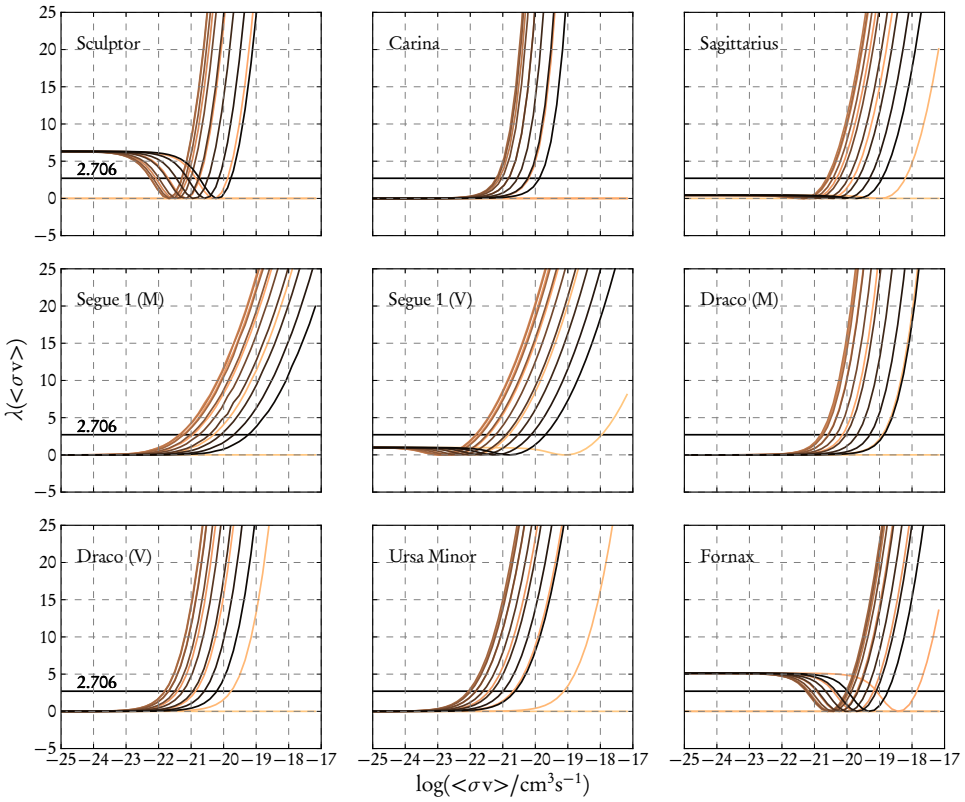

Figure C.1: The logarithmic profile likelihood functions $\lambda(\langle\sigma v\rangle)$ of the different observations, calculated for DM annihilations to W^+W^- pairs. (M) and (V) indicate observations by MAGIC and VERITAS, respectively. Each curve corresponds to one particular dark matter mass m_χ in the range from 100 GeV to 100 TeV, with lighter colours indicating lighter masses. The intersections of the likelihoods with the lines drawn at $\lambda = 2.706$ indicate the 95% C.L. upper limits on the annihilation cross-section $\langle\sigma v\rangle_{\mathrm{UL}}$. (In the cases of Sculptor and Fornax, this applies to the respective intersections at higher *values of $\langle\sigma v\rangle$.)*
This figure corresponds to Figure 4.5, except for the different final state.

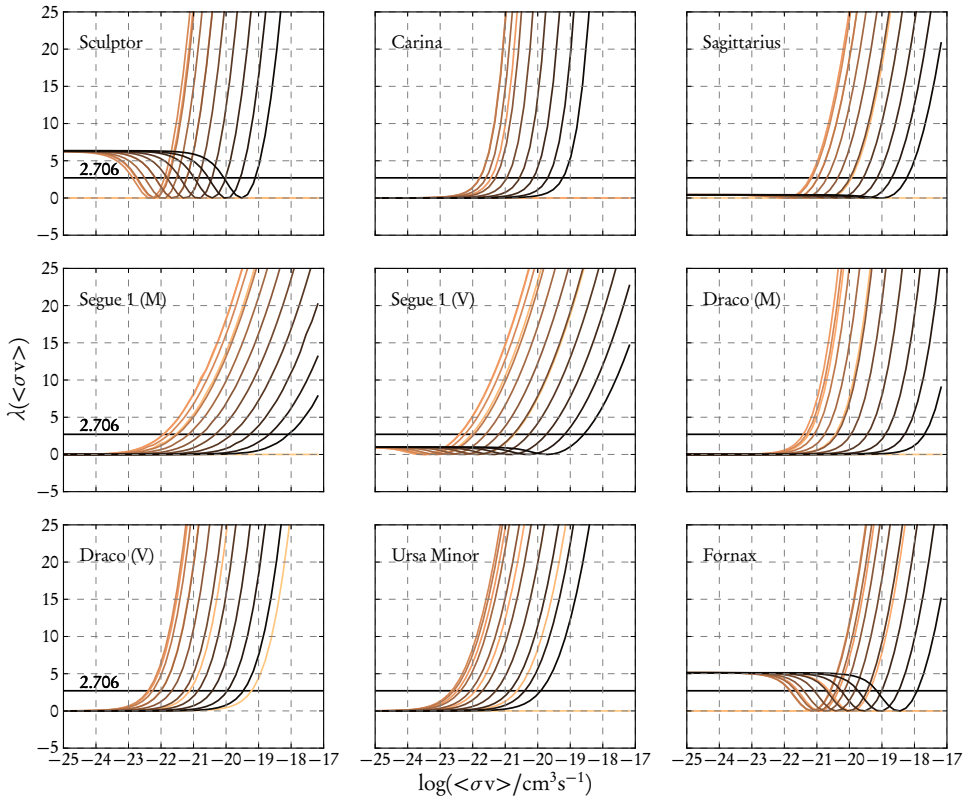

Figure C.2: Same as Figure C.1, but for DM annihilations to $\tau\overline{\tau}$ pairs.

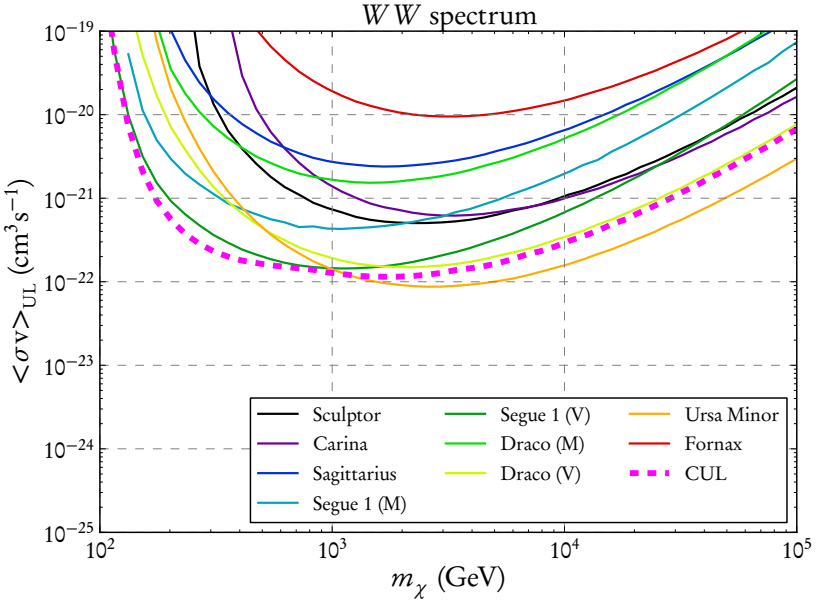

Figure C.3: Upper limits (95% C.L.) on the DM self-annihilation cross-section $\langle\sigma v\rangle$, for annihilations to W^+W^- pairs. Solid lines indicate the limits derived from the likelihood functions of the separate observations, while the thick dashed line (CUL) shows the limit derived with the combined likelihood method.
This corresponds to Figure 4.9, except for the different final state.

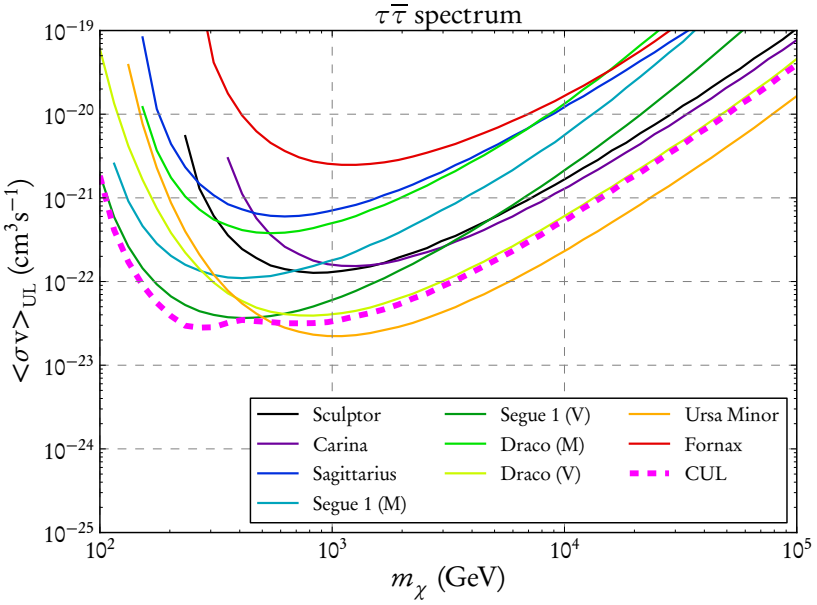

Figure C.4: Same as Figure C.3, but for dark matter self-annihilations to $\tau\overline{\tau}$ pairs.

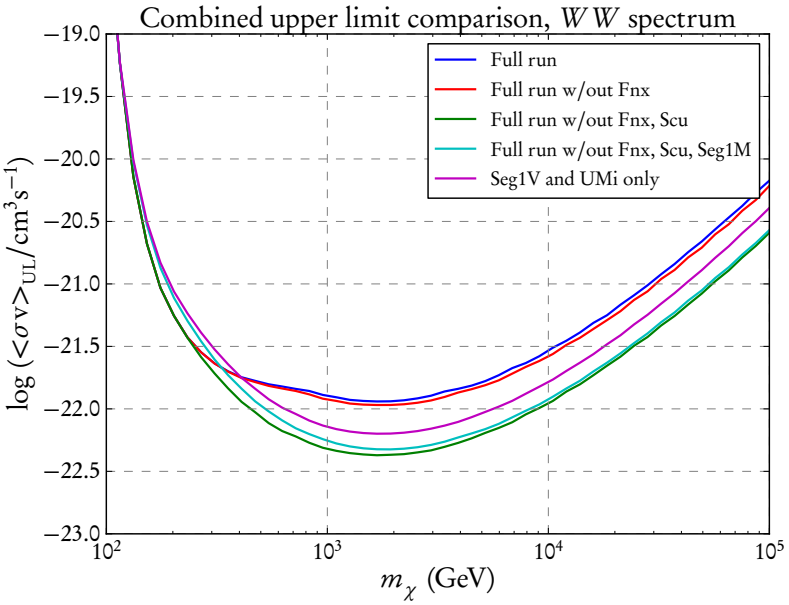

Figure C.5: Comparison of combined limits on $\langle\sigma v\rangle$, for annihilations to W^+W^- pairs. The upper limits (95% C.L.) are derived from the different sets of data indicated in the legend. This corresponds to Figure 4.12, except for the different final state.

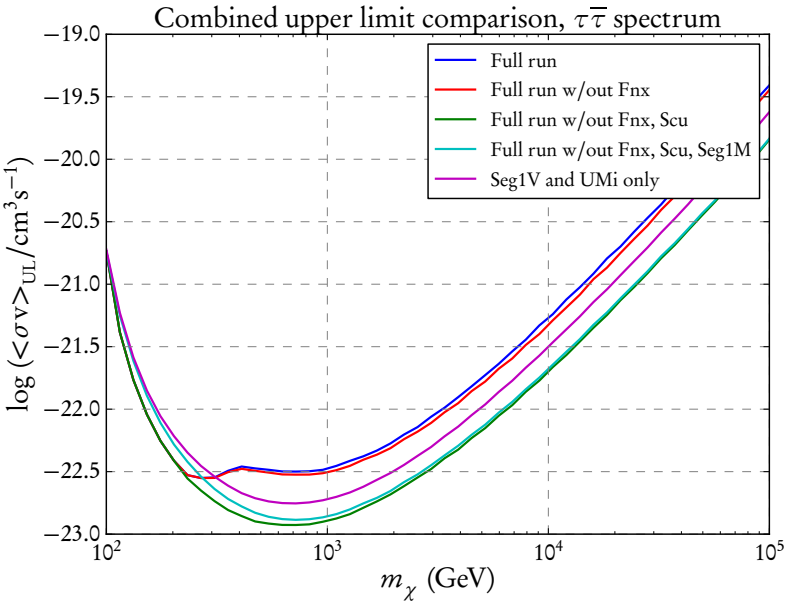

Figure C.6: Same as Figure C.5, but for dark matter self-annihilations to $\tau\overline{\tau}$ pairs.

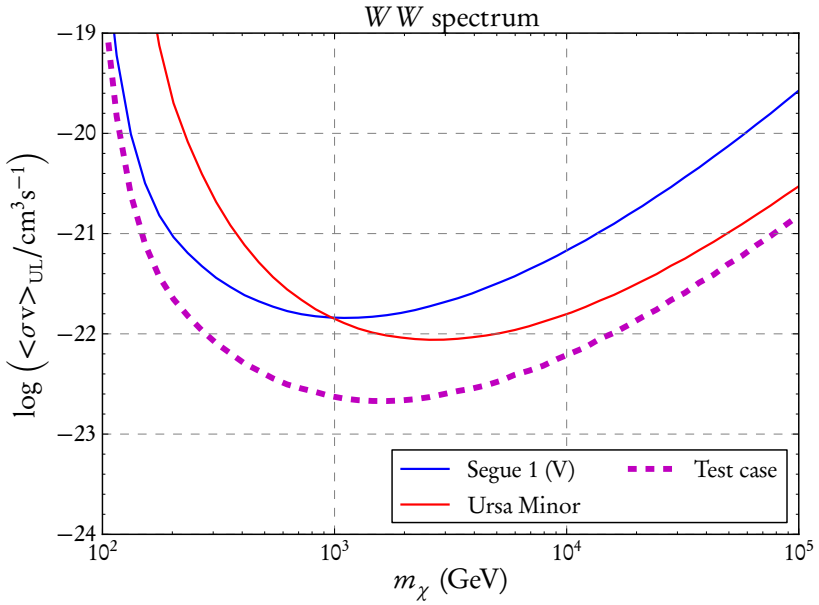

Figure C.7: Artificial test case: While the 95% C.L. upper limits on $\langle \sigma v \rangle$ from Segue 1 and Ursa Minor (solid lines) are those derived from the actual VERITAS data, the dashed line shows the limit that would be produced by the five-fold combination of these two datasets. This corresponds to Figure 4.13, except for the different final state.

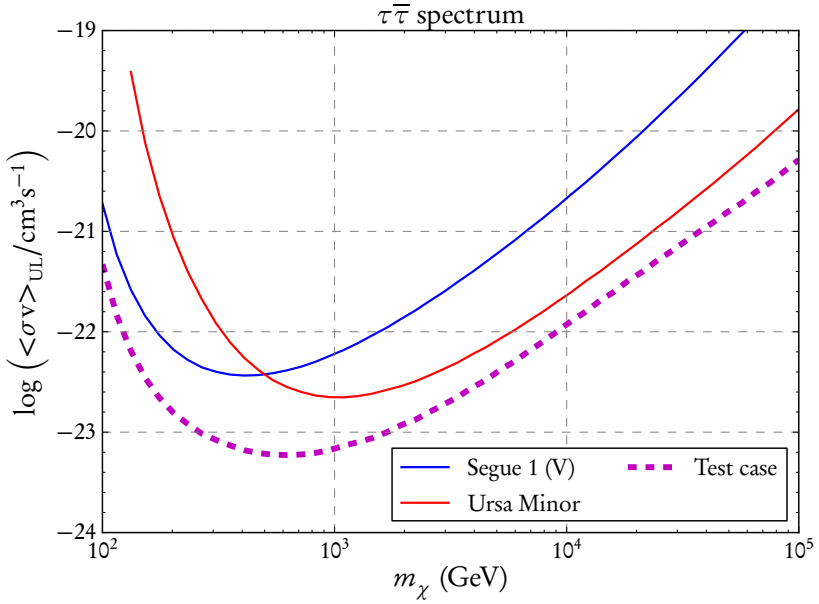

Figure C.8: Same as Figure C.7, but for dark matter self-annihilations to $\tau\overline{\tau}$ pairs.

Bibliography

Aad, G. *et al.* (2012): Physics Letters B, 716, 1: 1 – 29. http://dx.doi.org/10.1016/j.physletb.2012.08.020

Aartsen, M. G. *et al.* (2013): Phys. Rev. D, 88, 12: 122001. http://arxiv.org/abs/1307.3473, http://dx.doi.org/10.1103/PhysRevD.88.122001

Abazajian, K. *et al.* (2003): AJ, 126: 2081–2086. http://arxiv.org/abs/astro-ph/0305492, http://dx.doi.org/10.1086/378165

Abazajian, K. N. *et al.* (2012): ArXiv e-prints. http://arxiv.org/abs/1204.5379

Abramowski, A. *et al.* (H.E.S.S. Collaboration) (2012): ApJ, 750: 123. http://arxiv.org/abs/1202.5494, http://dx.doi.org/10.1088/0004-637X/750/2/123

Abramowski, A. *et al.* (H.E.S.S. Collaboration) (2011a): Astroparticle Physics, 34: 608. http://arxiv.org/abs/1012.5602, http://dx.doi.org/10.1016/j.astropartphys.2010.12.006

Abramowski, A. *et al.* (H.E.S.S. Collaboration) (2011b): Phys. Rev. Lett., 106, 16: 161301. http://arxiv.org/abs/1103.3266, http://dx.doi.org/10.1103/PhysRevLett.106.161301

Abramowski, A. *et al.* (H.E.S.S. Collaboration) (2013): Phys. Rev. Lett., 110: 041301. http://dx.doi.org/10.1103/PhysRevLett.110.041301

Abramowski, A. *et al.* (H.E.S.S. Collaboration) (2014): ApJ, 783: 63. http://dx.doi.org/10.1088/0004-637X/783/1/63

Acciari, V. A. *et al.* (2010): ApJ, 720: 1174–1180. http://arxiv.org/abs/1006.5955, http://dx.doi.org/10.1088/0004-637X/720/2/1174

Acharya, B. *et al.* (2013): Astroparticle Physics, 43, 0: 3 – 18. http://dx.doi.org/10.1016/j.astropartphys.2013.01.007

Ackermann, M. *et al.* (2011): Phys. Rev. Lett., 107, 24: 241302. http://arxiv.org/abs/1108.3546, http://dx.doi.org/10.1103/PhysRevLett.107.241302

Ackermann, M. *et al.* (Fermi-LAT Collaboration) (2014): Phys. Rev. D, 89: 042001. http://dx.doi.org/10.1103/PhysRevD.89.042001

Ackermann, M. *et al.* (2010): J. Cosmology Astropart. Phys., 5: 25. http://arxiv.org/abs/1002.2239, http://dx.doi.org/10.1088/1475-7516/2010/05/025

Ackermann, M. *et al.* (Fermi-LAT Collaboration) (2013): Phys. Rev. D, 88: 082002. http://dx.doi.org/10.1103/PhysRevD.88.082002

Ade, P. A. R. *et al.* (BICEP2 Collaboration) (2014): Phys. Rev. Lett., 112: 241101. http://dx.doi.org/10.1103/PhysRevLett.112.241101

Adriani, O. *et al.* (PAMELA Collaboration) (2009): Nature, 458: 607. http://arxiv.org/abs/0810.4995, http://dx.doi.org/10.1038/nature07942

Adriani, O. *et al.* (2011): Science, 332: 69–. http://arxiv.org/abs/1103.4055, http://dx.doi.org/10.1126/science.1199172

Agnese, R. *et al.* (CDMS Collaboration) (2013): Phys. Rev. Lett., 111: 251301. http://dx.doi.org/10.1103/PhysRevLett.111.251301

Aguilar, M. *et al.* (AMS Collaboration) (2013): Phys. Rev. Lett., 110: 141102. http://dx.doi.org/10.1103/PhysRevLett.110.141102

Aharonian, F. *et al.* (1999): Phys. Rev. D, 59, 9: 092003. http://arxiv.org/abs/astro-ph/9901160, http://dx.doi.org/10.1103/PhysRevD.59.092003

Aharonian, F. *et al.* (2005): Science, 307, 5717: 1938–1942. http://dx.doi.org/10.1126/science.1108643

Aharonian, F. *et al.* (2006a): Phys. Rev. Lett., 97, 22: 221102. http://arxiv.org/abs/astro-ph/0610509, http://dx.doi.org/10.1103/PhysRevLett.97.221102

Aharonian, F. *et al.* (2008): Astroparticle Physics, 29: 55–62. http://arxiv.org/abs/0711.2369, http://dx.doi.org/10.1016/j.astropartphys.2007.11.007

Aharonian, F. *et al.* (2009): A&A, 502: 437–443. http://arxiv.org/abs/0907.0727, http://dx.doi.org/10.1051/0004-6361/200912086

Aharonian, F. *et al.* (2010): Astroparticle Physics, 33: 274–275. http://dx.doi.org/10.1016/j.astropartphys.2010.01.007

Aharonian, F. A. *et al.* (2004): Nature, 432: 75–77. http://arxiv.org/abs/astro-ph/0411533, http://dx.doi.org/10.1038/nature02960

Aharonian, F. *et al.* (2006b): A&A, 457: 899. http://arxiv.org/abs/[astro-ph/0607333], http://dx.doi.org/10.1051/0004-6361:20065351

Aharonian, F. *et al.* (2006c): Science, 314: 1424. http://arxiv.org/abs/astro-ph/0612016, http://dx.doi.org/10.1126/science.1134408

Aharonian, F. *et al.* (2006): A&A, 457, 3: 899–915. http://dx.doi.org/10.1051/0004-6361:20065351

Aharonian, F. *et al.* (H.E.S.S. Collaboration) (2008): Phys. Rev. Lett., 101: 261104. http://dx.doi.org/10.1103/PhysRevLett.101.261104

Aharonian, F. *et al.* (2009): A&A, 508: 561. http://arxiv.org/abs/0905.0105, http://dx.doi.org/10.1051/0004-6361/200913323

Akerib, S., D. *et al.* ((LUX Collaboration)) (2014): Phys. Rev. Lett., 112: 091303. http://dx.doi.org/10.1103/PhysRevLett.112.091303

Albert, J. *et al.* (2008): ApJ, 675, 1: L25. http://stacks.iop.org/1538-4357/675/i=1/a=L25

Albert, J. *et al.* (2008a): ApJ, 679: 428–431. http://arxiv.org/abs/0711.2574, http://dx.doi.org/10.1086/529135

Albert, J. *et al.* (2008b): ApJ, 674: 1037–1055. http://arxiv.org/abs/0705.3244, http://dx.doi.org/10.1086/525270

Aldrich, J. (1997): Statistical Science, 12, 3: 162–176. http://dx.doi.org/10.1214/ss/1030037906

Aleksić, J. *et al.* (2011): J. Cosmology Astropart. Phys., 6: 035. http://arxiv.org/abs/1103.0477, http://dx.doi.org/10.1088/1475-7516/2011/06/035

Aleksić, J. *et al.* (2010): ApJ, 710: 634. http://arxiv.org/abs/0909.3267, http://dx.doi.org/10.1088/0004-637X/710/1/634

Aleksić, J. *et al.* (2012a): A&A, 541: A99. http://arxiv.org/abs/1111.5544, http://dx.doi.org/10.1051/0004-6361/201118502

Aleksić, J. *et al.* (2012b): Astroparticle Physics, 35: 435–448. http://arxiv.org/abs/1108.1477, http://dx.doi.org/10.1016/j.astropartphys.2011.11.007

Aleksić, J. *et al.* (2014): JCAP, 1402: 008. http://arxiv.org/abs/1312.1535, http://dx.doi.org/10.1088/1475-7516/2014/02/008

Aliu, E. *et al.* (2009): ApJ, 697: 1299–1304. http://arxiv.org/abs/0810.3561, http://dx.doi.org/10.1088/0004-637X/697/2/1299

Aliu, E. *et al.* (2012): Phys. Rev. D, 85, 6: 062001. http://arxiv.org/abs/1202.2144, http://dx.doi.org/10.1103/PhysRevD.85.062001

Aliu, E. *et al.* (2008): Science, 322: 1221–. http://arxiv.org/abs/0809.2998, http://dx.doi.org/10.1126/science.1164718

Allahverdi, R. *et al.* (2010): Annual Review of Nuclear and Particle Science, 60: 27–51. http://arxiv.org/abs/1001.2600, http://dx.doi.org/10.1146/annurev.nucl.012809.104511

Alpher, R. A., Bethe, H. & Gamow, G. (1948): Physical Review, 73: 803–804. http://dx.doi.org/10.1103/PhysRev.73.803

Amenomori, M. *et al.* (2006): Science, 314: 439–443. http://arxiv.org/abs/astro-ph/0610671, http://dx.doi.org/10.1126/science.1131702

Anderhalden, D. & Diemand, J. (2013): J. Cosmology Astropart. Phys., 2013, 04: 009. http://stacks.iop.org/1475-7516/2013/i=04/a=009

Anderhub, H. *et al.* (2011): NIM A, 639, 1: 58 – 61. http://dx.doi.org/10.1016/j.nima.2010.10.081

Anderson, P. W. (1963): Physical Review, 130: 439–442. http://dx.doi.org/10.1103/PhysRev.130.439

Aprile, E. *et al.* (2012): Phys. Rev. Lett., 109, 18: 181301. http://arxiv.org/abs/1207.5988, http://dx.doi.org/10.1103/PhysRevLett.109.181301

Arina, C., Bertone, G. & Silverwood, H. (2013): Phys. Rev. D, 88: 013002. http://dx.doi.org/10.1103/PhysRevD.88.013002

Arkani-Hamed, N. *et al.* (2009): Phys.Rev., D79: 015014. http://arxiv.org/abs/0810.0713, http://dx.doi.org/10.1103/PhysRevD.79.015014

Atwood, W. B. *et al.* (2009): ApJ, 697: 1071–1102. http://arxiv.org/abs/0902.1089, http://dx.doi.org/10.1088/0004-637X/697/2/1071

Atwood, W. *et al.* (2013): ArXiv e-prints. http://arxiv.org/abs/1303.3514

Balzer, A. *et al.* (2014): Astroparticle Physics, 54, 0: 67 – 80. http://dx.doi.org/10.1016/j.astropartphys.2013.11.007

Bartelmann, M. *et al.* (2013): Space Science Reviews, 177, 1-4: 3–29. http://dx.doi.org/10.1007/s11214-013-9977-6

Battaglia, G., Helmi, A. & Breddels, M. (2013): New A Rev., 57: 52–79. http://arxiv.org/abs/1305.5965, http://dx.doi.org/10.1016/j.newar.2013.05.003

Bayes, R. T. (1764): Phil.Trans.Roy.Soc.Lond., 53: 370–418. http://dx.doi.org/10.1098/rstl.1763.0053

Becherini, Y. *et al.* (2011): Astroparticle Physics, 34: 858–870. http://arxiv.org/abs/1104.5359, http://dx.doi.org/10.1016/j.astropartphys.2011.03.005

Bechtle, P. *et al.* (2012): Journal of High Energy Physics, 6: 98. http://arxiv.org/abs/1204.4199, http://dx.doi.org/10.1007/JHEP06(2012)098

Begeman, K. G., Broeils, A. H. & Sanders, R. H. (1991): MNRAS, 249: 523–537

Belikov, A. V., Zaharijas, G. & Silk, J. (2012): Phys. Rev. D, 86, 8: 083516. http://arxiv.org/abs/1207.2412, http://dx.doi.org/10.1103/PhysRevD.86.083516

Bell, N. F. *et al.* (2011): Phys. Rev. D, 84, 10: 103517. http://arxiv.org/abs/1101.3357, http://dx.doi.org/10.1103/PhysRevD.84.103517

Belokurov, V. *et al.* (2007): ApJ, 654: 897–906. http://arxiv.org/abs/astro-ph/0608448, http://dx.doi.org/10.1086/509718

Belokurov, V. *et al.* (2014): MNRAS, 441: 2124–2133. http://arxiv.org/abs/1403.3406, http://dx.doi.org/10.1093/mnras/stu626

Bennett, C. L. (2006): Nature, 440: 1126–1131. http://dx.doi.org/10.1038/nature04803

Bennett, C. L. *et al.* (2003): ApJS, 148: 1–27. http://arxiv.org/abs/astro-ph/0302207, http://dx.doi.org/10.1086/377253

Berge, D., Funk, S. & Hinton, J. (2007): A&A, 466, 3: 1219–1229. http://dx.doi.org/10.1051/0004-6361:20066674

Bergström, L., Ullio, P. & Buckley, J. H. (1998): Astroparticle Physics, 9: 137. http://arxiv.org/abs/astro-ph/9712318, http://dx.doi.org/10.1016/S0927-6505(98)00015-2

Bergström, L. *et al.* (2005): Phys. Rev. Lett., 95: 241301. http://dx.doi.org/10.1103/PhysRevLett.95.241301

Bergström, L., Edsjö, J. & Zaharijas, G. (2009): Phys. Rev. Lett., 103, 3: 031103. http://arxiv.org/abs/0905.0333, http://dx.doi.org/10.1103/PhysRevLett.103.031103

Bergström, L., Bringmann, T. & Edsjö, J. (2011): Phys. Rev. D, 83, 4: 045024. http://arxiv.org/abs/1011.4514, http://dx.doi.org/10.1103/PhysRevD.83.045024

Bergström, L. *et al.* (2012): J. Cosmology Astropart. Phys., 11: 025. http://arxiv.org/abs/1207.6773, http://dx.doi.org/10.1088/1475-7516/2012/11/025

Bergström, L. *et al.* (2013): Phys. Rev. Lett., 111, 17: 171101. http://arxiv.org/abs/1306.3983, http://dx.doi.org/10.1103/PhysRevLett.111.171101

Bergström, L. (1989): Physics Letters B, 225, 4: 372 – 380. http://dx.doi.org/10.1016/0370-2693(89)90585-6

Beringer, J. *et al.* (2012): Phys. Rev. D, 86, 1: 010001. http://dx.doi.org/10.1103/PhysRevD.86.010001

Bernabei, R. *et al.* (2008): EPJ C, 56, 3: 333–355. http://dx.doi.org/10.1140/epjc/s10052-008-0662-y

Bertone, G., *Particle Dark Matter : Observations, Models and Searches* (Cambridge University Press, 2010)

Bertone, G., Hooper, D. & Silk, J. (2005): Phys. Rept., 405: 279. http://arxiv.org/abs/hep-ph/0404175, http://dx.doi.org/10.1016/j.physrep.2004.08.031

Biermann, P. L., de Vega, H. J. & Sanchez, N. G. (2013): ArXiv e-prints. http://arxiv.org/abs/1305.7452

Bilenky, S. M. (2005): Physica Scripta, 2005, T121: 17. http://stacks.iop.org/1402-4896/2005/i=T121/a=001

Binney, J. & Tremaine, S., *Galactic Dynamics* (Princeton University Press, 2008)

Birkedal, A., Matchev, K. & Perelstein, M. (2004): Phys. Rev. D, 70: 077701. http://dx.doi.org/10.1103/PhysRevD.70.077701

Blumenthal, G. R. *et al.* (1986): ApJ, 301: 27–34. http://dx.doi.org/10.1086/163867

Bohec, S. L. *et al.* (1998): NIM A, 416, 2–3: 425 – 437. http://dx.doi.org/10.1016/S0168-9002(98)00750-5

Borla Tridon, D. *et al.* (2011): International Cosmic Ray Conference, 6: 43. http://arxiv.org/abs/1110.4008

Borriello, E. *et al.* (2012): MNRAS, 425: 1628–1632. http://arxiv.org/abs/1109.5943, http://dx.doi.org/10.1111/j.1365-2966.2012.21498.x

Bovy, J. (2009): Phys. Rev. D, 79, 8: 083539. http://arxiv.org/abs/0903.0413, http://dx.doi.org/10.1103/PhysRevD.79.083539

Boylan-Kolchin, M., Bullock, J. S. & Kaplinghat, M. (2011): MNRAS, 415: L40–L44. http://arxiv.org/abs/1103.0007, http://dx.doi.org/10.1111/j.1745-3933.2011.01074.x

Bradley, R. *et al.* (2003): Rev. Mod. Phys., 75: 777–817. http://dx.doi.org/10.1103/RevModPhys.75.777

Bringmann, T. (2009): New Journal of Physics, 11, 10: 105027. http://arxiv.org/abs/0903.0189, http://dx.doi.org/10.1088/1367-2630/11/10/105027

Bringmann, T. & Calore, F. (2014): Phys. Rev. Lett., 112, 7: 071301. http://arxiv.org/abs/1308.1089, http://dx.doi.org/10.1103/PhysRevLett.112.071301

Bringmann, T. & Weniger, C. (2012): Physics of the Dark Universe, 1: 194–217. http://arxiv.org/abs/1208.5481, http://dx.doi.org/10.1016/j.dark.2012.10.005

Bringmann, T., Bergström, L. & Edsjö, J. (2008): JHEP, 01: 049. http://arxiv.org/abs/0710.3169, http://dx.doi.org/10.1088/1126-6708/2008/01/049

Bringmann, T. *et al.* (2014): Phys. Rev. D, 89, 2: 023012. http://arxiv.org/abs/1303.3284, http://dx.doi.org/10.1103/PhysRevD.89.023012

Bromm, V. *et al.* (2009): Nature, 459: 49–54. http://arxiv.org/abs/0905.0929, http://dx.doi.org/10.1038/nature07990

Brun, R. & Rademakers, F. (1997): NIM A, 389: 81–86. http://dx.doi.org/10.1016/S0168-9002(97)00048-X

Bullock, J. S. (2010): ArXiv e-prints. http://arxiv.org/abs/1009.4505

Bullock, J. S. *et al.* (2001): MNRAS, 321, 3: 559–575. http://dx.doi.org/10.1046/j.1365-8711.2001.04068.x

Buote, D. A. *et al.* (2007): ApJ, 664: 123–134. http://arxiv.org/abs/astro-ph/0610135, http://dx.doi.org/10.1086/518684

Burch, B. & Cowsik, R. (2013): ApJ, 779: 35. http://arxiv.org/abs/1306.1920, http://dx.doi.org/10.1088/0004-637X/779/1/35

Burkert, A. (1995): ApJ, 447, 1: L25. http://stacks.iop.org/1538-4357/447/i=1/a=L25

Calcagni, G. *et al.* (Editors) (2013): *Quantum Gravity and Quantum Cosmology*, volume 863 of *Lecture Notes in Physics, Berlin Springer Verlag* (2013). http://dx.doi.org/10.1007/978-3-642-33036-0

Carlson, E. D., Machacek, M. E. & Hall, L. J. (1992): ApJ, 398: 43–52. http://dx.doi.org/10.1086/171833

Cembranos, J. A. R. *et al.* (2011): Phys. Rev. D, 83: 083507. http://dx.doi.org/10.1103/PhysRevD.83.083507

Cembranos, J. A. R. *et al.* (2013): Journal of High Energy Physics, 9: 77. http://arxiv.org/abs/1305.2124, http://dx.doi.org/10.1007/JHEP09(2013)077

Charbonnier, A. *et al.* (2011): MNRAS, 418: 1526–1556. http://arxiv.org/abs/1104.0412, http://dx.doi.org/10.1111/j.1365-2966.2011.19387.x

Chatrchyan, S. *et al.* (2012): Physics Letters B, 716, 1: 30 – 61. http://dx.doi.org/10.1016/j.physletb.2012.08.021

Cherenkov, P. A. (1937): Physical Review, 52: 378–379. http://dx.doi.org/10.1103/PhysRev.52.378

Cherenkov, P. (1986): NIM A, 248, 1: 1 – 4. http://dx.doi.org/10.1016/0168-9002(86)90487-0

Cheung, C. C. *et al.* (2014): ApJ, 782: L14. http://arxiv.org/abs/1401.0548, http://dx.doi.org/10.1088/2041-8205/782/2/L14

Cho, A. (2012): Science, 338, 6114: 1524–1525. http://dx.doi.org/10.1126/science.338.6114.1524

Ciafaloni, P. *et al.* (2011): J. Cosmology Astropart. Phys., 3: 019. http://arxiv.org/abs/1009.0224, http://dx.doi.org/10.1088/1475-7516/2011/03/019

Cirelli, M. *et al.* (2011): JCAP, 1103: 051. http://arxiv.org/abs/1012.4515, http://dx.doi.org/10.1088/1475-7516/2011/03/051

Cirelli, M. *et al.* (2012): Phys. Rev. D, 86, 8: 083506. http://arxiv.org/abs/1205.5283, http://dx.doi.org/10.1103/PhysRevD.86.083506

Clowe, D. *et al.* (2006): ApJ, 648: L109–L113. http://arxiv.org/abs/astro-ph/0608407, http://dx.doi.org/10.1086/508162

Colafrancesco, S., Profumo, S. & Ullio, P. (2006): A&A, 455: 21. http://arxiv.org/abs/astro-ph/0507575, http://dx.doi.org/10.1051/0004-6361:20053887

Cole, S. *et al.* (2005): MNRAS, 362: 505–534. http://arxiv.org/abs/astro-ph/0501174, http://dx.doi.org/10.1111/j.1365-2966.2005.09318.x

Collins, M. L. M. *et al.* (2014): ApJ, 783, 1: 7. http://stacks.iop.org/0004-637X/783/i=1/a=7

Comerford, J. M. & Natarajan, P. (2007): MNRAS, 379: 190–200. http://arxiv.org/abs/astro-ph/0703126, http://dx.doi.org/10.1111/j.1365-2966.2007.11934.x

Consolandi, C. (2014): ArXiv e-prints. On behalf of the AMS-02 Collaboration, http://arxiv.org/abs/1402.0467

Cortina, J. *et al.* (2009): ArXiv e-prints. http://arxiv.org/abs/0907.1211

Cousins, R. D. (1995): American Journal of Physics, 63, 5: 398–410. http://dx.doi.org/10.1119/1.17901

Cowan, G. *et al.* (2011): EPJ C, 71, 2: 1–19. http://dx.doi.org/10.1140/epjc/s10052-011-1554-0

Dawson, W. A. *et al.* (2012): ApJ, 747, 2: L42. http://stacks.iop.org/2041-8205/747/i=2/a=L42

de Bernardis, P. *et al.* (2000): Nature, 404: 955–959. http://arxiv.org/abs/astro-ph/0004404

de Blok, W. J. G. (2010): Advances in Astronomy, 2010. http://arxiv.org/abs/0910.3538, http://dx.doi.org/10.1155/2010/789293

de Naurois, M. & Rolland, L. (2009): Astroparticle Physics, 32: 231. http://arxiv.org/abs/0907.2610, http://dx.doi.org/10.1016/j.astropartphys.2009.09.001

Di Cintio, A. *et al.* (2014): MNRAS, 437, 1: 415–423. http://dx.doi.org/10.1093/mnras/stt1891

Dicke, R. H. *et al.* (1965): ApJ, 142: 414–419. http://dx.doi.org/10.1086/148306

Dickinson, H. & Conrad, J. (2013): Astroparticle Physics, 41, 0: 17 – 30. http://dx.doi.org/10.1016/j.astropartphys.2012.10.004

Diemand, J., Moore, B. & Stadel, J. (2005): Nature, 433: 389–391. http://arxiv.org/abs/astro-ph/0501589, http://dx.doi.org/10.1038/nature03270

Diemand, J., Kuhlen, M. & Madau, P. (2006): ApJ, 649: 1. http://arxiv.org/abs/astro-ph/0603250, http://dx.doi.org/10.1086/506377

Diemand, J. *et al.* (2008): Nature, 454: 735. http://arxiv.org/abs/0805.1244, http://dx.doi.org/10.1038/nature07153

Dodelson, S. (2011): International Journal of Modern Physics D, 20: 2749–2753. http://arxiv.org/abs/1112.1320, http://dx.doi.org/10.1142/S0218271811020561

Doro, M. (2014): NIM A, 742: 99–106. http://dx.doi.org/10.1016/j.nima.2013.12.010

Doro, M. *et al.* (2013): Astroparticle Physics, 43, 0: 189 – 214. http://dx.doi.org/10.1016/j.astropartphys.2012.08.002

Drinkwater, M. J., Gregg, M. D. & Colless, M. (2001): ApJ, 548: L139. http://arxiv.org/abs/astro-ph/0012415, http://dx.doi.org/10.1086/319113

Duffy, L. D. & van Bibber, K. (2009): New Journal of Physics, 11, 10: 105008. http://stacks.iop.org/1367-2630/11/i=10/a=105008

Dugger, L., Jeltema, T. E. & Profumo, S. (2010): J. Cosmology Astropart. Phys., 12: 015. http://arxiv.org/abs/1009.5988, http://dx.doi.org/10.1088/1475-7516/2010/12/015

Egorov, A. E. & Pierpaoli, E. (2013): Phys. Rev. D, 88, 2: 023504. http://arxiv.org/abs/1304.0517, http://dx.doi.org/10.1103/PhysRevD.88.023504

Einasto, J. (1965): Trudy Astrofizicheskogo Instituta Alma-Ata, 5: 87–100

Eisenstein, D. J. *et al.* (2005): ApJ, 633: 560–574. http://arxiv.org/abs/astro-ph/0501171, http://dx.doi.org/10.1086/466512

El-Zant, A., Shlosman, I. & Hoffman, Y. (2001): ApJ, 560: 636. http://arxiv.org/abs/astro-ph/0103386, http://dx.doi.org/10.1086/322516

Ellis, J. (1985): Nature, 313: 626–627. http://dx.doi.org/10.1038/313626a0

Ellis, J. *et al.* (1984): Nuclear Physics B, 238: 453–476. http://dx.doi.org/10.1016/0550-3213(84)90461-9

Englert, F. & Brout, R. (1964): Phys. Rev. Lett., 13: 321–323. http://dx.doi.org/10.1103/PhysRevLett.13.321

Essig, R. *et al.* (2010): Phys. Rev. D, 82, 12: 123503. http://arxiv.org/abs/1007.4199, http://dx.doi.org/10.1103/PhysRevD.82.123503

Famaey, B. & McGaugh, S. S. (2012): Living Reviews in Relativity, 15: 10. http://arxiv.org/abs/1112.3960, http://dx.doi.org/10.12942/lrr-2012-10

Famaey, B. & McGaugh, S. (2013): Journal of Physics: Conference Series, 437, 1: 012001. http://stacks.iop.org/1742-6596/437/i=1/a=012001

Farrar, G. (2003): Int.J.Theor.Phys., 42: 1211–1218. http://dx.doi.org/10.1023/A:1025702431127

Feldman, G. J. & Cousins, R. D. (1998): Phys. Rev. D, 57: 3873. http://arxiv.org/abs/arXiv:physics/9711021, http://dx.doi.org/10.1103/PhysRevD.57.3873

Feng, J. L. (2010): ARA&A, 48: 495–545. http://arxiv.org/abs/1003.0904, http://dx.doi.org/10.1146/annurev-astro-082708-101659

Feng, J. L., Kaplinghat, M. & Yu, H.-B. (2010): Phys. Rev. D, 82: 083525. http://dx.doi.org/10.1103/PhysRevD.82.083525

Fernandes, M. V., Horns, D. & Raue, M., In "American Institute of Physics Conference Series", , edited by F. A. Aharonian, W. Hofmann & F. M. Rieger, volume 1505, pp. 725–728 (2012). http://dx.doi.org/10.1063/1.4772362

Fiasson, A. *et al.* (2010): Astroparticle Physics, 34: 25–32. http://arxiv.org/abs/1004.3375, http://dx.doi.org/10.1016/j.astropartphys.2010.04.006

Fixsen, D. J. (2009): ApJ, 707: 916–920. http://arxiv.org/abs/0911.1955, http://dx.doi.org/10.1088/0004-637X/707/2/916

Folkes, S. *et al.* (1999): MNRAS, 308: 459–472. http://arxiv.org/abs/astro-ph/9903456, http://dx.doi.org/10.1046/j.1365-8711.1999.02721.x

Fomin, V. P. *et al.* (1994): Astroparticle Physics, 2: 137–150. http://dx.doi.org/10.1016/0927-6505(94)90036-1

Freese, K. (2009): EAS Publications Series, 36: 113–126. http://dx.doi.org/10.1051/eas/0936016

Frenk, C. S. & White, S. D. M. (2012): Annalen der Physik, 524: 507–534. http://arxiv.org/abs/1210.0544, http://dx.doi.org/10.1002/andp.201200212

Funk, S. (2013): ArXiv e-prints. http://arxiv.org/abs/1310.2695

Garrison-Kimmel, S. *et al.* (2014): MNRAS, 444: 961–970. http://arxiv.org/abs/1405.3985, http://dx.doi.org/10.1093/mnras/stu1479

Gaug, M. (2006): *Calibration of the MAGIC telescope and observation of gamma-ray bursts*. Ph.D. thesis, Universitat Autonoma de Barcelona

Geringer-Sameth, A. & Koushiappas, S. M. (2011): Phys. Rev. Lett., 107, 24: 241303. http://arxiv.org/abs/1108.2914, http://dx.doi.org/10.1103/PhysRevLett.107.241303

Glashow, S. L. (1961): Nucl. Phys. A, 22: 579–588. http://dx.doi.org/10.1016/0029-5582(61)90469-2

Goldberg, H. (1983): Phys. Rev. Lett., 50: 1419–1422. http://dx.doi.org/10.1103/PhysRevLett.50.1419

Gondolo, P. *et al.* (2004): J. Cosmology Astropart. Phys., 7: 008. http://arxiv.org/abs/astro-ph/0406204, http://dx.doi.org/10.1088/1475-7516/2004/07/008

Gonzalez, A. H. *et al.* (2013): ApJ, 778: 14. http://arxiv.org/abs/1309.3565, http://dx.doi.org/10.1088/0004-637X/778/1/14

Governato, F. *et al.* (2010): Nature, 463: 203–206. http://arxiv.org/abs/0911.2237, http://dx.doi.org/10.1038/nature08640

Green, A. M., Hofmann, S. & Schwarz, D. J. (2004): MNRAS, 353, 3: L23–L27. http://dx.doi.org/10.1111/j.1365-2966.2004.08232.x

Griest, K., Cieplak, A. M. & Lehner, M. J. (2013): Phys. Rev. Lett., 111: 181302. http://dx.doi.org/10.1103/PhysRevLett.111.181302

Gross, D. J. & Wilczek, F. (1973): Phys. Rev. Lett., 30, 26: 1343–1346. http://dx.doi.org/10.1103/PhysRevLett.30.1343

Gunn, J. E. *et al.* (1978): ApJ, 223: 1015–1031. http://dx.doi.org/10.1086/156335

Guralnik, G. S., Hagen, C. R. & Kibble, T. W. (1964): Phys. Rev. Lett., 13: 585–587. http://dx.doi.org/10.1103/PhysRevLett.13.585

Hahn, J. *et al.* (2014): Astroparticle Physics, 54, 0: 25 – 32. http://dx.doi.org/10.1016/j.astropartphys.2013.10.003

Higgs, P. W. (1964): Phys. Rev. Lett., 13: 508–509. http://dx.doi.org/10.1103/PhysRevLett.13.508

Hillas, A. M. (1985): International Cosmic Ray Conference, 3: 445–448

Hillas, A. M. (1996): Space Sci. Rev., 75: 17–30. http://dx.doi.org/10.1007/BF00195021

Hillas, A. M. (2013): Astroparticle Physics, 43: 19–43. http://dx.doi.org/10.1016/j.astropartphys.2012.06.002

Hinshaw, G. *et al.* (2013): ApJS, 208: 19. http://arxiv.org/abs/1212.5226, http://dx.doi.org/10.1088/0067-0049/208/2/19

Hinton, J. (2009): New Journal of Physics, 11, 5: 055005. http://stacks.iop.org/1367-2630/11/i=5/a=055005

Hinton, J. A. & Hofmann, W. (2009): ARA&A, 47: 523. http://arxiv.org/abs/1006.5210, http://dx.doi.org/10.1146/annurev-astro-082708-101816

Hisano, J., Matsumoto, S. & Nojiri, M. M. (2004): Phys. Rev. Lett., 92, 3: 031303. http://arxiv.org/abs/arXiv:hep-ph/0307216, http://dx.doi.org/10.1103/PhysRevLett.92.031303

Holder, J. (2012): Astroparticle Physics, 39–40, 0: 61 – 75. Cosmic Rays Topical Issue, http://dx.doi.org/10.1016/j.astropartphys.2012.02.014

Holder, J. *et al.* (2006): Astroparticle Physics, 25: 391–401. http://arxiv.org/abs/astro-ph/0604119, http://dx.doi.org/10.1016/j.astropartphys.2006.04.002

Hooper, D. & Profumo, S. (2007): Phys. Rep., 453: 29–115. http://arxiv.org/abs/hep-ph/0701197, http://dx.doi.org/10.1016/j.physrep.2007.09.003

Horns, D. *et al.* (2012): Phys. Rev. D, 86, 7: 075024. http://arxiv.org/abs/1207.0776, http://dx.doi.org/10.1103/PhysRevD.86.075024

Hryczuk, A. & Iengo, R. (2012): Journal of High Energy Physics, 2012, 1: 1–25. http://dx.doi.org/10.1007/JHEP01(2012)163

Hu, W. & Dodelson, S. (2002): ARA&A, 40, 1: 171–216. http://arxiv.org/abs/http://www.annualreviews.org/doi/pdf/10.1146/annurev.astro.40.060401.093926, http://dx.doi.org/10.1146/annurev.astro.40.060401.093926

Hubble, E. (1929): Proceedings of the National Academy of Science, 15: 168–173. http://dx.doi.org/10.1073/pnas.15.3.168

Hunter, J. D. (2007): Computing in Science & Engineering, 9, 3: 90–95. http://link.aip.org/link/?CSX/9/90/1

IceCube Collaboration (2013): Science, 342, 6161. http://dx.doi.org/10.1126/science.1242856

Ikebe, Y. *et al.* (1996): Nature, 379: 427–429. http://dx.doi.org/10.1038/379427a0

Ivezic, Z. *et al.* (2008): ArXiv e-prints. http://arxiv.org/abs/0805.2366

James, F., *Statistical Methods in Experimental Physics: 2nd Edition* (World Scientific Publishing Co, 2006)

Jaynes, E. T. & Bretthorst, G. L., *Probability Theory* (Cambridge University Press, 2003)

Jeltema, T. E., Kehayias, J. & Profumo, S. (2009): Phys. Rev. D, 80, 2: 023005. http://arxiv.org/abs/0812.0597, http://dx.doi.org/10.1103/PhysRevD.80.023005

Jones, E. *et al.* (2001): "SciPy: Open source scientific tools for Python". http://www.scipy.org/

Jungman, G., Kamionkowski, M. & Griest, K. (1996): Phys. Rep., 267: 195. http://arxiv.org/abs/arXiv:hep-ph/9506380, http://dx.doi.org/10.1016/0370-1573(95)00058-5

Kahlhoefer, F. *et al.* (2014): MNRAS, 437, 3: 2865–2881. http://dx.doi.org/10.1093/mnras/stt2097

Kaiser, N. *et al.*, In "Survey and Other Telescope Technologies and Discoveries", , edited by J. A. Tyson & S. Wolff, volume 4836 of *Society of Photo-Optical Instrumentation Engineers (SPIE) Conference Series*, pp. 154–164 (2002). http://dx.doi.org/10.1117/12.457365

Kaluza, T. (1921): Sitzungsberichte der Preussischen Akademie der Wissenschaften, 54: 966

Keller, S. C. *et al.* (2007): PASA, 24: 1–12. http://arxiv.org/abs/astro-ph/0702511, http://dx.doi.org/10.1071/AS07001

Klein, O. (1926): Zeitschrift für Physik, 37, 12: 895–906. http://dx.doi.org/10.1007/BF01397481

Klypin, A. *et al.* (1999): ApJ, 522, 1: 82. http://stacks.iop.org/0004-637X/522/i=1/a=82

Kolb, E. W. & Slansky, R. (1984): Physics Letters B, 135, 5–6: 378 – 382. http://dx.doi.org/10.1016/0370-2693(84)90298-3

Konopelko, A. *et al.* (1999): Astroparticle Physics, 10: 275–289. http://arxiv.org/abs/astro-ph/9901199, http://dx.doi.org/10.1016/S0927-6505(98)00062-0

Koposov, S. *et al.* (2008): ApJ, 686, 1: 279. http://stacks.iop.org/0004-637X/686/i=1/a=279

Kowalczyk, K. *et al.* (2013): MNRAS, 431, 3: 2796–2807. http://dx.doi.org/10.1093/mnras/stt376

Kravtsov, A. V. & Borgani, S. (2012): ARA&A, 50: 353–409. http://arxiv.org/abs/1205.5556, http://dx.doi.org/10.1146/annurev-astro-081811-125502

Kroupa, P. (2012): PASA, 29: 395–433. http://dx.doi.org/10.1071/AS12005

Kuhlen, M. (2010): Advances in Astronomy, 2010: 162083. http://arxiv.org/abs/0906.1822, http://dx.doi.org/10.1155/2010/162083

Kuhlen, M., Diemand, J. & Madau, P. (2008): ApJ, 686, 1: 262. http://stacks.iop.org/0004-637X/686/i=1/a=262

Kuhlen, M., Vogelsberger, M. & Angulo, R. (2012a): Physics of the Dark Universe, 1, 1–2: 50 – 93. http://dx.doi.org/10.1016/j.dark.2012.10.002

Kuhlen, M. *et al.* (2012b): ApJ, 749, 1: 36. http://stacks.iop.org/0004-637X/749/i=1/a=36

Kuhlen, M., Madau, P. & Krumholz, M. R. (2013): ApJ, 776, 1: 34. http://stacks.iop.org/0004-637X/776/i=1/a=34

Kuzio de Naray, R. & Spekkens, K. (2011): ApJ, 741, 2: L29. http://stacks.iop.org/2041-8205/741/i=2/a=L29

Kuzio de Naray, R. *et al.* (2010): ApJ, 710: L161–L166. http://arxiv.org/abs/0912.3518, http://dx.doi.org/10.1088/2041-8205/710/2/L161

Lamanna, G. *et al.* (2013): ArXiv e-prints. http://arxiv.org/abs/1307.4918

Laporte, C. F. P., Walker, M. G. & Peñarrubia, J. (2013): MNRAS: Letters, 433, 1: 54–58. http://dx.doi.org/10.1093/mnrasl/slt057

Lattanzi, M. & Silk, J. (2009): Phys. Rev. D, 79, 8: 083523. http://dx.doi.org/10.1103/PhysRevD.79.083523

Lee, S. K. *et al.* (2014): Phys. Rev. Lett., 112: 011301. http://dx.doi.org/10.1103/PhysRevLett.112.011301

Lemaître, G. (1927): Annales de la Société Scientifique de Bruxelles, 47: 49–59

Li, T. & Ma, Y. (1983): ApJ, 272: 317. http://dx.doi.org/10.1086/161295

Loeb, A. & Furlanetto, S. R., *The First Galaxies in the Universe*. Princeton Series in Astrophysics (Princeton University Press, 2013). http://www.jstor.org/stable/j.ctt24hrpv

Lola, S. (2011): Fortschritte der Physik, 59: 1093–1097. http://dx.doi.org/10.1002/prop.201100067

Longair, M. S., *The Cosmic Century* (Cambridge University Press, 2013)

Lundberg, J. *et al.* (2010): Computer Physics Communications, 181: 683–686. http://arxiv.org/abs/0907.3450, http://dx.doi.org/10.1016/j.cpc.2009.11.001

Macciò, A. V., Dutton, A. A. & van den Bosch, F. C. (2008): MNRAS, 391: 1940–1954. http://arxiv.org/abs/0805.1926, http://dx.doi.org/10.1111/j.1365-2966.2008.14029.x

Madhavacheril, M. S., Sehgal, N. & Slatyer, T. R. (2013): ArXiv e-prints. http://arxiv.org/abs/1310.3815

Martin, S. P., In "Perspectives on Supersymmetry", , edited by G. L. Kane, p. 1 (1998). http://arxiv.org/abs/hep-ph/9709356

Martinez, G. D. *et al.* (2009): J. Cosmology Astropart. Phys., 2009, 06: 014. http://stacks.iop.org/1475-7516/2009/i=06/a=014

Martinez, G. D. *et al.* (2011): ApJ, 738, 1: 55. http://stacks.iop.org/0004-637X/738/i=1/a=55

Mashchenko, S., Couchman, H. M. P. & Wadsley, J. (2006): Nature, 442: 539–542. http://arxiv.org/abs/astro-ph/0605672, http://dx.doi.org/10.1038/nature04944

Massey, R., Kitching, T. & Richard, J. (2010): Reports on Progress in Physics, 73, 8: 086901. http://arxiv.org/abs/1001.1739, http://dx.doi.org/10.1088/0034-4885/73/8/086901

Mather, J. C. *et al.* (1990): ApJ, 354: L37–L40. http://dx.doi.org/10.1086/185717

Matta, C. F. *et al.* (2011): Journal of Chemical Education, 88: 67–70. http://dx.doi.org/10.1021/ed1000476

McConnachie, A. W. (2012): AJ, 144: 4. http://arxiv.org/abs/1204.1562, http://dx.doi.org/10.1088/0004-6256/144/1/4

Meade, P. *et al.* (2010): Nuclear Physics B, 831, 1–2: 178 – 203. http://dx.doi.org/10.1016/j.nuclphysb.2010.01.012

Meyer, M., Horns, D. & Zechlin, H.-S. (2010): A&A, 523: A2. http://arxiv.org/abs/1008.4524, http://dx.doi.org/10.1051/0004-6361/201014108

Meyer, M., Horns, D. & Raue, M. (2013): Phys. Rev. D, 87, 3: 035027. http://arxiv.org/abs/1302.1208, http://dx.doi.org/10.1103/PhysRevD.87.035027

Milgrom, M. (1983): ApJ, 270: 365–370. http://dx.doi.org/10.1086/161130

Miller, S. H. *et al.* (2014): ApJ, 782, 2: 115. http://stacks.iop.org/0004-637X/782/i=2/a=115

Mitsou, V. A. (2013): International Journal of Modern Physics A, 28: 30052. http://arxiv.org/abs/1310.1072, http://dx.doi.org/10.1142/S0217751X13300524

Moiseev, A. A. *et al.* (2013): ArXiv e-prints. http://arxiv.org/abs/1307.2345

Moroi, T. & Randall, L. (2000): Nuclear Physics B, 570: 455. http://arxiv.org/abs/arXiv:hep-ph/9906527, http://dx.doi.org/10.1016/S0550-3213(99)00748-8

Morrissey, D. E., Plehn, T. & Tait, T. M. P. (2012): Phys. Rep., 515: 1–113. http://arxiv.org/abs/0912.3259, http://dx.doi.org/10.1016/j.physrep.2012.02.007

Navarro, J. F., Eke, V. R. & Frenk, C. S. (1996): MNRAS, 283, 3: L72–L78. http://dx.doi.org/10.1093/mnras/283.3.L72

Navarro, J. F., Frenk, C. S. & White, S. D. M. (1996): ApJ, 462: 563. http://arxiv.org/abs/astro-ph/9508025, http://dx.doi.org/10.1086/177173

Navarro, J. F., Frenk, C. S. & White, S. D. M. (1997): ApJ, 490: 493. http://arxiv.org/abs/astro-ph/9611107, http://dx.doi.org/10.1086/304888

Navarro, J. F. *et al.* (2004): MNRAS, 349, 3: 1039–1051. http://dx.doi.org/10.1111/j.1365-2966.2004.07586.x

Nesti, F. & Salucci, P. (2013): J. Cosmology Astropart. Phys., 7: 016. http://arxiv.org/abs/1304.5127, http://dx.doi.org/10.1088/1475-7516/2013/07/016

Nezri, E. *et al.* (2012): MNRAS, 425, 1: 477–489. http://dx.doi.org/10.1111/j.1365-2966.2012.21484.x

Nguyen, N., Horns, D. & Bringmann, T., In "Proceedings of the 13th ICATPP Conference", , edited by S. Giani *et al.*, pp. 1025–1030 (2012). http://arxiv.org/abs/1202.1385, http://dx.doi.org/10.1142/9789814405072_0154

Ohm, S., van Eldik, C. & Egberts, K. (2009): Astroparticle Physics, 31: 383–391. http://arxiv.org/abs/0904.1136, http://dx.doi.org/10.1016/j.astropartphys.2009.04.001

Oliphant, T. E. (2007): Computing in Science & Engineering, 9, 3: 10–20. http://link.aip.org/link/?CSX/9/10/1

Oort, J. H. (1932): Bull. Astron. Inst. Netherlands, 6: 249

Ostriker, J. P. & Steinhardt, P. (2003): Science, 300, 5627: 1909–1913. http://dx.doi.org/10.1126/science.1085976

Padmanabhan, N. & Finkbeiner, D. P. (2005): Phys. Rev. D, 72, 2: 023508. http://arxiv.org/abs/astro-ph/0503486, http://dx.doi.org/10.1103/PhysRevD.72.023508

Paolillo, M. *et al.* (2002): ApJ, 565: 883. http://arxiv.org/abs/astro-ph/0109342, http://dx.doi.org/10.1086/337919

Parker, M. A. (2013): Physica Scripta, 2013, T158: 014015. http://stacks.iop.org/1402-4896/2013/i=T158/a=014015

Pedaletti, G., Wagner, S. & Benbow, W., In "International Cosmic Ray Conference", volume 3, p. 933 (2008). http://arxiv.org/abs/0709.2778

Pedaletti, G., Wagner, S. J. & Rieger, F. M. (2011): ApJ, 738: 142. http://arxiv.org/abs/1107.0910, http://dx.doi.org/10.1088/0004-637X/738/2/142

Penzias, A. A. & Wilson, R. W. (1965): ApJ, 142: 419–421. http://dx.doi.org/10.1086/148307

Penzo, C. *et al.* (2014): MNRAS, 442: 176–186. http://arxiv.org/abs/1401.3338, http://dx.doi.org/10.1093/mnras/stu857

Pérez, F. & Granger, B. E. (2007): Comput. Sci. Eng., 9, 3: 21–29. http://ipython.org

Perkins, J. S., Maier, G. & The VERITAS Collaboration (2009): ArXiv e-prints. http://arxiv.org/abs/0912.3841

Pieri, L. *et al.* (2009): A&A, 496: 351–360. http://arxiv.org/abs/0812.1494, http://dx.doi.org/10.1051/0004-6361:200810888

Pinzke, A., Pfrommer, C. & Bergström, L. (2009): Phys. Rev. Lett., 103, 18: 181302. http://arxiv.org/abs/0905.1948, http://dx.doi.org/10.1103/PhysRevLett.103.181302

Pinzke, A., Pfrommer, C. & Bergstrom, L. (2011): Phys.Rev., D84: 123509. http://arxiv.org/abs/1105.3240, http://dx.doi.org/10.1103/PhysRevD.84.123509

Planck Collaboration *et al.* (2013a): ArXiv e-prints. http://arxiv.org/abs/1303.5062

Planck Collaboration *et al.* (2013b): ArXiv e-prints. http://arxiv.org/abs/1303.5076

Planck Collaboration *et al.* (2013c): ArXiv e-prints. http://arxiv.org/abs/1303.5082

Politzer, H. D. (1973): Phys. Rev. Lett., 30, 26: 1346–1349. http://dx.doi.org/10.1103/PhysRevLett.30.1346

Pontzen, A. & Governato, F. (2012): MNRAS, 421, 4: 3464–3471. http://dx.doi.org/10.1111/j.1365-2966.2012.20571.x

Pontzen, A. & Governato, F. (2014): Nature, 506: 171–178. http://arxiv.org/abs/1402.1764, http://dx.doi.org/10.1038/nature12953

Porter, T. A., Johnson, R. P. & Graham, P. W. (2011): ARA&A, 49: 155–194. http://arxiv.org/abs/1104.2836, http://dx.doi.org/10.1146/annurev-astro-081710-102528

Press, W. H. & Schechter, P. (1974): ApJ, 187: 425–438. http://dx.doi.org/10.1086/152650

Protassov, R. *et al.* (2002): ApJ, 571: 545–559. http://arxiv.org/abs/astro-ph/0201547, http://dx.doi.org/10.1086/339856

Read, J. I. (2014): Journal of Physics G, 41, 6: 063101. http://arxiv.org/abs/1404.1938, http://dx.doi.org/10.1088/0954-3899/41/6/063101

Reiprich, T. H. & Böhringer, H. (2002): ApJ, 567: 716. http://arxiv.org/abs/astro-ph/0111285, http://dx.doi.org/10.1086/338753

Richtler, T. *et al.* (2008): A&A, 478: L23. http://arxiv.org/abs/0711.4077, http://dx.doi.org/10.1051/0004-6361:20078539

Rieger, F. M., de Oña-Wilhelmi, E. & Aharonian, F. A. (2013): Frontiers of Physics, 8: 714–747. http://arxiv.org/abs/1302.5603, http://dx.doi.org/10.1007/s11467-013-0344-6

Ringwald, A. (2012): Physics of the Dark Universe, 1, 1–2: 116 – 135. http://dx.doi.org/10.1016/j.dark.2012.10.008

Ripken, J. *et al.* (2014): J. Cosmology Astropart. Phys., 1: 049. http://arxiv.org/abs/1211.6922, http://dx.doi.org/10.1088/1475-7516/2014/01/049

Robertson, B. E. *et al.* (2010): Nature, 468: 49–55. http://arxiv.org/abs/1011.0727, http://dx.doi.org/10.1038/nature09527

Rocha, M. *et al.* (2013): MNRAS, 430, 1: 81–104. http://dx.doi.org/10.1093/mnras/sts514

Rolke, W. A., López, A. M. & Conrad, J. (2005): NIM A, 551: 493–503. http://arxiv.org/abs/arXiv:physics/0403059, http://dx.doi.org/10.1016/j.nima.2005.05.068

Rothman, T. & Boughn, S. (2006): Foundations of Physics, 36, 12: 1801–1825. http://dx.doi.org/10.1007/s10701-006-9081-9

Rowell, G. P. (2003): A&A, 410: 389. http://arxiv.org/abs/astro-ph/0310025, http://dx.doi.org/10.1051/0004-6361:20031194

Rubin, V. C. & Ford, W. K., Jr. (1970): ApJ, 159: 379. http://dx.doi.org/10.1086/150317

Rubin, V. C., Ford, W. K. J. & . Thonnard, N. (1980): ApJ, 238: 471–487. http://dx.doi.org/10.1086/158003

Saglia, R. P. *et al.* (2000): AJ, 119: 153–161. http://arxiv.org/abs/astro-ph/9909446, http://dx.doi.org/10.1086/301153

Salam, A., In "Proceedings of 8th Nobel Symposium, Lerum, Sweden", pp. 367–377 (1968)

Samtleben, D., Staggs, S. & Winstein, B. (2007): Annual Review of Nuclear and Particle Science, 57: 245–283. http://arxiv.org/abs/0803.0834, http://dx.doi.org/10.1146/annurev.nucl.54.070103.181232

Sánchez-Conde, M. A. *et al.* (2011): J. Cosmology Astropart. Phys., 12: 011. http://arxiv.org/abs/1104.3530, http://dx.doi.org/10.1088/1475-7516/2011/12/011

Schneider, P., *Einführung in die extragalaktische Astronomie und Kosmologie* (Springer, Berlin, 2006)

Schneider, A. *et al.* (2014): MNRAS, 441: L6–L10. http://arxiv.org/abs/1309.5960, http://dx.doi.org/10.1093/mnrasl/slu034

Schuberth, Y. *et al.* (2010): A&A, 513: A52. http://arxiv.org/abs/0911.0420, http://dx.doi.org/10.1051/0004-6361/200912482

Servant, G. & Tait, T. M. P. (2003): Nuclear Physics B, 650: 391. http://arxiv.org/abs/arXiv:hep-ph/0206071, http://dx.doi.org/10.1016/S0550-3213(02)01012-X

Simon, J. D. *et al.* (2011): ApJ, 733: 46. http://arxiv.org/abs/1007.4198, http://dx.doi.org/10.1088/0004-637X/733/1/46

Smoot, G. F. *et al.* (1992): ApJ, 396: L1–L5. http://dx.doi.org/10.1086/186504

Sommerfeld, A. (1931): Annalen der Physik, 403, 3: 257–330. http://dx.doi.org/10.1002/andp.19314030302

Spergel, D. N. & Steinhardt, P. J. (2000): Phys. Rev. Lett., 84: 3760–3763. http://dx.doi.org/10.1103/PhysRevLett.84.3760

Springel, V. *et al.* (2005): Nature, 435: 629–636. http://arxiv.org/abs/astro-ph/0504097, http://dx.doi.org/10.1038/nature03597

Springel, V., Frenk, C. S. & White, S. D. M. (2006): Nature, 440: 1137–1144. http://arxiv.org/abs/astro-ph/0604561, http://dx.doi.org/10.1038/nature04805

Springel, V. *et al.* (2008a): Nature, 456: 73–76. http://arxiv.org/abs/0809.0894, http://dx.doi.org/10.1038/nature07411

Springel, V. *et al.* (2008b): MNRAS, 391: 1685. http://arxiv.org/abs/0809.0898, http://dx.doi.org/10.1111/j.1365-2966.2008.14066.x

Stepanian, A. A., Fomin, V. P. & Vladimirskii, B. M. (1983): Izvestiya Ordena Trudovogo Krasnogo Znameni Krymskoj Astrofizicheskoj Observatorii, 66: 234–241

Stigler, S. M. (2007): Statistical Science, 22, 4: 598–620. http://dx.doi.org/10.1214/07-STS249

Stinson, G. S. *et al.* (2013): MNRAS, 428, 1: 129–140. http://dx.doi.org/10.1093/mnras/sts028

Storm, E. *et al.* (2013): ApJ, 768: 106. http://arxiv.org/abs/1210.0872, http://dx.doi.org/10.1088/0004-637X/768/2/106

Strigari, L. E. (2013): Phys. Rep., 531: 1–88. http://arxiv.org/abs/1211.7090, http://dx.doi.org/10.1016/j.physrep.2013.05.004

Susskind, L. (1979): Phys. Rev. D, 20: 2619–2625. http://dx.doi.org/10.1103/PhysRevD.20.2619

Suzuki, N. *et al.* (2012): ApJ, 746, 1: 85. http://stacks.iop.org/0004-637X/746/i=1/a=85

't Hooft, G. (2007): Nature, 448, 7151: 271–273. http://www.scopus.com/inward/record.url?eid=2-s2.0-34447503692&partnerID=40&md5=47c45cf5a314d469b49f9cdcef848885

't Hooft, G. & Veltman, M. (1972): Nuclear Physics B, 44: 189–213. http://dx.doi.org/10.1016/0550-3213(72)90279-9

Takayama, F. & Yamaguchi, M. (2000): Physics Letters B, 485: 388–392. http://arxiv.org/abs/hep-ph/0005214, http://dx.doi.org/10.1016/S0370-2693(00)00726-7

The Dark Energy Survey Collaboration (2005): ArXiv Astrophysics e-prints. http://arxiv.org/abs/astro-ph/0510346

Tisserand, P. *et al.* (2007): A&A, 469, 2: 387–404. http://dx.doi.org/10.1051/0004-6361:20066017

Tollerud, E. J. *et al.* (2008): ApJ, 688, 1: 277. http://stacks.iop.org/0004-637X/688/i=1/a=277

Tonry, J. L. *et al.* (2001): ApJ, 546: 681. http://arxiv.org/abs/astro-ph/0011223, http://dx.doi.org/10.1086/318301

van den Aarssen, L. G., Bringmann, T. & Pfrommer, C. (2012): Phys. Rev. Lett., 109: 231301. http://dx.doi.org/10.1103/PhysRevLett.109.231301

van den Bergh, S. (1999): PASP, 111: 657–660. http://arxiv.org/abs/astro-ph/9904251, http://dx.doi.org/10.1086/316369

Viana, A. *et al.* (2012): ApJ, 746: 77. http://arxiv.org/abs/1103.2627, http://dx.doi.org/10.1088/0004-637X/746/1/77

Viel, M. *et al.* (2006): Phys. Rev. Lett., 97: 071301. http://dx.doi.org/10.1103/PhysRevLett.97.071301

Viel, M. *et al.* (2013): Phys. Rev. D, 88, 4: 043502. http://arxiv.org/abs/1306.2314, http://dx.doi.org/10.1103/PhysRevD.88.043502

Voit, G. M. (2005): Reviews of Modern Physics, 77: 207. http://arxiv.org/abs/astro-ph/0410173, http://dx.doi.org/10.1103/RevModPhys.77.207

Völk, H. & Bernlöhr, K. (2009): Experimental Astronomy, 25, 1-3: 173–191. http://dx.doi.org/10.1007/s10686-009-9151-z

Walker, M., *Dark Matter in the Galactic Dwarf Spheroidal Satellites*, p. 1039 (2013). http://dx.doi.org/10.1007/978-94-007-5612-0_20

Walker, M. G. & Peñarrubia, J. (2011): ApJ, 742, 1: 20. http://stacks.iop.org/0004-637X/742/i=1/a=20

Walker, M. G. *et al.* (2009): ApJ, 704, 2: 1274. http://stacks.iop.org/0004-637X/704/i=2/a=1274

Walker, M. G. *et al.* (2010): ApJ, 710, 1: 886. http://stacks.iop.org/0004-637X/710/i=1/a=886

Walker, M. G. *et al.* (2011): ApJ, 733: L46. http://arxiv.org/abs/1104.0411, http://dx.doi.org/10.1088/2041-8205/733/2/L46

Walter, M., Spiering, C. & Knapp, J. (2014): Astroparticle Physics, 53, 0: 1 – 2. http://dx.doi.org/10.1016/j.astropartphys.2013.10.006

Weekes, T. C. *et al.* (1989): ApJ, 342: 379–395. http://dx.doi.org/10.1086/167599

Weekes, T. C. *et al.* (2002): Astroparticle Physics, 17: 221–243. http://arxiv.org/abs/astro-ph/0108478, http://dx.doi.org/10.1016/S0927-6505(01)00152-9

Weinberg, S. (1967): Phys. Rev. Lett., 19: 1264–1266. http://dx.doi.org/10.1103/PhysRevLett.19.1264

Weinberg, S., *The first three minutes. A modern view of the origin of the universe* (1977)

Weinberg, D. H. *et al.*, In "The Emergence of Cosmic Structure", , edited by S. H. Holt & C. S. Reynolds, volume 666 of *American Institute of Physics Conference Series*, pp. 157–169 (2003). http://arxiv.org/abs/astro-ph/0301186, http://dx.doi.org/10.1063/1.1581786

Weinberg, D. H. *et al.* (2013): ArXiv e-prints. http://arxiv.org/abs/1306.0913

Weinmann, S. M. *et al.* (2011): MNRAS, 416, 2: 1197–1214. http://dx.doi.org/10.1111/j.1365-2966.2011.19118.x

Weniger, C. (2012): J. Cosmology Astropart. Phys., 2012, 08: 007. http://stacks.iop.org/1475-7516/2012/i=08/a=007

Wess, J. & Zumino, B. (1974): Nuclear Physics B, 70: 39–50. http://dx.doi.org/10.1016/0550-3213(74)90355-1

Wilks, S. S. (1938): Annals of Mathematical Statistics, 9: 60–62

Willman, B. *et al.* (2011): AJ, 142: 128. http://arxiv.org/abs/1007.3499, http://dx.doi.org/10.1088/0004-6256/142/4/128

Wolf, J. *et al.* (2010): MNRAS, 406: 1220–1237. http://arxiv.org/abs/0908.2995, http://dx.doi.org/10.1111/j.1365-2966.2010.16753.x

Wood, M. D. (2010): *An Indirect Search for Dark Matter with VERITAS*. Ph.D. thesis, University of California, Los Angeles

Wyatt, T. (2007): Nature, 448: 274–280. http://dx.doi.org/10.1038/nature06075

Wyrzykowski, L. *et al.* (2011): MNRAS, 413, 1: 493–508. http://dx.doi.org/10.1111/j.1365-2966.2010.18150.x

Yang, C. N. & Mills, R. L. (1954): Phys. Rev., 96: 191–195. http://dx.doi.org/10.1103/PhysRev.96.191

Zitzer, B. (2012): Physics Procedia, 37, 0: 1365 – 1372. http://dx.doi.org/10.1016/j.phpro.2012.03.740

Zwicky, F. (1933): Helvetica Physica Acta, 6: 110–127

Acknowledgements

Blabla, Weltfrieden.

... seriously: There is a number of people whom I would like to thank for letting me do the work presented in this thesis. First of all, there is Dieter Horns at the Universität Hamburg, my supervisor (and, indirectly, employer). Without his support, none of this would have been possible. Secondly, I would like to thank Jan Conrad, who made it possible for me to spend three nice months at Stockholms universitet, and who ignited the work that became Chapter 4 of this thesis.

Next, I would like to thank my co-workers: Hugh Dickinson in Stockholm had a lot of patience with my attempts to understand his C++ code. In Hamburg, Nelly Nguyen and Hannes Zechlin were my fellow inmates at the Chamber of Darkness, though I think we managed to take it rather lightly. I want to thank both of them for illuminating discussions and a lot of fun. All members of the Hamburg astroparticle group ought to be thanked for creating a working atmosphere that is both inspiring and very pleasant (at least most of the time). I cannot name all of them here, but Martin Tluczykont and Attila Abramowski may be singled out for providing valuable comments on the draft stages of this thesis. Christian Farnier in Stockholm, and especially Joachim Ripken, now in Göttingen, have also helped a lot — many thanks!

I should also thank the members of the H.E.S.S. collaboration, and especially the Astroparticle Working Group, for the inspiring discussions and the interesting experience of international cooperation. Many thanks go to Albert Jahnke and Jarosław Dyks for the nice shift in Namibia.

It is also a pleasure to thank many people I don't even know: It was lots of fun to do my work using the Python language, the IPython interpreter, and the SciPy, NumPy, and Matplotlib extensions. See Section 4.1.4 for the URLs — many thanks to everyone involved in the construction and maintenance of these open source tools, and to the people at `stackoverflow.com` and its partner sites. The `pomodorotechnique.com` was also essential for the completion of this thesis.

Finally, I want to thank my family and friends for their love and support during the last few years. I hope I haven't forgotten anybody.

List of publications

I am the (corresponding) author of the following publications:

1. Opitz, B., “Dark matter searches with H.E.S.S.”, SciNeGHE Proceeding (2010).
   adsabs.harvard.edu/abs/2010AIPC.1223..140O
2. Abramowski, A. *et al.*, “Search for Dark Matter Annihilation Signals from the Fornax Galaxy Cluster with H.E.S.S.”, ApJ 750,12:123 (2012).
   adsabs.harvard.edu/abs/2012ApJ...750..123A
3. Abramowski, A. *et al.*, “Erratum: "Search for Dark Matter Annihilation Signals from the Fornax Galaxy Cluster with H.E.S.S.", ApJ 783,1:63 (2014).
   adsabs.harvard.edu/abs/2014ApJ...783...63A
4. Diplomarbeit: “Studies towards an improved determination of the gluon density in the proton using jet measurements at HERA”, Universität Hamburg (2008).

In addition, there are, at the time of this writing, 58 publications whose co-author I am as a member of the H.E.S.S. collaboration. I do not list them here, but they can be retrieved at tinyurl.com/HESS-Publ-Opitz.